JETP Letters, Vol. 76, No. 9, 2002, pp. 545–547. From Pis'ma v Zhurnal Éksperimental'noĭ i Teoreticheskoĭ Fiziki, Vol. 76, No. 9, 2002, pp. 643–644.

Improved Limits on β^- and $\beta^-\beta^-$ Decays of ^{48}Ca¶

A. Bakalyarov[1], A. Balysh[1], A. S. Barabash[2], P. Beneš[3], Ch. Briançon[4], V. Brudanin[5], P. Čermák[3], V. Egorov[5], F. Hubert[6], Ph. Hubert[6], N. A. Korolev[5], V. N. Kosjakov[1], A. Kovalik[5], N. A. Lebedev[5], V. I. Lebedev[1], A. F. Novgorodov[5], N. I. Rukhadze[5], N. I. Štekl[3], V. V. Timkin[5], I. E. Veleshko[1], Ts. Vylov[5], and V. I. Umatov[2]

[1] *Russian Research Centre Kurchatov Institute, Kurchatov Square, Moscow, 123182 Russia*

[2] *Institute of Theoretical and Experimental Physics, Moscow, 117259 Russia*

e-mail: barabash@vitep1.itep.ru

[3] *FNSPE, Czech Technical University, 11519 Prague, Czech Republic*

[4] *Centre de Spectrométrie Nucléaire et de Spectrométrie de Masse, IN2P3-CNRS et Université Paris-Sud, 91405 Orsay, France*

[5] *Joint Institute for Nuclear Research, Dubna, Moscow region, 141980 Russia*

[6] *Centre d'Études Nucléaires, IN2P3-CNRS et Université de Bordeaux, F-33170 Gradignan, France*

Received September 12, 2002

New limits on ^{48}Ca β^- and $\beta^-\beta^-$ decays to excited states of ^{48}Ti have been obtained using a 400 cm^3 low-background HPGe detector and an external source of 24.558 *g* enriched CaF_2 powder (9.822 *g* of ^{48}Ca). The limits for β^- decay to the 6^+ ground state and excited 5^+ and 4^+ states in ^{48}Sc are 1.6×10^{20} yr, 2.5×10^{20} yr, and 1.9×10^{20} yr at the 90% confidence level. For the $\beta^-\beta^-$ decay to ^{48}Ti, the limits to the first 2^+, second 2^+, and first 0^+ excited states are 1.8×10^{20} yr, 1.5×10^{20} yr, and 1.5×10^{20} yr, again at the 90% confidence level. © *2002 MAIK "Nauka/Interperiodica".*

PACS numbers: 23.40.Hc

The doubly magic nucleus ^{48}Ca can decay by beta decay and double beta decay. The largest possible energy released, 4272 keV, attracts attention to this isotope for double-beta-decay investigations. However, the small natural abundance (0.187%) and the feasibility problems of producing sufficient quantities of this isotope make studies of fare decays rather difficult. In a previous paper [1], we presented new limits (see table) on decays of ^{48}Ca. A low-background 400 cm^3 HPGe detector located in the Modane Underground Laboratory (depth of 4800 m w.e.) was used to measure 63.86 *g* of enriched $^{48}CaCO_3$ powder (enrichment is 73%; 20.18 *g* of ^{48}Ca were exposed for 797.3 hours). New upper limits improved by around one order of magnitude were obtained on half-lives of ^{48}Ca for β^- decay to the 6^+ ground state, excited 5^+ and 4^+ states in ^{48}Sc, and $\beta^-\beta^-$ decay to the first 2^+, second 2^+, and first 0^+ excited states in ^{48}Ti. However the sample was found to have fairly large radioactive impurities, mainly ^{60}Co and ^{226}Ra, which produced too high a background for the processes under investigation, and this limited the results. Consequently, we decided to repeat the experiment after the sample was purified.

Several methods of sample purification were developed using natural calcium with radioactive tracers. Reduction factors of 10^3 and 10^4 were achieved for $^{226(228)}$Ra and ^{60}Co, respectively. These results were obtained using the same HPGe detector that was used for measurements with enriched Ca samples. Activities of ^{60}Co, ^{226}Ra, and ^{228}Th impurities in the enriched Ca sample after purification were found to be less than 2 μBq/g, 4 μBq/g, and 2 μBq/g, respectively, which leads to reduction factors of >400, >70 and >25. The chemical purification technique yielded a CaF_2 powder.

The current experiment was performed with the 400 cm^3 HPGe detector and 24.558 *g* of enriched $^{48}CaF_2$ powder by looking for γ rays following β^- and $\beta^-\beta^-$ transitions of ^{48}Ca. A total of 9.822 *g* of ^{48}Ca was exposed for 1589.8 hours.

The HPGe detector is surrounded by a passive shield consisting of 6 cm of archeological lead, 10 cm of OFHC copper, and 15 cm of ordinary lead. To reduce the ^{222}Rn gas, which is one of the main sources of the background, special efforts were made to minimize the free space near the detector. In addition, the passive shield was enclosed in an aluminum box flushed with high-purity nitrogen. The cryostat, the endcap, and the critical mechanical components of the HPGe detector

¶This article was submitted by the authors in English.

Experimental half-life limits and theoretical predictions for the decay of ^{48}Ca

Transition	γ-ray, efficiency	$(T_{1/2})_{exp}$, 10^{20} yr		$(T_{1/2})_{theor}$, yr
		Present	Previous [1]	
	β^- decay			
$0^+ \longrightarrow 6^+_{g.s.}$	(983.5 keV, 3.25%) + (1312.1 keV, 2.65%)	>1.6	>0.71	1.5×10^{29}–1.3×10^{31} [3]
$0^+ \longrightarrow 5^+$	(130.9 keV, 15.2%)	>2.5	>1.1	$1.1^{+0.8}_{-0.6} \times 10^{21}$ [3]
$0^+ \longrightarrow 4^+_1$	(130.9 keV, 11.5%)	>1.9	>0.82	8.8×10^{23}–5.2×10^{28} [3]
	$\beta^-\beta^-(0\nu + 2\nu)$ decay			
$0^+ \longrightarrow 2^+_1$	(983.5 keV, 5.0%)	>1.8	>0.47	5.0×10^{26} [4]
$0^+ \longrightarrow 2^+_2$	(983.5 keV, 3.89%) + (1437.5 keV, 2.95%)	>1.5	>1.1	3.6×10^{26} [4]
$0^+ \longrightarrow 0^+_1$	(983.5 keV, 4.03%) + (2013.7 keV, 2.33%)	>1.5	>0.90	
			>10* [2]	

The γ rays accompanying the different modes are presented with their detection efficiencies. Experimental limits are given at the 90% confidence level. The asterisk * identifies the result for 0νββ decay mode taken from [2].

are made of very pure Al–Si alloy. Finally, the cryostat has a *J*-type geometry to shield the crystal from possible radioactive impurities in the dewar.

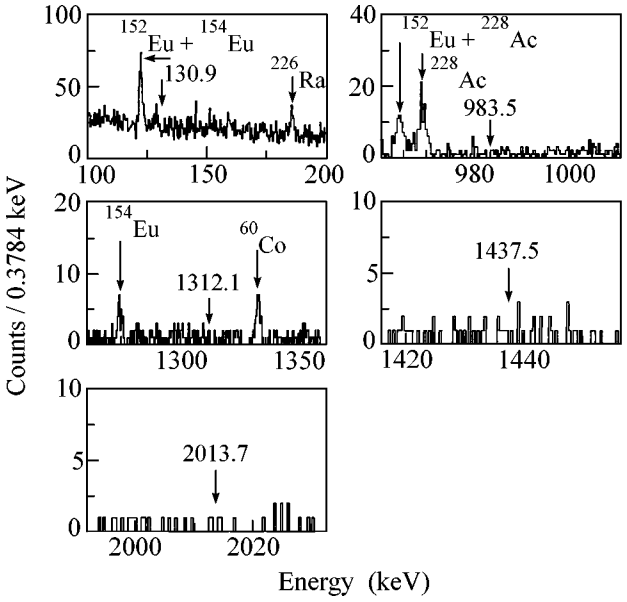

Partial γ-ray spectra of the energy ranges corresponding to the most intensive γ quanta of different decay modes of ^{48}Ca which were used to estimate limits. The arrows indicate the expected γ-line positions: 130.9 keV (β^- transitions to 5^+ and 4^+ excited states of ^{48}Sc), 983.5 keV (β^- transition to 6^+ ground state of ^{48}Sc and for all $\beta^-\beta^-$ transitions to excited states), 1312.1 keV (β^- transition to 6^+ ground state of ^{48}Sc), 1437.5 keV ($\beta^-\beta^-$ transition to 2^+_1 excited state of ^{48}Ti), 2013.7 keV ($\beta^-\beta^-$ transition to 0^+ excited state of ^{48}Ti).

The electronics consist of currently available spectrometric amplifiers and an 8192 channel ADC. The energy calibration was adjusted to cover the energy range from 50 keV to 3.5 MeV. The energy resolution was 1.9 keV for the 1332 keV line of ^{60}Co. The electronics were stable during the experiment due to the constant conditions in the laboratory (temperature of 23°C, hygrometric degree of 50%). A daily check on the apparatus assured that the counting rate was statistically constant.

The detection efficiencies have been computed with the CERN Monte Carlo code GEANT3.21. Special calibration measurements with radioactive sources and powders containing well-known ^{236}Ra activities confirmed that the accuracy of these efficiencies is within 10%.

The background in the regions of interest was found to decrease 5 to 10 times when compared with the previous measurement (figure). One can see from the figure that there are no statistically significant peaks at pointed places. Using the same method of data analysis [1], the new limits for the decay modes of ^{48}Ca were obtained. The table presents these limits with specified γ-lines and their detection efficiencies using in data analysis. The previous best results and theoretical estimates for the half-lives of the investigated transitions are given for comparison. As one can see, the limits have improved by a factor of two or three when compared with our previous measurement [1]. Note that the new limits fail to approach the theoretical predictions, with the exception of the β^- transition to the 5^+ excited

state of ^{48}Sc. For the last transition, current experiments can reach the half-life theoretical value.

This work was performed in the framework of collaboration agreement no. 99-44 between IN2P3 and JINR, which are gratefully acknowledged. The authors would also like to thank the Modane Underground Laboratory staff for their technical assistance in running the experiment. We are grateful to Prof. Sean Sutton for his remarks. This work was partly supported by INTAS (grant no. 00-00362), the Russian Foundation for Basic Research (project no. 00-02-16549), and the Grant Agency of the Czech Republic (contract no. 202/02/0157).

REFERENCES

1. A. Bakalyarov, A. Balysh, A. S. Barabash, *et al.*, Nucl. Phys. A **700**, 17 (2002).
2. A. S. Barabash, Phys. Lett. B **216**, 257 (1989).
3. M. Aunola, J. Suhonen, and T. Siiskonen, Europhys. Lett. **46**, 577 (1999).
4. W. C. Haxton and G. J. Stephenson, Prog. Part. Nucl. Phys. **12**, 409 (1984).

JETP Letters, Vol. 76, No. 9, 2002, pp. 548–552. Translated from Pis'ma v Zhurnal Éksperimental'noĭ i Teoreticheskoĭ Fiziki, Vol. 76, No. 9, 2002, pp. 645–649.

Ionization Spectrum Transformation and Compression of Powerful Femtosecond Laser Pulses in Experiments on the Propagation in Gas-Filled Dielectric Capillaries

A. A. Babin, D. V. Kartashov*, A. M. Kiselev, V. V. Lozhkarev, A. M. Sergeev, A. A. Solodov, and A. N. Stepanov

Institute of Applied Physics, Russian Academy of Sciences, ul. Ul'yanova 46, Nizhni Novgorod, 603950 Russia
** e-mail: dekart@ufp.appl.sci-nnov.ru*

Received August 23, 2002; in final form, September 30, 2002

The propagation of an intense ($I \le 10^6$ W/cm^2) femtosecond laser radiation with a duration of ~100 fs through gas-filled dielectric capillaries was studied. The radiation with a power up to 0.2 TW propagates along the paths up to 20 cm with a transmission efficiency of ~45%. The beam transverse structure at the output is close to the capillary fundamental mode under gas-ionization conditions. The transformation of pulse spectrum was studied as a function of input intensity. It is demonstrated experimentally that the pulse is compressed to a duration of ~30 fs due to the compensation of ionization-induced self-phase modulation in a linear dispersive element at the capillary output. © *2002 MAIK "Nauka/Interperiodica".*

PACS numbers: 51.70.+f; 32.80.Fb

The problem of increasing length of interaction between a high-intensity femtosecond laser radiation and a substance, compared to the diffraction Rayleigh length, arises in many physical problems, such as large-amplitude plasma wave generation for electron acceleration [1], fabrication of X-ray lasers [2], etc. Several ways were proposed for solving this problem. In particular, the propagation of a powerful laser radiation in preliminary formed plasma channels was investigated (see, e.g., [3, 4]). The use of hollow dielectric waveguides (capillaries) is one of the efficient ways of transmitting powerful laser radiation at distances appreciably exceeding the Rayleigh length. In [5, 6], the terawatt laser radiation was transported in vacuum capillaries at a distance more than an order of magnitude exceeding the Rayleigh length. The first results on the transmission of a powerful femtosecond laser radiation in gas-filled dielectric capillaries were obtained in [7, 8]. In the cited works, the influence of gas ionization on the transmission efficiency and the spatial distribution of output intensity were studied as functions of gas pressure and capillary diameter and length. In this work, we are mainly focused on the experimental study of a nonlinear spectrum transformation for an intense ($I \le 10^6$ W/cm^2) femtosecond laser radiation under conditions of gas ionization in capillary.

It is known that, upon the propagation of an intense ionizing laser radiation in gas, its spectrum becomes enriched at short wavelengths, as compared to the initial spectrum [9]. Due to a large radiation–gas interaction length in a capillary, one can attain, at relatively low gas pressures (few torrs) and plasma concentrations, the broadening and short-wavelength shift of pulse spectrum greater than in the known experiments with focusing powerful laser radiation in dense gases [9]. The spectrum broadening due to the nonlinear self-phase modulation caused by field-induced gas ionization can be used for the subsequent pulse compression in linear dispersive elements [10]. In this work, such a compression scheme for powerful laser radiation is experimentally implemented for the first time.

In the experiments, a femtosecond laser system on Ti : sapphire crystals was used with the amplification of a chirped pulse and its subsequent compression [11]. The pulse parameters were as follows: pulse energy $W \le 20$ mJ, wavelength $\lambda = 0.8$ μm, pulse duration $\tau \approx 85$ fs, and the repetition rate $F = 10$ Hz. The beam diameter D at the output of laser system was equal to 14 mm. Laser radiation was led into a vacuum chamber pumped to a pressure of 10^{-4} torr and focused by a spherical mirror onto the input capillary face. The capillary was placed at a three-coordinate translational stage with angular adjustment. The magnified image of the output capillary face was translated by another spherical mirror to a 12-bit CCD camera and the spectrograph input slit. The chamber was used to monitor the tuning of radiation passage through the capillary and to study the spatial structure of transmitted radiation. The spectra were recorded using a CCD array placed at the spectrograph output. The incident energy and the energy passed through the capillary were measured by calibrated photodiodes. Inert He and Ar gases were used in the experiments.

0021-3640/02/7609-0548$22.00

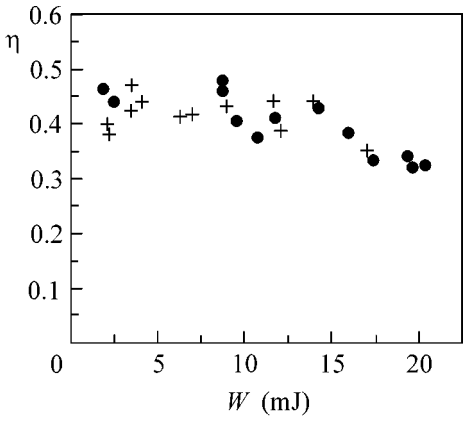

Fig. 1. Radiation transmission efficiency for the (●) evacuated and (+) Ar-filled capillary under a pressure of 1 torr. Gas ionization was observed at energies higher than 1 mJ.

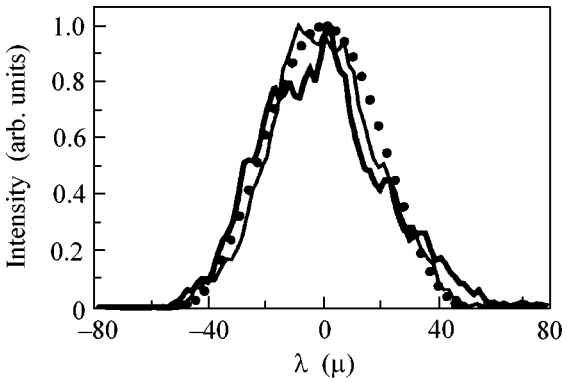

Fig. 2. Transverse intensity distribution for a beam at the output of the (thin line) evacuated capillary and (heavy line) Ar-filled capillary under a pressure of 1 torr. Points show the intensity distribution for the fundamental EH_{11} mode.

One of the main features of the capillary as a waveguide is energy loss caused by the loss of a portion of radiation into the shell [12]. The transmission efficiency η through the capillary (capillary input-to-output radiation-energy ratio) is determined by the efficiency η_{exc} of input beam transformation into the mode and by the energy loss upon the beam propagation in capillary: $\eta = \eta_{exc} e^{-\gamma L}$, where γ is the energy attenuation coefficient in capillary. For the fundamental mode EH_{11} of a glass capillary with diameter d = 100 μm and length L = 20 cm, used in most experiments, the calculated exponential factor was 0.65. The mode excitation efficiency was determined by calculating the overlap integral between the experimentally measured beam distribution focused on the capillary input and the EH_{11} mode distribution. It was found to be $\eta_{exc} = 0.7$, giving $\eta = 0.45$ for the transmission efficiency with allowance made for the radiation capillary passage loss. In Fig. 1, the experimentally measured transmission efficiency of a femtosecond radiation is given as a function of the incident pulse energy for an evacuated capillary and a capillary filled with Ar (at a pressure of 1 torr). Similar results were obtained with He at a pressure up to 3 torr. It follows from Fig. 1 that the plasma formation in the course of gas ionization at pressures studied has no effect on the transmission efficiency through the capillary. This suggests that plasma-induced energy losses are small, in accordance with the theoretical estimates. The observed decrease in the transmission efficiency for pulse energies ≥15 mJ is caused by the phase front distortion due to Kerr nonlinearity on the air path before the entrance into the vacuum chamber and in the input window of the vacuum chamber.

It is known that laser plasma appearing in the focus area may strongly affect, due to refraction, the radiation propagation process behind the focus. The plasma concentration n_{max}, for which the refraction becomes significant, can be estimated as [13]

$$n_{max} = n_c \theta^2, \quad (1)$$

where n_c is the critical plasma concentration and θ is half of the convergence angle of focused radiation. In the experiments with a capillary with a diameter of 100 μm, we had $n_{max} \approx 3 \times 10^{17}$ cm^{-3}, which corresponds to the gas pressure (for a single ionization) $p_{max} \approx 10$ torr. Our observations show that, in the case where the pressure was higher or on the order of p_{max}, the transmission efficiency through the capillary decreased appreciably and the capillary entrance face was rapidly (during few shots) destroyed. For this reason, the pressure in the experiments was limited by the pressure several times lower than its limiting value p_{max}.

The spatial structure of the output beam is an important characteristic of the propagation of a powerful laser radiation through the capillary. Figure 2 shows the pulse-averaged spatial intensity distribution at the capillary output for the incident pulse energy W = 20 mJ for a (thin line) capillary in vacuum and (thick line) Ar-filled capillary at a pressure of 1 torr. The points in Fig. 2 correspond to the squared zero-order Bessel function $J_0^2(r)$ describing the intensity distribution for the fundamental capillary mode EH_{11}. A comparison of the curves shows that the beam transverse structure at the capillary output in our experiments was close to the structure of fundamental mode, even in the presence of gas ionization. This signifies that the choice of gas-pressure working range given by Eq. (1) is correct.

Figure 3 presents the spectra of pulses passed through the capillary filled with Ar at pressure p = 1 torr for various pulse input energies. At the energy lower than the gas-ionization level, the spectrum at the capillary output coincided with the spectrum obtained for the evacuated capillary (thin line in Fig. 3). As the ion-

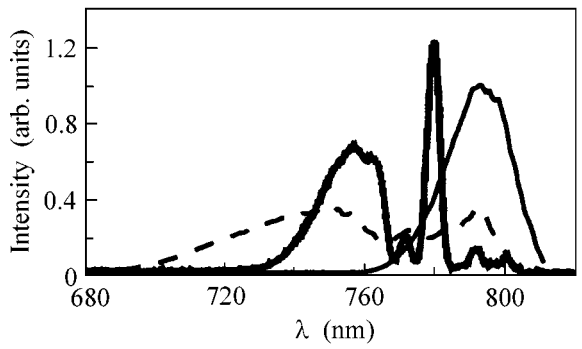

Fig. 3. Laser pulse spectrum at the output of a capillary filled with Ar under a pressure of 1 torr for an input pulse energy of (thin line) 1 mJ, (heavy line) 5 mJ, and (dashed line) 12 mJ; λ is the wavelength.

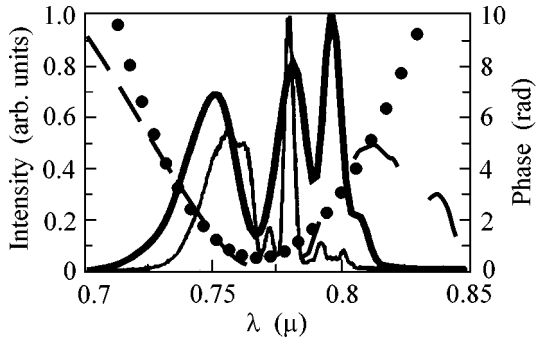

Fig. 4. The cross-section-averaged (heavy line) pulse spectral intensity and (dashed line) pulse phase at the capillary output and (points) the parabolic approximation of the phase frequency dependence. Thin line is the experimental spectrum.

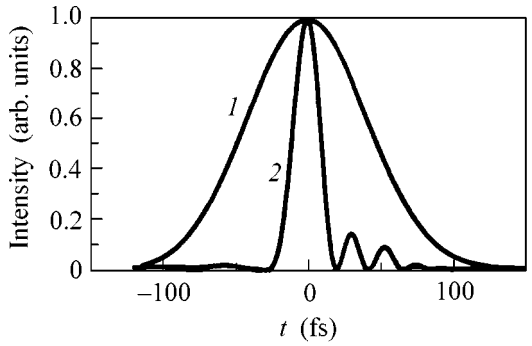

Fig. 5. (*2*) Pulse envelope (on the axis) with the compensation of quadratic frequency dependence of spectral phase and (*1*) envelope of the initial pulse.

ization threshold was exceeded, the output spectrum underwent short-wavelength shift. With an increase in the energy of incident pulse, the maximal shifts of central components increased. The maximal spectral "center-of-gravity" shift at the capillary output was as high as $\Delta\lambda \approx 20$–30 nm and comprised from two to three widths of the input pulse spectrum. The effective spectrum width was several times greater than its initial value. In He, the spectrum behavior was qualitatively the same, but, because of the higher ionization potential of He, spectral changes analogous to those in Ar occurred at higher incident pulse energies, and the maximal short-wavelength shift was smaller.

We carried out numerical simulation of laser pulse propagation in a capillary under the experimental conditions. To examine the laser pulse dynamics in a capillary, the paraxial equation was used for the complex envelope of a high-frequency field [$\mathbf{E} = \mathbf{x}_0 \hat{E} \exp(-i\omega_0\tau)$ + c.c], and the ionization balance equations

$$\left[\frac{2}{c}\frac{\partial}{\partial z}\left(i\omega_0 - \frac{\partial}{\partial\tau}\right) + \nabla_\perp^2\right]\hat{E} = k_p^2\hat{E}, \quad (2)$$

$$\frac{\partial n_1}{\partial\tau} = (1 - \sum n_i)W_1(\hat{E}) - n_1 W_2(\hat{E}), \quad (3)$$

$$\frac{\partial n_i}{\partial\tau} = n_{i-1}W_i(\hat{E}) - n_i W_{i+1}(\hat{E}), \quad (4)$$

$$\frac{\partial n_K}{\partial\tau} = n_{K-1}W_K(\hat{E}) \quad (5)$$

were used, where $\tau = t - z/c$, ω_0 is the initial field frequency, $k_p = \omega_p/c$, ω_p is the plasma frequency, c is the speed of light, n_i is the concentration of i-fold ionized ions, W_i is the ionization probability for the ith ion, and K is the maximal degree of ionization. To allow for the frequency shift of ionizing radiation, we retained the term $\partial^2/\partial z\partial\tau$ (small for a quasi-monochromatic field). In the laser intensity range used in the experiment, the gas ionization has a tunneling character, so that the ionization rates for atoms and ions were calculated using the ADK formula [14] with correction coefficients obtained for intensities in [15].

In Fig. 4, the intensity distribution is shown for the output pulse obtained in numerical simulation for the experimental conditions with an input pulse energy of 3.5 mJ. One can see from Fig. 4 that the results of numerical simulation are in a good qualitative agreement with the experiment. Among the main computational results, one should note the near-quadratic wavelength dependence of the spectral phase, in compliance with the results obtained in [10], where the idea of the powerful laser radiation compression by virtue of self-phase modulation compensation due to the ionization nonlinearity was suggested. The wavelength dependence of the spectral phase in the output pulse signifies that the frequency modulation caused by the nonlinear ionization of a gas in capillary can be compensated, to a large measure, during the pulse propagation in a linear medium with normal dispersion relations (e.g., in a quartz glass of the appropriate thickness). Figure 5 pre-

sents the calculated pulse intensity distribution (on the axis) after the compensation of quadratic phase upon passing through a quartz plate of thickness 3 cm and the intensity distribution for the initial pulse at the capillary output. One can see that the pulse compression is quite efficient: the pulse duration after a half-intensity compression is approximately 4.5 times shorter than at the capillary input.

To check for the possibility of realizing this effect, additional experiments were carried out. A single-pulse autocorrelator was built in the measuring scheme and fed with a portion of capillary output beam collimated by a long-focus mirror (with a focus length of 81 cm). For the pulse compression, plane-parallel compensating quartz plates of different length were placed at the autocorrelator input. In Fig. 6, the output autocorrelation function (ACF) is shown for the output pulse with the spectrum shown in Fig. 3 by the heavy line for a 3-cm-thick compensating plate. It follows from Fig. 6 that the pulse duration decreased to $\tau \approx 35$ fs, i.e., almost threefold compared to its initial value. In this case, the input pulse energy was 5 mJ and the energy of compressed pulse was ≈2 mJ, with account taken of the capillary losses. Estimates showed that the nonlinear phase incursion due to the nonlinear Kerr mechanism in quartz was ≤1, so that the effect of self-focusing nonlinearity on the temporal and spectral pulse characteristics could be ignored. One can see from Fig. 6 that, along with the highly compressed portion of the ACF, there are wings containing a considerable energy fraction of the output signal. These wings appear due to the incomplete phase compensation by the quartz plate. The incomplete phase compensation is caused by a poor quality of the input pulse and the nonideal compression in a glass plate. The complete phase compensation allows one to maximally compress the pulse if its duration is determined only by the spectral width. The optimal compression can be obtained by the inverse Fourier transform of the spectrum measured simultaneously with the ACF. As follows from Fig. 6, the duration of the optimally compressed pulse is approximately four times shorter than the duration of the initial laser pulse and is equal to 20 fs. It is significant that the pulse compression was uniform in cross-section, evidencing for the quasi-one-mode regime of radiation propagation in a capillary and the weakness of the effect of Kerr nonlinearity in the compensation plate on the radiation parameters.

It is worth noting that the presently existing compression schemes are based on the Kerr mechanism of nonlinear self-phase modulation of a powerful laser radiation propagating in the capillaries filled with a high-pressure (several atmospheres) gas [16, 17]. In this case, the maximal pulse energy is limited by the gas ionization threshold. In particular, one of the best results obtained in [17] demonstrates that, after the pulse compression, a pulse duration of 5 fs can be obtained at the capillary output for an energy of compressed pulse of ≈0.5 mJ and its initial duration of 20 fs.

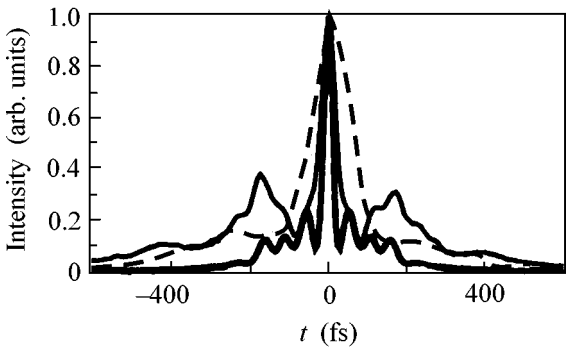

Fig. 6. (thin line) Autocorrelation function of a compressed pulse. The dashed line is for the autocorrelation function of a pulse passed through the evacuated capillary. Heavy line corresponds to the optimal compression.

The results obtained in this work demonstrate experimentally the compression scheme for the powerful laser pulses with the ionization mechanism of nonlinear self-phase modulation in capillaries filled by a low-pressure gas. In this scheme, no limitations are posed on the pulse energy in capillaries, which opens up the possibilities for obtaining extremely short high-energy (≥1 mJ) optical pulses.

In summary, the spectrum transformation of an intense femtosecond laser pulse has been experimentally studied under conditions of propagation in a gas-filled dielectric capillary, when the gas ionization has no effect on the efficiency of radiation propagation. It is shown that the initial spectrum broadens substantially (by several times) and its center of gravity shifts to short wavelengths. The results of numerical simulation are in a good qualitative agreement with the experiment. The compression (by several times) of the output pulse by virtue of the compensation of phase modulation arising due to the nonlinear field-induced gas ionization process was experimentally demonstrated. The results obtained open up the possibilities for generating ultrashort pulses with a duration of ≤10 fs and an energy of tens of millijoules.

This work was supported in part by the Russian Foundation for Basic Research (project nos. 02-02-16065, 01-02-17512, 02-02-06317, 01-02-18006), the Russian Academy of Sciences (project no. 1999-37), and INTAS (grant no. 97-10236).

REFERENCES

1. E. Esarey, P. Sprangle, J. Kroll, and A. Ting, IEEE Trans. Plasma Sci. **24**, 252 (1996).
2. B. Lemoff, G. Yin, C. Gordon III, *et al.*, Phys. Rev. Lett. **74**, 1574 (1995).
3. H. Milchberg, T. Clark, C. Durfee, *et al.*, Phys. Plasmas **3**, 2149 (1996).
4. S. Hooker, D. Spence, and R. Smith, J. Opt. Soc. Am. B **17**, 90 (2000).

5. S. Jackel, R. Burris, J. Grun, *et al.*, Opt. Lett. **20**, 1086 (1995).
6. M. Borghesi, A. J. Mackinnon, R. Gaillard, *et al.*, Phys. Rev. E **57**, R4899 (1998).
7. F. Dorchies, J. R. Marques, B. Cros, *et al.*, Phys. Rev. Lett. **82**, 4655 (1999).
8. B. Cros, C. Courtois, G. Malka, *et al.*, IEEE Trans. Plasma Sci. **28**, 1071 (2000).
9. Wm. Wood, C. Siders, and M. Downer, Phys. Rev. Lett. **67**, 3523 (1991).
10. G. Tempea and T. Brabec, Opt. Lett. **23**, 1286 (1998).
11. A. A. Babin, A. M. Kiselev, A. M. Sergeev, and A. N. Stepanov, Kvantovaya Élektron. (Moscow) **31**, 623 (2001).
12. E. Marcatili and R. Schmeltzer, Bell Syst. Tech. J. **43**, 1783 (1964).
13. V. B. Gil'denburg, Zh. Éksp. Teor. Fiz. **78**, 952 (1980) [Sov. Phys. JETP **51**, 480 (1980)].
14. M. V. Ammosov, N. B. Delone, and V. P. Kraĭnov, Zh. Éksp. Teor. Fiz. **91**, 2008 (1986) [Sov. Phys. JETP **64**, 1191 (1986)].
15. S. Augst, D. D. Meyerhofer, D. Strickland, and S. L. Chin, J. Opt. Soc. Am. B **8**, 858 (1991).
16. M. Nisoli, S. DeSilvestri, O. Svelto, *et al.*, Opt. Lett. **22**, 522 (1997).
17. S. Sartania, Z. Cheng, M. Lenzner, *et al.*, Opt. Lett. **22**, 1562 (1997).

Translated by V. Sakun

JETP Letters, Vol. 76, No. 9, 2002, pp. 553–557. From Pis'ma v Zhurnal Éksperimental'noĭ i Teoreticheskoĭ Fiziki, Vol. 76, No. 9, 2002, pp. 650–654.

On the Theory of Boson Peak in Glasses¶

V. L. Gurevich[1], D. A. Parshin[2], and H. R. Schober[3]

[1] *Solid State Physics Division, Ioffe Institute, Russian Academy of Sciences, St. Petersburg, 194021 Russia*
[2] *St. Petersburg State Technical University, St. Petersburg, 195251 Russia*
[3] *Institut für Festkörperforschung, Forschungszentrum, Jülich, D-52425 Jülich, Germany*

Received September 23, 2002

A universal mechanism of the Boson peak formation in glasses is proposed. The mechanism is based on the concept of interacting quasilocal oscillators. Even in the case of weak interaction, the low-frequency spectrum becomes unstable. Due to anharmonicity, the system undergoes a transition into a new stable configuration. As a result, below some characteristic frequency ω_c, proportional to the typical strength of interaction, the renormalized density of states becomes a universal function of ω with a Boson peak feature; i.e., the reduced density of states $g(\omega)/\omega^2$ has a maximum at a frequency $\omega_b \ll \omega_c$. We derive an analytic form of this function. © *2002 MAIK "Nauka/Interperiodica".*

PACS numbers: 61.43.Fs; 63.50.+x; 78.30.Ly

The purpose of the present paper is to propose a universal mechanism of Boson peak formation in glasses. The Boson peak (BP) is usually observed in a wide temperature range in the inelastic light- and neutron-scattering intensities at low frequencies, corresponding to a maximum in the reduced density of vibrational states $g(\omega)/\omega^2$ [1]. The position of this maximum correlates with a low-temperature bump in the reduced specific heat $C(T)/T^3$, where T is the temperature.

In spite of numerous efforts, there is no widely accepted theory of Boson peak phenomenon. An interesting feature is that the BP usually does not show up as a peak in the density of states (DOS) $g(\omega)$ itself but only in the reduced DOS, $g(\omega)/\omega^2$. A crucial question is whether this peak corresponds to phonon degrees of freedom or to some additional harmonic excitations in glasses, quasilocalized (resonant) modes (QLMs). In the first case, it would correspond either to an anomalous dispersion of the acoustic phonon excitations that has not been observed in experiment or to some low-lying optical modes. Disorder in an amorphous material would destroy the long-range coherence of optical modes. This makes a distinction between them and quasilocalized (resonant) modes impossible. Therefore, we base our theory of the Boson peak on harmonic excitations in glasses which coexist and interact with long-wavelength acoustic phonons (sound waves).

The QLMs (or broken up, low-lying optical modes) can be described as harmonic oscillators (HOs) that interact with the phonons [2–8]. QLMs are also found by numerical simulations; see [9] and references therein. Due to their interaction with phonons, they should inevitably interact with one another [10, 11]. This interaction can cause a mechanical instability of the system and the Boson peak phenomenon [12].

For illustration, consider a system of two interacting HOs with a potential energy

$$U_{\rm har}(x_1, x_2) = M_1\omega_1^2 x_1^2/2 + M_2\omega_2^2 x_2^2/2 - I_{12}x_1x_2. \quad (1)$$

Here, M_i are the masses and ω_i, are the frequencies of the two oscillators. The interaction strength is given by [11]

$$I_{12} = g_{12}J/r_{12}^3, \quad J \equiv \Lambda^2/\rho v^2, \quad (2)$$

where g_{12} accounts for the relative orientation of the HOs, r_{12} is their distance, ρ is the mass density of the glass and v is the sound velocity. The interaction between the HO is due to the coupling between a single HOs and the surrounding elastic medium (the glass). Possible additional short-range interactions do not introduce qualitative differences. The HO–phonon coupling has the form [7] $\mathcal{H}_{\rm int} = \Lambda x\varepsilon$, where Λ is the coupling constant and ε is the strain.

Diagonalization of Eq. (1) yields two frequencies

$$\tilde{\omega}_{1,2}^2 = \frac{\omega_1^2 + \omega_2^2}{2} \pm \sqrt{\left(\frac{\omega_1^2 - \omega_2^2}{2}\right)^2 + \frac{I_2^2}{M_1M_2}}. \quad (3)$$

The smaller value, $\tilde{\omega}_2^2$ becomes negative when I_{12} exceeds the threshold (critical) value $I_c \equiv \omega_1\omega_2\sqrt{M_1M_2}$. A negative $\tilde{\omega}_2^2$ indicates an instability of the corresponding eigenstate, *vibrational instability*—the previous minimum at $x_1 = x_2 = 0$ becomes a saddle point of the potential energy $U_{\rm har}(x_1, x_2)$.

This instability also persists in a system of many interacting HOs. However, in a real glass, an unstable HO is always stabilized by anharmonic forces into a

¶This article was submitted by the authors in English.

nearby minimum of the potential energy. The position of this minimum depends on the interaction between HOs. The new frequencies, in these new minima, are real and different from the original ones. Thus, the vibrational spectrum is reconstructed. This is the mechanism of the Boson peak formation.

Let us consider a system of randomly distributed, interacting HOs with an initial DOS, $g_0(\omega)$, where $g_0(\omega)$ is a monotonically increasing function of ω in the frequency range from 0 to ω_0 (it is normalized to 1). For the harmonic part of the interaction, we take the generalization of Eq. (1) and add an anharmonic term to stabilize the system

$$U_{\text{anhar}} = (A/4)\sum_i x_i^4. \tag{4}$$

We will consider the interaction I_{ij} between the oscillators to be a *small parameter* of our theory. Namely, we assume that the typical random interaction I between neighboring HOs is much smaller than the typical values of the product $M\omega_0^2$. As $|I| \ll M\omega_0^2$, the frequencies on the order of ω_0 will be practically unaffected by the interaction, whereas HOs with frequencies

$$\omega < \omega_c \simeq |I|/M\omega_0 \ll \omega_0 \tag{5}$$

will be displaced to new minima.

Since the concentration of unstable HOs is much smaller than that of the stable ones, a low-frequency oscillator is usually surrounded by high-frequency ones. Therefore, we can split our problem into two parts. First we consider a cluster containing a low-frequency oscillator with frequency $\omega_1 \lesssim \omega_c$ which is surrounded by a large number N of HOs with much higher frequencies $\omega_j \sim \omega_0$. To determine the eigenfrequencies of the interacting oscillators belonging to the cluster, one should solve the secular equation on the order of $N + 1$ in ω^2. However, the variations of the high eigenfrequencies should be small and can be discarded as they are proportional to the small parameter $I/M\omega_0^2$. As a result, one gets for the smallest eigenfrequency a linear equation. It can easily be solved, and one can show that such a cluster becomes unstable under the condition

$$M_1\omega_1^2 < k, \quad \text{where} \quad k \equiv \sum_j \frac{I_{1j}^2}{M_j\omega_j^2}. \tag{6}$$

For the unstable situation, one has to take the anharmonicity, Eq. (4), into account. The new low frequency of the coupled oscillators is then given by

$$\tilde{\omega}_1^2 = \begin{cases} \dfrac{1}{M_1}(M_1\omega_1^2 - k), & k < M_1\omega_1^2 \\ \dfrac{2}{M_1}(k - M_1\omega_1^2), & k > M_1\omega_1^2. \end{cases} \tag{7}$$

It is remarkable that the anharmonicity which has been used in deriving the second Eq. (7) does not in the end enter this equation of our final result, Eq. (20).

Thus, the derivation of the new (reconstructed) DOS amounts to a calculation of the distribution of k, $\rho(k)$. Inserting Eqs. (2) and (6) into the definition of $\rho(k)$ gives

$$\rho(k) = \left\langle \delta\left(k - \frac{J^2}{M}\sum_j \frac{g_{1j}^2}{r_{1j}^6\omega_j^2}\right)\right\rangle. \tag{8}$$

Here, the angular brackets denote the averaging over the positions of the N high-frequency HOs, their frequencies, and orientations. For simplicity, we take equal masses $M_j = M$ and for g_{ij}, a uniform distribution in the interval $[-1/2, 1/2]$.

Using the Holtsmark method [13], one gets

$$\rho(k) = \frac{1}{\sqrt{2\pi}}\frac{B}{k^{3/2}}\exp\left(-\frac{B^2}{2k}\right), \tag{9}$$

where

$$B = \frac{1}{3}(2\pi)^{3/2}\frac{Jn}{\sqrt{M}}\left\langle\frac{1}{\omega}\right\rangle_0 \equiv \omega_c\sqrt{M}. \tag{10}$$

Here, n is the concentration of HO and $\langle 1/\omega\rangle_0$ is the ω^{-1} moment of the initial DOS $g_0(\omega)$. This formula is the definition of the characteristic frequency ω_c introduced by order of magnitude in Eq. (5). $Jn \simeq I$ is the typical interaction between the nearest neighbors and $\langle 1/\omega\rangle_0 \simeq 1/\omega_0$. We assume that the average $\langle 1/\omega\rangle_0$ is finite; i.e., at small ω, the initial DOS $g_0(\omega) \propto \omega^n$ with $n > 0$.

The DOS is reconstructed to $\tilde{g}(\omega) = \tilde{G}(\omega^2)/2\omega$, where

$$\begin{aligned}\tilde{G}(\omega^2) &= \langle\delta(\omega^2 - \tilde{\omega}_1^2)\rangle_{k,\omega_1} \\ &\equiv \int_0^\infty dk\,\rho(k)\int_0^\infty d\omega_1^2 G_0(\omega_1^2)\delta(\omega^2 - \tilde{\omega}_1^2)\end{aligned} \tag{11}$$

and $G_0(\omega_1^2) \equiv g_0(\omega_1)/2\omega_1$. Using Eq. (7) and integrating Eq. (5), we obtain

$$\begin{aligned}\tilde{G}(\omega^2) &= \frac{1}{2}\int_0^\infty dk\,\rho\left(k + \frac{1}{2}M\omega^2\right)G_0\left(\frac{k}{M}\right) \\ &\quad + \int_0^\infty dk\,\rho(k)G_0\left(\omega^2 + \frac{k}{M}\right).\end{aligned} \tag{12}$$

As one can see, for $\omega \ll \omega_c$, $\tilde{G}(\omega^2) = \text{const}$, so that $\tilde{g}(\omega) \propto \omega$; i.e., the reconstructed DOS appears to be a *linear function* of ω. For high frequencies, the first term

in Eq. (12) can be discarded and the original DOS is reproduced, $\tilde{G}(\omega^2) = \tilde{G}_0(\omega^2)$ for $\omega \gg \omega_c$.

If the low-frequency HOs with their reconstructed linear DOS were isolated, the problem would be solved. There is, however, a further interaction between these HOs, which we will take into account in the second step of our procedure. The low frequency HOs, displaced from their equilibrium positions, create random static forces f. The force f_i acting on the ith oscillator from the jth one is

$$f_i = I_{ij}x_{j0}. \tag{13}$$

In the presence of anharmonicity, this again reconstructs the low frequency part of the spectrum (cf. [6]). Consider an anharmonic potential variation under the action of a random static force f, so that $U(x) = Ax^4/4 + M\omega_1^2 x^2/2 - fx$, with ω_1 the oscillator frequency in the harmonic approximation. Under the action of f, the equilibrium position shifts from $x = 0$ to x_0 satisfying the equilibrium equation

$$Ax_0^3 + M\omega_1^2 x_0 - f = 0. \tag{14}$$

In the new equilibrium position, the oscillator, in the harmonic approximation, acquires the eigenfrequency

$$\omega_{\text{new}}^2 = \omega_1^2 + 3Ax_0^2/M. \tag{15}$$

If $\tilde{g}_1(\omega_1)$ is the distribution function of frequencies ω_1 and $P(f)$ is the distribution of random forces, then one gets the new equilibrium DOS

$$g(\omega) = \int_0^\infty \tilde{g}_1(\omega_1)d\omega_1 \int_{-\infty}^{\infty} df P(f)\delta(\omega - \omega_{\text{new}}). \tag{16}$$

As the forces between the HOs are proportional to r_{ij}^{-3}, they have a Lorentzian distribution:

$$P(f) = \frac{1}{\pi}\frac{\delta f}{f^2 + (\delta f)^2}. \tag{17}$$

Assuming $\omega \ll \omega_c$ and integrating Eq. (16) with $\tilde{g}_1(\omega_1) = C\omega_1$, we get

$$\frac{g(\omega)}{\omega^2} = \frac{6C}{\pi\omega^*}\left(\frac{\omega}{\omega^*}\right)^2 \int_0^1 \frac{dt}{1 + (\omega/\omega^*)^6 t^2(3 - 2t^2)} \tag{18}$$

with

$$\omega^* = \sqrt{3}A^{1/6}(\delta f)^{1/3}/\sqrt{M}. \tag{19}$$

Finally,

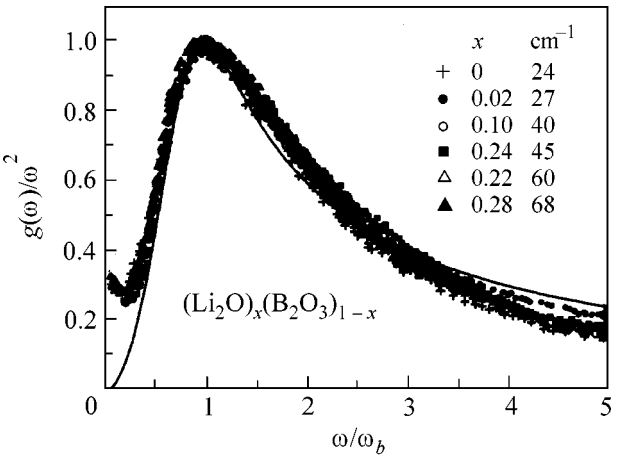

Fig. 1. The Boson peak in reduced units: Eq. (20) (solid line) and Raman data for lithium borate glasses [14]. The positions of the BP (for different compositions x) are given in cm^{-1}.

$$\frac{g(\omega)}{\omega^2} = \frac{3C}{\pi\omega^*}\left(\frac{\omega^*}{\omega}\right)^4 [z_1^2(\omega) + z_2^2(\omega)]^{-1} \times \left[\frac{1}{2z_1(\omega)}\ln\frac{z_1(\omega)+1}{z_1(\omega)-1} + \frac{1}{z_2(\omega)}\arctan\frac{1}{z_2(\omega)}\right], \tag{20}$$

where

$$z_{1,2}(\omega) = \frac{1}{2}\sqrt{\sqrt{9 + 8(\omega^*/\omega)^6} \pm 3}.$$

The function $g(\omega)/\omega^2$ is plotted in Fig. 1. It depends on a single parameter, ω^*. The maximum of $g(\omega)/\omega^2$, i.e., the Boson peak, is at $\omega_b \approx 1.1\omega^*$. For large frequencies, $\omega \gg \omega_b$, $g(\omega) \propto \omega$, while for small frequencies, $\omega \ll \omega_b$, $g(\omega) \propto \omega^4$. Also shown is a comparison of our theoretical curve with Raman scattering data for lithium borate glasses [14] of different compositions. These results are in a rather good agreement with the experimental data and support the idea of a universal form of the Boson peak [15].

The Boson peak frequency, $\omega_b \approx 1.1\omega^*$, is determined by the characteristic value of the random force δf, Eq. (19) acting on an HO with the characteristic frequency ω_c. According to Eq. (13), it is due to the interaction between HOs with frequencies on the order of ω_c; i.e., $|I_{ij}^{(c)}| \simeq Jn_c$, $J \simeq M\omega_c/g_0(\omega_0)$, where $n_c \simeq g_0(\omega_c)\omega_c$ is the concentration of these HOs. The characteristic displacement of the HO from the equilibrium position is $x_0 \simeq \omega_c\sqrt{M/A}$. As a result, we get the estimate

$$\omega_b \simeq \omega_c[g_0(\omega_c)/g_0(\omega_0)]^{1/3}, \quad \omega_b \ll \omega_c. \tag{21}$$

We tested these ideas by numerical simulation. N oscillators with frequencies $0 < \omega_i < 1$ were placed on a

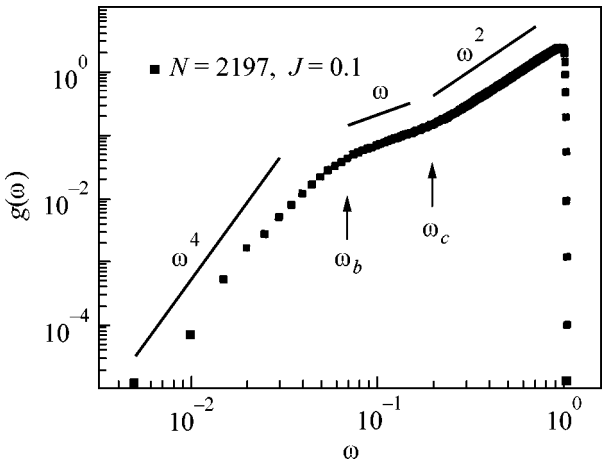

Fig. 2. Simulated density of states ($g_0(\omega) \propto \omega^2$, $N = 2097$) in a log–log representation. The arrows indicate two characteristic frequencies ω_b and ω_c.

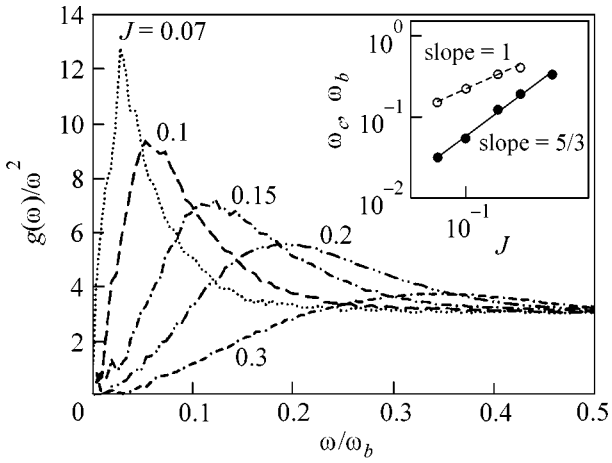

Fig. 3. Simulated $g(\omega)/\omega^2$ for different interaction strengths with $g_0(\omega) \propto \omega^2$, $N = 2097$ and $N = 4096$ ($J = 0.07$). The insert shows the scaling of the crossover frequencies ω_c (○) and ω_b (●) with the interaction strength J.

simple cubic lattice with lattice constant $a = 1$ and periodic boundary conditions. For random orientations of the oscillators, g_{ij}, Eq. (2), we took random numbers in the interval [–0.5, 0.5]. The anharmonicity parameter, A, and the masses of the oscillators, M_i, were set equal to 1. The initial DOS for the noninteracting HOs was taken as $g_0(\omega) \propto \omega^n$, with $n = 1, 2, 3$. We minimized the potential energy and calculated the DOS in the harmonic approximation (around this minimum) for different interaction strengths, J. This procedure was repeated for 10000 representations. To check for size dependence, we did the calculations for different N. Except for the case $J = 0.07$, the results did not change between $N = 2097$ and $N = 4096$. The results also did not change by introduction of the cubic anharmonicity.

Figure 2 shows $g(\omega)$ for $g_0(\omega) \propto \omega^2$ and $J = 0.1$ in a log–log representation. The predicted crossovers in the ω dependence of the DOS are clearly observed at two characteristic frequencies ω_c and ω_b. From the calculated eigenvectors, we find that, as expected, near and above ω_b, the eigenmodes are complicated superpositions of many HOs, whereas at the lowest frequencies, the HOs are weakly coupled.

The dependence of the reconstructed DOS $g(\omega)/\omega^2$ on the interaction strength J is illustrated in Fig. 3. One can see the general increase of ω_b and related decrease of the Boson peak intensity with increasing J. This result agrees with recent experiments [16] and molecular-dynamic simulations [17]. Our simulations cover one decade in Boson peak frequencies. The insert shows that, in full agreement with our predictions (see Eq. (5) and Eq. (4)), the crossover frequencies change with interaction J as $\omega_c \propto J$ and $\omega_b \propto J^{1+n/3}$.

In this letter, we dealt with the case of weak interaction between HOs. If the interaction is increased, the characteristic frequencies ω_b and ω_c grow, and the gap between them narrows and finally disappears. Then our Boson peak in $g(\omega)/\omega^2$ superimposes the "boundary peak" in $g_0(\omega)$ at the edge of the original vibrational spectrum. The Boson peak can no longer be distinguished from the boundary peak in $g(\omega)$ or from a possible equivalent maximum in $g_0(\omega)$. A similar case with strong coupling between oscillators was investigated in [10] by means of molecular-dynamic simulations and in [18] using the replica method.

In conclusion, we present a universal picture of the Boson peak formation in glasses where stabilization of the system of weakly coupled harmonic modes by anharmonicity is essential. The principal new result of our approach, compared to previous work, is that the Boson peak emerges naturally on the unstructured flat low-frequency part of the initial spectrum $g_0(\omega)/\omega^2$, where no peaks in the DOS existed before. For small interactions, the Boson peak frequency is much smaller than the Debye frequency value. It shifts with interaction strength, I which explains the large variety of Boson peak magnitudes found in experiment.

The authors VLG and DAP gratefully acknowledge the financial support of the German Ministry of Science and Technology and the hospitality of the Forschungszentrum Jülich, where part of the work was done. VLG is pleased to acknowledge the support for this work by the Russian Foundation for Basic Research (project no. 00-15-96748).

REFERENCES

1. *Amorphous Solids. Low Temperature Properties*, Ed. by W. A. Phillips (Springer-Verlag, Berlin, 1981).

2. V. G. Karpov, M. I. Klinger, and F. N. Ignatiev, Zh. Éksp. Teor. Fiz. **84**, 760 (1983) [Sov. Phys. JETP **57**, 439 (1983)].
3. V. G. Karpov and D. A. Parshin, Pis'ma Zh. Éksp. Teor. Fiz. **38**, 536 (1983) [JETP Lett. **38**, 648 (1983)]; Zh. Éksp. Teor. Fiz. **88**, 2212 (1985) [Sov. Phys. JETP **61**, 1308 (1985)].
4. U. Buchenau, N. Nücker, and A. J. Dianoux, Phys. Rev. Lett. **53**, 2316 (1984).
5. M. A. Krivoglaz, Zh. Éksp. Teor. Fiz. **88**, 2171 (1985) [Sov. Phys. JETP **61**, 1284 (1985)].
6. M. A. Il'in, V. G. Karpov, and D. A. Parshin, Zh. Éksp. Teor. Fiz. **92**, 291 (1987) [Sov. Phys. JETP **65**, 165 (1987)].
7. U. Buchenau, Yu. M. Galperin, V. L. Gurevich, *et al.*, Phys. Rev. B **46**, 2798 (1992).
8. D. A. Parshin, Fiz. Tverd. Tela (St. Petersburg) **36**, 1809 (1994) [Phys. Solid State **36**, 991 (1994)].
9. B. B. Laird and H. R. Schober, Phys. Rev. Lett. **66**, 636 (1991); H. R. Schober and B. B. Laird, Phys. Rev. B **44**, 6746 (1991); H. R. Schober and C. Oligschleger, Phys. Rev. B **53**, 11469 (1996); C. Oligschleger, Phys. Rev. B **60**, 3182 (1999).
10. E. R. Grannan, M. Randeria, and J. P. Sethna, Phys. Rev. B **41**, 7799 (1990).
11. V. L. Gurevich, D. A. Parshin, J. Pelous, and H. R. Schober, Phys. Rev. B **48**, 16318 (1993).
12. V. L. Gurevich, D. A. Parshin, and H. R. Schober, cond-mat/0203165.
13. S. Chandrasekhar, Rev. Mod. Phys. **15**, 1 (1943).
14. S. Kojima and M. Kodama, Physica B (Amsterdam) **263**, 336 (1999).
15. V. K. Malinovsky and A. P. Sokolov, Solid State Commun. **57**, 757 (1986); V. K. Malinovsky, V. N. Novikov, P. P. Parshin, *et al.*, Europhys. Lett. **11**, 43 (1990).
16. O. Yamamuro, K. Takeda, I. Tsukushi, and T. Matsuo, Physica B (Amsterdam) **311**, 84 (2002); Y. Inamura, M. Arai, M. Nakamura, *et al.*, J. Non-Cryst. Solids **293**, 389 (2001); Y. Inamura, M. Arai, O. Yamamuro, *et al.*, Physica B (Amsterdam) **263–264**, 299 (1999).
17. P. Jund and R. Jullien, J. Chem. Phys. **113**, 2768 (2000).
18. R. Kühn and U. Horstmann, Phys. Rev. Lett. **78**, 4067 (1997).

JETP Letters, Vol. 76, No. 9, 2002, pp. 558–562. From Pis'ma v Zhurnal Éksperimental'noĭ i Teoreticheskoĭ Fiziki, Vol. 76, No. 9, 2002, pp. 655–659.

Alternative Approach for Evaluation of Mössbauer Spectra of Nanostructured Ferromagnetic Alloys within Generalized Two-Level Relaxation Model¶

M. A. Chuev[1], O. Hupe[2], A. M. Afanas'ev[1], H. Bremers[2], and J. Hesse[2]

[1] *Institute of Physics and Technology, Russian Academy of Sciences, Moscow, 117218 Russia*

[2] *Institut für Metallphysik und Nukleare Festkörperphysik, Technische Universität 38106 Braunschweig, Germany*

Received September 27, 2002

The simplest treatment of the complex ^{57}Fe Mössbauer absorption spectra of nanostructured Fe–Cu–Nb–B alloys within the recently developed generalized two-level relaxation model has been successfully performed. This model applied for a system of superparamagnetic particles allows one to take into account the interparticle interaction in a simpler form and to describe qualitatively a specifically asymmetric shape of Mössbauer lines with sharp outer and smeared inward sides when the conventional two-level relaxation model fails. The approach is actually an alternative way in order to evaluate the Mössbauer spectra of nanostructured ferromagnetic alloys without taking into consideration a rather wide and diverse distribution over the particle sizes.

PACS numbers: 61.18.Fs; 61.46.+w; 76.80.+y

We report the first experimental evidence for the success of the generalized two-level relaxation (GTLR) model recently introduced in order to understand Mössbauer spectra of nanostructured magnetic alloys [1]. Studies of these alloys by means of different techniques are of great interest for both fundamental and technological reasons. The most attractive are the structural and magnetic properties of these alloys, so that the ^{57}Fe Mössbauer spectroscopy appears to be an excellent tool for characterization of the iron-based nanostructured materials [2–6]. These materials are produced by the partial devitrification of amorphous alloys, and consist structurally of nanosized crystalline bcc iron grains (NG) with a long-range order and a residual amorphous matrix that exhibits short-range order. As a result, the Mössbauer spectra of the materials look like a superposition of the well-resolved hyperfine magnetic structure corresponding to NG and strongly broadened magnetic component with a lower average hyperfine field, which is usually associated with the amorphous phase (see Fig. 1). In spite of the large amount and diversity of the experimental spectra of various nanostructured materials, there still remain principal difficulties and even contradictions in the treatment of data.

The most popular approach for evaluation of Mössbauer spectra of nanostructured ferromagnetic alloys is taking into consideration continuous distributions of the hyperfine field H_{hf} [7], which should describe, first of all, a distribution over the particle sizes in such inhomogenious materials. This method has allowed researchers to restore the temperature dependencies of the H_{hf} average values and widths of their distribution for NG and amorphous phase, as well as to justify the presence and evaluate the parameters of so-called interface zones between NG and matrix [2, 6]. However, the results obtained within the method often suffer from some ambiguity. First, the widths of the H_{hf} distribution require for their explanation a rather wide distribution over particle size, which is often not confirmed by complementary methods. On the other side, the sizes of NG in the nanostructured materials are regarded to be rather small (for instance, the average size of particles in the $Fe_{86-x}Cu_1Nb_xB_{13}$ alloys was estimated to be about 2–4 nm from transmission-electron-microscopy measurements [8]) so that the particles should demonstrate superparamagnetic relaxation at finite temperatures.

The simplest way to describe the relaxation effects on the Mössbauer line shape is to use the two-level relaxation (TLR) model [9], within which only two energy states corresponding to opposite directions of the particle's magnetic moment along the easy magnetization axes are considered, so that jumps from one state to the other are determined by the energy barrier U_0 between them (Fig. 2, left). The Neel formula is used to describe the temperature-dependent transition rate [10]:

$$p = p_0 \exp(-U_0/k_B T), \qquad (1)$$

where p_0 is slightly dependent on temperature. According to the model, if the relaxation rate is comparable or larger than the natural Mössbauer linewidth Γ_0 (which is just the case for the iron nanosized particles at room temperature and higher), the relaxation reveals itself in

¶This article was submitted by the authors in English.

the Mössbauer spectra with temperature increasing as a remarkable broadening of spectral lines followed by shifts of the widely broadened lines to the center of the spectra and a collapse of the magnetic hyperfine structure into a single central line or quadrupole doublet at higher temperatures [1, 9].

At first glance, the temperature evolution of Mössbauer spectra of nanostructured ferromagnetic alloys (like those shown in Fig. 1) exhibits behavior of just this kind, which is why some investigators have tried to evaluate the spectra within the relaxation effects [4]. The pressing point here is just the consequence of the two-level relaxation model that, at any stage of relaxation in the transition region from a well-resolved hyperfine magnetic structure to its collapse, the broadening of spectral lines should be principally of a Lorentzian type; i.e., the relaxation should result in the appearance of long Lorentzian tails in the spectrum, which could be easily registered by means of careful fitting of the spectrum. Earlier [6], we performed such a detailed analysis of the Mössbauer spectra of nanostructured $Fe_{86-x}Cu_1Nb_xB_{13}$ alloys using the powerful DISCVER method [11] but failed to find any traces of the conventional relaxation effects (i.e., the presence of additional Lorentzian tails in the spectra) up to higher temperatures where the collapse effect occurs.

However, the most striking feature of Mössbauer spectra of nanostructured ferromagnetic alloys is a specifically asymmetric shape of the spectral lines with sharp outer and smeared inward sides, and even stairs-like shape at higher temperatures (see Fig. 1), which is experimentally observed in almost every other work published in the field (see, e.g., [2–6] and references therein). Lines of this unusual form have been observed earlier in many studies of systems with superparamagnetic particles [12, 13] and could not fit the conventional two-level relaxation model without taking into account a rather wide distribution over the particle sizes, i.e., over the magnetic anisotropy energies U_0 and relaxation parameters p_0 [14]. Note that a much more complicated multilevel relaxation model with a log-normal particle-size distribution has successfully described the Mössbauer spectra of real fine-particle systems, but no qualitative distinction between effects of the two factors on the line-shape evolution with temperature has been given [15].

A qualitatively new explanation for Mössbauer line shapes of this kind has recently been suggested in theoretical work [1], where a generalization of the TLR model has been performed. In the present study, we have applied this GTLR model for a qualitative treatment of the Mössbauer spectra of the nanostructured $Fe_{79}Cu_1Nb_7B_{13}$ alloys with average NG size of about 4 nm and different NG content, measured in the temperature range from 300 K to 700 K. Because of the great importance of qualitative consequences of the new GTLR model for superparamagnetic relaxation as a whole and for studies of nanostructured magnetic materials in particular, below we will stay within the simplest possible assumptions taken in [1].

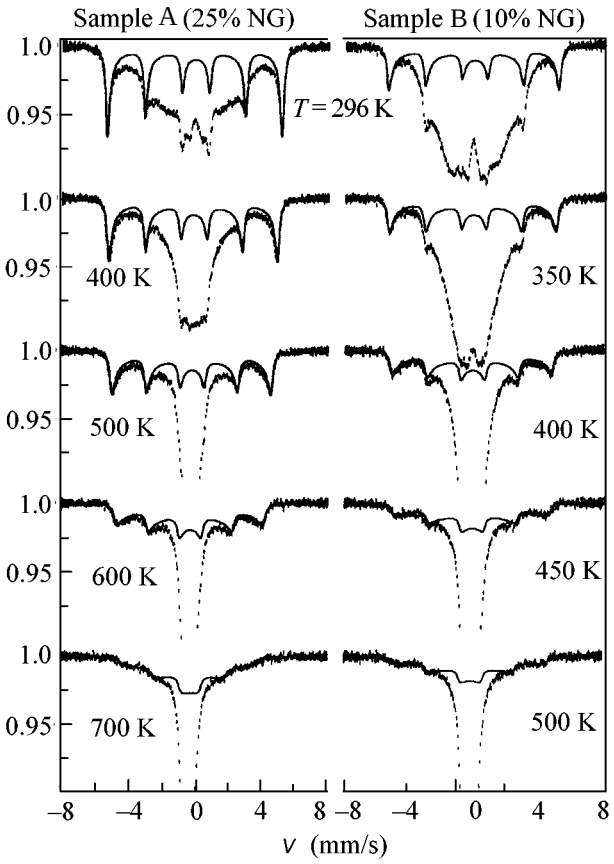

Fig. 1. Temperature evolution of ^{57}Fe Mössbauer spectra (bars) of the nanostructured ferromagnetic $Fe_{79}Cu_1Nb_7B_{13}$ alloys with different content of nanograins: 25% NG (left) and 10% NG (right). Solid lines are calculated within the generalized two-level relaxation model for the outermost hyperfine magnetic component corresponding to NG of the same size with different energy distribution widths σ.

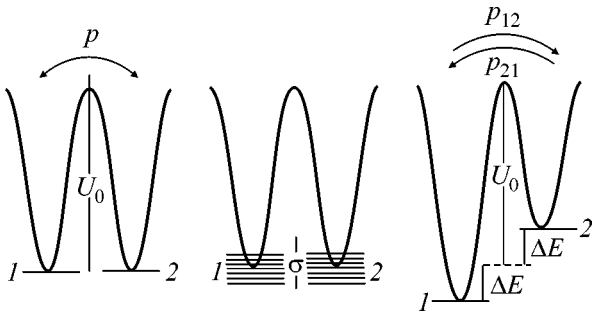

Fig. 2. Two-level relaxation model for a single superparamagnetic particle (left), generalized two-level relaxation model for a particle interacting with environment (center); two-level scheme for a particle interacting with environment at given ΔE (right).

The principal postulate of the GTLR model is that the relaxation between the particle's states with opposite directions of its magnetic moment never occurs as a transition between the states of the same energy, because even weak interaction with the environment should inevitably smear out the energy levels (Fig. 2, center). In a system like nanostructured ferromagnetic alloys with a great number of degrees of freedom, the energy levels of each particle at a certain time prove to be separated by a certain gap ΔE (Fig. 2, right), and the average value σ of distribution over ΔE may be rather large and comparable to temperature. Such a separation of the energy levels results in different values of the relaxation rates, $p_{12}(\Delta E)$ and $p_{21}(\Delta E)$, from one state to the other and vice versa, followed by a difference in equilibrium populations of these states from the detailed balance principle. As a result, the shape of the Mössbauer absorption spectrum and its temperature evolution changes drastically [1, 9].

Following the assumption of the conventional TLR model that the hyperfine field at the nucleus can only be reversed during the relaxation and the results obtained in [1], one can easily derive the following expression for the cross section of gamma-ray quantum absorption for a given ΔE:

$$\varphi(\omega, \Delta E) = -\frac{\sigma_a \Gamma_0}{2} \times \sum_\alpha |C_\alpha|^2 \mathrm{Im} \frac{\bar{\omega} + i\bar{p} + (\Delta p/\bar{p})\omega_\alpha}{\bar{\omega}^2 - \omega_\alpha^2 + \bar{p}^2 - 2i\Delta p \omega_\alpha}, \quad (2)$$

where $\bar{\omega} = \omega + i(\Gamma_0/2 + \bar{p})$, $\alpha = (M, m)$ labels the hyperfine transitions between the ground and excited states with nuclear spin projections m and M onto the direction of the hyperfine field, $\omega_\alpha = M\omega_e - m\omega_g$, $\omega_{e,g} = g_{e,g}\mu_N H_{hf}$, μ_N is the nuclear magneton, $g_{g,e}$ is the nuclear g factor for the ground and excited states, C_α determines the intensity of the corresponding transition, σ_α is the effective absorber thickness,

$$\bar{p} \equiv \bar{p}(\Delta E) = \frac{p_{12}(\Delta E) + p_{21}(\Delta E)}{2}, \quad \text{and} \quad \Delta p \equiv \Delta p(\Delta E) = \frac{p_{21}(\Delta E) - p_{12}(\Delta E)}{2}. \quad (3)$$

It is clearly seen that, in the absence of interaction ($\Delta E = 0$, $\bar{p} = p$, $\Delta p = 0$), Eq. (2) is reduced to the well-known expression for the absorption spectrum within the conventional TLR model [9].

From the physical point of view, the ΔE values must be random variables spread over a certain interval, and the simplest ΔE distribution function can be chosen in the Gaussian form:

$$P(\Delta E, \sigma) = \frac{1}{\sqrt{2\pi}\sigma} \exp\left(-\frac{(\Delta E)^2}{2\sigma^2}\right). \quad (4)$$

Then, the averaged absorption cross section is naturally determined by the energy distribution width σ:

$$\bar{\varphi}(\omega) = \int_{-\infty}^{\infty} \varphi(\omega, \Delta E) P(\Delta E, \sigma) d(\Delta E). \quad (5)$$

Using Eqs. (2)–(5), one can easily calculate the absorption spectrum within the GTLR model, provided that the relaxation parameters $p_{12}(\Delta E)$ and $p_{21}(\Delta E)$ are given; i.e., the values of energy maxima and minima shown in Fig. 2 (right) should be determined. In the simplest case of weak interaction ($\Delta E \ll U_0$), the relaxation parameters can be written in the form

$$p_{21,12}(\Delta E) = p \exp(\pm \Delta E / k_B T), \quad (6)$$

where p is defined by Eq. (1). In this case, as clearly seen from comparison of Eqs. (1)–(6), the averaged absorption spectrum $\bar{\varphi}(\omega)$ is completely defined by only three parameters: p_0, U_0, and the ratio of the energy distribution width to temperature, $\sigma/k_B T$. As has been shown already in [1], the relaxation Mössbauer spectra calculated within this scheme differ drastically from those of the TLR model, and the most salient feature of the GTLR spectra is just the appearance of asymmetrically shaped lines with extended inward wings.

Since the asymmetrical lineshape is clearly seen in the spectra of nanostructured $Fe_{79}Cu_1Nb_7B_{13}$ alloys shown in Fig. 1, we have tried to fit the data within the GTLR model. However, in order to analyze spectra of such a high level of complexity in detail, one needs first to develop a strategy of analysis and corresponding computer program like DISCVER [11], which, of course, takes time. That is why, at this first stage of analysis, we have decided to restrict ourselves to fitting only the most distinguishable contribution into the spectra with the highest value of hyperfine field, which obviously comes from nanocrystalline grains. We have performed simultaneous fitting of the whole temperature series of spectra for each sample over the outermost velocity ranges including only outer lines of magnetic sextet corresponding to NG. The adjustable parameters in the course of fitting were p_0 and U_0, the same for all spectra of each sample, as well as hyperfine field, isomer shift, and σ for each spectrum of the sample. In order to avoid unphysical solutions due to the restrictions on the fitting velocity ranges, the variable parameter was also the spectral area of only one spectrum of the series, while others were bonded by the ratios of total areas of corresponding spectra, which were estimated independently with rather good accuracy [6].

Results of the analysis are shown as solid curves in Fig. 1, and temperature depedences of the values, of hyperfine field H_{hf} and energy distribution width σ for both the samples studied are displayed in Fig. 3. As clearly seen, Fig. 1 demonstrates a good description of

the outermost lines of all the spectra, as well as almost complete accordance between the calculated curves and resolved magnetic hyperfine structure (with lines of strongly asymmetrical shape mentioned above) at temperatures higher than the Curie temperature of amorphous phase for both the samples. Remembering that solid lines in Fig. 1 are calculated within the GTLR model for the only hyperfine magnetic component corresponding to NG of the same size, one can understand that, in this case, there is no need to introduce a broad distribution of particle size, at least for this NG phase even at higher temperatures, because the relaxation of interacting particles can result in the specific broadening of the spectral lines. In any case, it is clear that, although the GTLR model does not principally deny the particle's distribution over sizes, taking into account the interparticle interaction should strongly modify the shape of the distributions obtained by conventional methods.

There is one more interesting result of physical meaning. As Fig. 3 shows, despite the considerable difference between the temperature evolution of Mössbauer spectra for the two samples studied, the hyperfine-field values for nanograins in these samples are practically the same up to higher temperatures and slightly deviate from the temperature dependency of bulk values of hyperfine field in pure iron. At the same time, the difference in the temperature evolution of the spectra for the two samples, as well as the forms of this evolution mentioned above, seem to be governed by the temperature dependence of energy distribution width σ characterizing interparticle interactions. At least, it is obviously seen in Fig. 3 that the $\sigma(T)$ dependences exhibit remarkable changes in the interactions just above the Curie temperature of amorphous phase for both the samples, which again evidences an essential interrelation between the magnetic behavior of NG and amorphous matrix.

As for the relaxation parameters p_0 and U_0, they appeared to be equal to $(1.0 \pm 0.8) \times 10^{11}$ s^{-1} and 1100 ± 300 K, respectively, just indicating that the fast relaxation regime is realized for nanograins in both the samples down to room temperature. Moreover, large mean-square errors in these parameters justify this conclusion, because, in the case of fast relaxation, the absorption cross section becomes slightly dependent on the relaxation rate p, i.e., on p_0 and U_0. Indeed, the fast-relaxation regime, from the physical viewpoint, means very fast fluctuations between the energy states of a particle, so that the nucleus should "feel" only the stochastically averaged hyperfine field defined by the difference of the equilibrium populations, $w_1(\Delta E)$ and $w_2(\Delta E)$, of the states at a given ΔE:

$$\bar{H}_{hf}(\Delta E) = [w_1(\Delta E) - w_2(\Delta E)]H_{hf}. \quad (7)$$

As follows from the detailed balance principle,

$$w_1(\Delta E) - w_2(\Delta E) = \Delta p/\bar{p} = \tanh(\Delta E/k_B T), \quad (8)$$

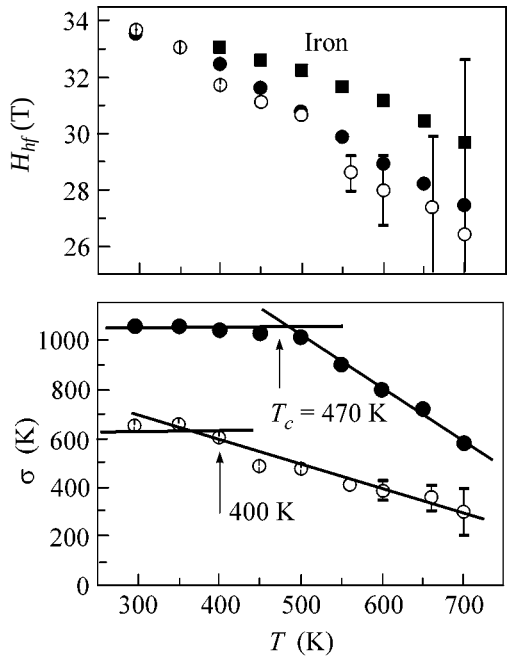

Fig. 3. Temperature dependences of the hyperfine fields (top) and energy distribution widths σ (bottom) obtained from the fitting outermost velocity ranges of the spectra shown in Fig. 1: sample A with 25% NG (closed circles) and sample B with 10% NG (open circles). Rectangles (top) correspond to the bulk values of hyperfine field in pure iron. The indicated Curie temperatures of the amorphous matrix in the samples were estimated by the Mössbauer thermal scan method [8].

and Eq. (5) for the absorption cross section in the GTLR model is reduced to the form independent of the parameter p [1]:

$$\bar{\varphi}(\omega) = \frac{\sigma_a \Gamma_0^2}{4} \sum_{\alpha} |C_\alpha|^2 \times \int_{-\infty}^{\infty} \frac{1}{[\omega - \omega_\alpha \tanh(x)]^2 + \Gamma_0^2/4} P(x, \sigma/k_B T) d(x). \quad (9)$$

As seen from this equation, the spectrum in the fast-relaxation regime represents a continuous distribution of hyperfine magnetic sextets with lines of natural width and relative intensities defined by the $P(x, \sigma/k_B T)$ probability function. Then, one can easily see that the line shapes in the GTLR model are asymmetric and fully determined by the ratio of energy distribution width σ to temperature. Realization of the fast-relaxation regime in our case may only mean that nanograins in the samples studied are small and would demonstrate the superparamagnetic behavior even at room temperature if they were isolated; however, the interparticle interaction makes them stay in the locally ferromagnetic state up to substantially higher temperatures.

In conclusion, the generalized two-level relaxation model proved to be rather efficient in describing spe-

cific shapes of Mössbauer spectra of nanostructure ferromagnetic alloys. It actually represents a new approach to analysis of the spectra taking into consideration the interparticle interaction in a simple form, which can be easily used by experimentalists. However, the GTLR model must be extended to the case of time-dependent energy shifts ΔE, which should be correlated over mutually interacting superparamagnetic particles. In addition, a detailed quantitative analysis of Mössbauer spectra of nanostructured ferromagnetic alloys obviously requires the development of an efficient computational procedure taking into account both the relaxation of interacting particles and their distribution over sizes.

We are grateful to the "Internationales Büro des BMBF," Bonn, and the Russian Ministry of Science and Technology, Moscow (project RUS-157-97), as well as to the Russian Foundation Sponsoring Domestic Science, Moscow, for supporting our collaboration.

REFERENCES

1. A. M. Afanas'ev and M. A. Chuev, Pis'ma Zh. Éksp. Teor. Fiz. **74**, 112 (2001) [JETP Lett. **74**, 107 (2001)].
2. M. Miglierini and J.-M. Greneche, J. Phys.: Condens. Matter **9**, 2303 (1997); M. Miglierini, I. Skorvanek, and J.-M. Greneche, J. Phys.: Condens. Matter **10**, 3159 (1998); M. Miglierini, P. Schaaf, I. Skorvanek, *et al.*, J. Phys.: Condens. Matter **13**, 10359 (2001).
3. K. Suzuki and J. M. Cadogan, Phys. Rev. B **58**, 2730 (1998).
4. T. Kemeny, D. Kaptas, J. Balogh, *et al.*, J. Phys.: Condens. Matter **11**, 2841 (1999); J. Balogh, L. Bujdoso, D. Kaptas, *et al.*, Phys. Rev. B **61**, 4109 (2000).
5. A. Hernando, J. Phys.: Condens. Matter **11**, 9455 (1999).
6. O. Hupe, H. Bremers, J. Hesse, *et al.*, Nanostruct. Mater. **12**, 581 (1999); O. Hupe, M. A. Chuev, H. Bremers, *et al.*, J. Phys.: Condens. Matter **11**, 10545 (1999); M. A. Chuev, O. Hupe, H. Bremers, *et al.*, Hyperfine Interact. **126**, 407 (2000).
7. J. Hesse and H. Rübartsch, J. Phys. E **7**, 526 (1974).
8. O. Hupe, *Untersuchung der magnetischen Wechselwirkungen in nanostrukturierten Systemen: Mössbauer-Effekt und Magnetisierungsmessungen an FeCuNbB-Legierungen*, Thesis (Technische Universität Braunschweig, 2002).
9. H. H. Wickman, in *Mössbauer Effect Methodology*, Ed. by I. J. Gruverman (Plenum, New York, 1996), Vol. 2.
10. L. Néel, Ann. Geophys. **5**, 99 (1949).
11. A. M. Afanas'ev and M. A. Chuev, Zh. Éksp. Teor. Fiz. **107**, 989 (1995) [JETP **80**, 560 (1995)].
12. S. Mørup, Hyperfine Interact. **60**, 959 (1990); S. Mørup and E. Tronc, Phys. Rev. Lett. **72**, 3278 (1994); F. Bødker, S. Morup, M. Pedersen, *et al.*, J. Magn. Magn. Mater. **177–181**, 925 (1998).
13. J. Dormann, F. D'Orazio, F. Lucari, *et al.*, Phys. Rev. B **53**, 14291 (1996); E. Tronc, A. Ezzir, R. Cherkaoui, *et al.*, J. Magn. Magn. Mater. **221**, 63 (2001).
14. N. M. K. Reid, D. P. E. Dickson, and D. H. Jones, Hyperfine Interact. **56**, 1487 (1990).
15. J. van Lierop and D. H. Ryan, Phys. Rev. B **63**, 064406 (2001).

JETP Letters, Vol. 76, No. 9, 2002, pp. 563–567. From Pis'ma v Zhurnal Éksperimental'noĭ i Teoreticheskoĭ Fiziki, Vol. 76, No. 9, 2002, pp. 660–664.

Multicomponent Dense Electron Gas as a Model of Si MOSFET¶

S. V. Iordanski and A. Kashuba

Landau Institute for Theoretical Physics, Russian Academy of Sciences, Moscow, 119334 Russia

Received October 2, 2002

We solve a 2D model of N-component dense electron gas in the limit $N \longrightarrow \infty$ and in the range of the Coulomb interaction parameter $N^{-3/2} \ll r_s \ll 1$. The quasiparticle interaction on the Fermi circle vanishes as $\hbar^2/Nm$. The ground-state energy and the effective mass are found as series in powers of $r_s^{2/3}$. In the quantum Hall state on the lowest Landau level at integer filling $1 \ll \nu < N$, the charge-activation-energy gap and the exchange constant are $\Delta = \log(r_s N^{3/2})\hbar\omega_H/\nu$ and $J = 0.66\hbar\omega_H/\nu$. © *2002 MAIK "Nauka/Interperiodica".*

PACS numbers: 71.10.Ca; 73.43.Cd; 85.30.Tv

Two-dimensional electron gas (2DEG) in GaAs quantum wells and Si heterostructures [1] is a unique system where density of electrons n can be varied widely. Effects of the electrostatic Coulomb interaction are determined by the dimensionless variable $r_s = e^2m/\sqrt{\pi n}\,\hbar^2$. In an Si MOSFET, interesting phenomena were observed recently at relatively large $r_s^\dagger \sim 10$: a conductivity "fan" similar to the metal–insulator transition [2], and an increase of the effective electron mass and magnetic susceptibility [3, 4]. At large r_s, no exact model exists, and many phenomenological approximations have been developed.

At small r_s, there is an exact model—dense electron gas [5]—but two of its key predictions have not been confirmed in experiment. First, theory predicts a reduction of the effective mass $m^*/m - 1 \sim r_s\log(1/r_s)$ at $r_s \longrightarrow 0$ [6], because the forward scattering is larger then the backward scattering for Coulomb potential. Second, in the integer quantum Hall ferromagnet state on the lowest Landau level, theory [7] predicts the Coulomb charge-activation gap $\Delta \sim e^2\sqrt{eH/\hbar c}$ in strong magnetic field H ($r_s \longrightarrow 0$). Yet, in an Si(100) MOSFET, the Shubnikov–de Haas oscillation experiments [8, 3] find $m^*/m = 1 + 0.08r_s$, at $3 > r_s > 0.9$, and the magnetocapacitance experiment [9] finds much lower charge activation gaps $\Delta \sim \hbar eH/mc$, at $4 > r_s > 1.5$. In phenomenological models (see Refs. in [1]), experimental $m^*(r_s) > m$ was reproduced in the large-r_s domain with a crossover at $r_s^* \sim 1$ from the theory [5] with $m^* < m$ to the large r_s with $m^* > m$. But perturbation series in one parameter r_s could hardly have the two so widely different crossovers $r_s^\dagger$ and r_s^*.

In this letter, we show that a systematic model of multicomponent dense electron gas agrees better with experiment. In Si, electron states have a valley degeneracy [1] corresponding to different band minima. For the (100) orientation of the 2D plane, there are $N = 4$ equivalent spin-valley states. Two valley band states here differ only by plane waves $\exp(\pm iQz)$ in the perpendicular direction with an atomic value of momentum Q. These states are strongly orthogonal. For (111) orientation, the spin-valley degeneracy is especially large, $N = 12$. Electron gas in the limit $N \longrightarrow \infty$ was first considered in [10], and the leading term of the ground-state energy was shown to coincide with that of a dense charged boson gas [11].

For N-component dense 2DEG in the limit $N \longrightarrow \infty$, we find a crossover at $r_s^* = 1/N^{3/2}$ from the theory [5] at vanishing r_s to a novel systematic theory at

$$r_s \ll 1 \quad \text{and} \quad r_s \gg r_s^* = 1/N^{3/2}. \tag{1}$$

It describes a system of interacting electrons and plasmons. Plasmons are excitations with large characteristic momentum $q_0 \gg p_F$ and energy $\omega_0 \gg \epsilon_F$. Landau theory of Fermi liquid uses only one function—the amplitude of quasiparticle scattering—to derive all Landau Fermi liquid parameters. In our theory, the interaction between quasiparticles vanishes as $1/Nm$, and the electron subsystem is the ideal Fermi gas. The exchange of high-energy plasmons gives rise to a polaronic-like renormalization of the effective electron mass as a series in powers of $r_s^{2/3}$. In the case of an integer quantum Hall state on the lowest Landau level, we predict a linear dependence on magnetic field of the charge-activation-energy gap and the exchange constant that agree better with experiment.

¶This article was submitted by the authors in English.

0021-3640/02/7609-0563$22.00

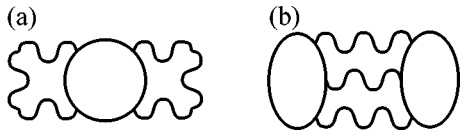

Fig. 1. (a) Four-leg plasmon vertex and (b) two three-leg plasmon vertices contribution to the energy. Solid lines are electron propagations and wavy lines are plasmon propagations.

The 2DEG Hamiltonian is expressed in terms of the second quantized electron operator [12]

$$\hat{H} = \frac{1}{2m}\int \psi^{\dagger}_{\alpha}(\mathbf{r})\left(-i\hbar\nabla + \frac{e}{c}\mathbf{A}(\mathbf{r})\right)^2 \psi_{\alpha}(\mathbf{r})d^2\mathbf{r} + \frac{1}{2}\iint \frac{e^2}{|\mathbf{x}-\mathbf{r}|}\psi^{\dagger}_{\alpha}(\mathbf{x})\psi^{\dagger}_{\beta}(\mathbf{r})\psi_{\beta}(\mathbf{r})\psi_{\alpha}(\mathbf{x})d^2\mathbf{x}d^2\mathbf{r}, \quad (2)$$

where $\alpha, \beta = 1, \ldots, N$ are spin-valley indices. N is an even length of fermion spinor. No valley mixing in the density operators, an isotropic mass tensor, and a positive uniform charge at large distance d from the 2D plane are assumed. At first we assume zero magnetic field and $\alpha_F = e^2/\hbar v_F \approx r_s\sqrt{N} \ll 1$ instead of the first condition (1), and then we extend the theory to all $r_s \ll 1$. We use Matsubara diagrammatic expansion in terms of the Coulomb interaction. The new Coulomb line multiplies the diagram by a small parameter α_F, whereas each electron loop brings a large factor N with it. Therefore, the leading order is given by diagrams with minimum number of Coulomb lines per electron loop, with an essential block being the RPA screened Coulomb interaction—a sequence of alternating Coulomb lines and electron loops [13]. The second condition (1) makes the typical RPA momentum large: $q \sim q_0 \gg p_F$, where $q_0 = (8\pi e^2 mn)^{1/3} = r_s^{1/3}\sqrt{N}\,p_F$ and $\omega_0 = q_0^2/\sqrt{2}\,m$ defines a typical plasmon momentum and energy. The electron polarization operator is

$$\Pi(\omega, \mathbf{q}) = \frac{2n\epsilon(\mathbf{q})}{\omega^2 + \epsilon^2(\mathbf{q})}, \quad (3)$$

where $\epsilon(\mathbf{q}) = q^2/2m$ is the electron dispersion. It depends on the total density n and is independent of an electron distribution over N spin valleys as long as $p_{F_\alpha} \ll q_0$. The RPA Coulomb interaction is

$$D(\omega, \mathbf{q}) = \frac{2\pi e^2}{q}\left(1 + \frac{2\pi e^2}{q}\Pi(\omega, \mathbf{q})\right)^{-1}. \quad (4)$$

Its pole corresponds to a plasmon excitation with a dispersion: $\omega(\mathbf{q}) = \sqrt{q^4 + q_0^3 q}\,/2m$. Electrons can be integrated out from the model (2), leaving an effective theory of plasmons with typical momentum q_0 and a propagator (4) which weakly interact (in the limit $r_s \ll 1$) due to three plasmon, four plasmon, etc., vertices. A plasmon vertex with a k leg with external momenta $q_i^2 \sim q$ and frequencies $|\omega_i| \sim \omega$ vanishes in the limit $q_i^2/m \ll |\omega_i|$ as $nq^2/m\omega^k$ for k even and $nq^4/m^2\omega^{k+1}$ for k odd due to the electron-number conservation.

The kinetic energy density $E_{\rm kin} = \pi n^2/Nm$ is small, because electrons are evenly distributed over N spin-valley states. In the leading order, the energy of 2DEG is given by the zero energy of plasmons: $E_0 = E_{HF} + E'$, where $E_{HF} = -8r_s n^2/3m\sqrt{N}$ is the 2D Hartree–Fock exchange energy and E' is the RPA energy [13]

$$E' = \int\left[\log\left(1 + \frac{2\pi e^2}{q}\Pi(\omega, \mathbf{q})\right) - \frac{2\pi e^2}{q}\Pi(\omega, \mathbf{q})\right]\frac{d\omega d^2\mathbf{q}}{2(2\pi)^3}. \quad (5)$$

At $q \sim p_F$, we single out from E' the term that cancels E_{HF} exactly, and the remaining plasmon energy (also called a correlation energy) can be evaluated as [14]

$$E_0 = -\frac{3\sqrt{\pi}}{4}\Gamma\left(\frac{2}{3}\right)\Gamma\left(\frac{5}{6}\right)r_s^{4/3}\frac{n^2}{m}. \quad (6)$$

Plasmon energy (6) coincides in the leading order with the ground-state energy of a dense charged boson gas [11].

The next corrections to the plasmon energy are given by the second-order diagram (a) and the third-order diagram (b) in Fig. 1. Provided the internal frequency and momentum are related by plasmon dispersion, the value of a diagram is proportional to $r_s^{2/3}$ in power of $N_i - N_L + 2$, where N_i is the number of Coulomb lines and N_L is the number of electron loops. We have numerically evaluated the two diagrams in Fig. 1 and found $E_0 + E_1 = -(2.03191\,r_s^{4/3} - 0.156(1)r_s^2)n^2/m$, where the first term represents Eq. (6). Comparing vertices of the fermion (2) and the dense charged bose gas models, we conclude that these models are different.

A specific feature of our mean field theory that distinguishes it from the standard Landau–Fermi liquid theory is that electron and plasmon excitations are found in a wide momentum range $p_F \ll p \ll q_0$. Let us prove that the four-fermion vertex [12] vanishes on the infrared side of this range: $\Gamma_{\alpha\alpha;\,\beta\beta}(\epsilon_i, p_i) \sim Q^2/mn$ at $p_i/q_0 \longrightarrow 0$, where $\epsilon_i \sim p_i^2/2m$ and $i = 1 \ldots 4$. $\Omega = \epsilon_1 - \epsilon_2$ and $\mathbf{Q} = \mathbf{p}_1 - \mathbf{p}_2$ are the transfered frequency and momentum in the particle-hole channel in Fig. 2. A pair of electron and hole Green's functions with independent integration over frequency and momentum and sum over spin-valley index γ gives a large term [12]. Therefore, vertex $\Gamma(\Omega, Q)$ is a ladder of alternating pairs—polarization operators $\Pi(\Omega, Q)$—and blocks M, defined as the set of all diagrams that cannot be cut over the pair lines. The block M is assumed to be indepen-

dent of the internal integration momenta and frequency of the adjacent $\Pi(\Omega, Q)$. The block M can be further divided into i) a part that can be cut over one plasmon line $\Gamma_3 D(\Omega, Q)\Gamma_3$, where Γ_3 is a three-leg one-plasmon irreducible part at vanishing leg momenta and (ii) a four-leg one-plasmon irreducible part Γ_4 at vanishing leg momenta. Let $\Gamma_D(\Omega, Q)$ and $\Gamma_\Gamma(\Omega, Q)$ be the parts of the total vertex $\Gamma(\Omega, Q)$ that end on the left with a plasmon line D or with a block Γ_4. The Dyson equation for the particle-hole channel is algebraic:

$$\begin{pmatrix} \Gamma_D \\ \Gamma_\Gamma \end{pmatrix} = \begin{pmatrix} D\Gamma_3 \\ \Gamma_4 \end{pmatrix} - \begin{pmatrix} \Pi D(\Gamma_3^2 - 1) & D\Gamma_3\Pi \\ \Gamma_4\Pi\Gamma_3 & \Gamma_4\Pi \end{pmatrix} \begin{pmatrix} \Gamma_D \\ \Gamma_\Gamma \end{pmatrix}. \quad (7)$$

The total four-fermion vertex is given as $\Gamma = \Gamma_3\Gamma_D + \Gamma_\Gamma$:

$$\Gamma = \frac{D\Gamma_3^2 + \Gamma_4(1 - D\Pi)}{\Gamma_3^2 + (1 + \Gamma_4\Pi)(1 - D\Pi)}. \quad (8)$$

If $\Omega \sim Q^2/m$, then we estimate the plasmon propagator $D(\Omega, Q) \approx \Pi^{-1}(\Omega, Q) \sim Q^2$ to be small, but the factor $(1 - D\Pi) \sim Q^3$ is even smaller in the limit $Q \longrightarrow 0$. We use the Ward identity $\Gamma_3 = Z^{-1}$, where $Z < 1$ is the Green's function pole renormalization. Γ_4 is given in the lowest order by the two diagrams in Fig. 3: $\Gamma_4^0 = -\sqrt{\pi}\,\Gamma(2/3)\Gamma(5/6) r_s^{4/3}/\sqrt{3}m$. It represents a retarded attractive interaction, because it appears in the second order of perturbation in plasmon exchange. Assuming that Γ_4 is finite, we conclude from (8) that $\Gamma(0, Q) = D(0, Q) = Q^2/4m^*nZ^2$.

This suggests an analogy between Fermi gas and a ferromagnet with spontaneously broken symmetry where both spin-wave dispersion and interaction vanish as Q^2 according to the Goldstone theorem. A continuation to momenta on the Fermi circle gives the quasiparticle interaction $\Gamma = 2\pi/mN$.

There are no infrared divergences in the block Γ_4, despite the possibility that some internal frequency integration is determined by electron energy poles rather then by plasmon energy poles in the momentum range $p_F \ll p \ll q_0$. Those diagrams that (i) can be cut into two or more parts only over electron lines and for which (ii) each part emerging as a result is one-plasmon irreducible after all internal electron lines are contracted into points would be divergent. Those parts where all plasmon lines are closed into loops are fermion vertices, symbolically written as $V_{2k}\int \psi^{\dagger k}\psi^k dx^2 dt$. In the Cooper channel, the four-leg vertex $V_4 = \Gamma \sim Q^2$ vanishes and thus cuts off a specific 2D logarithmic divergence [12]. All higher order vertices are regular as functions of leg momenta and are irrelevant in 2D, as a simple power counting shows: $t \sim x^2$ and $\psi \sim 1/x$.

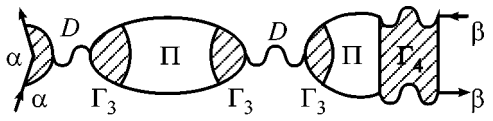

Fig. 2. A particle-hole ladder for vertex Γ. Two-leg element D, three-leg element Γ_3, and four-leg element Γ_4 are shown.

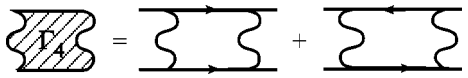

Fig. 3. Four-leg vertex is a sum of two diagrams in the leading order.

Despite the vanishing interaction between electrons, there is an essential plasmon polaronic effect. The electron self-energy [12]

$$\Sigma(\epsilon, \mathbf{p}) = -\int D(\omega, \mathbf{q}) G(\epsilon + \omega, \mathbf{p} + \mathbf{q}) \frac{d\omega d^2\mathbf{q}}{(2\pi)^3} \quad (9)$$

is related to the electron Green's function $G^{-1}(\epsilon, \mathbf{p}) = i\epsilon - p^2/2m + \mu - \Sigma(\epsilon, \mathbf{p})$, where μ is the chemical potential. At $\epsilon \ll \omega_0$ and $p \ll q_0$, we calculate the self-energy (9) and find $G^{-1}(\epsilon, \mathbf{p}) = Z(i\epsilon - \epsilon(\mathbf{p}))^{-1}$, where the quasiparticle dispersion is $\epsilon(\mathbf{p}) = (p^2 - p_F^2)/2m^*$ with the renormalized effective mass

$$\frac{m}{m^*} = 1 - \frac{1}{10\sqrt{\pi}}\Gamma\left(\frac{1}{3}\right)\Gamma\left(\frac{7}{6}\right) r_s^{2/3}, \quad (10)$$

and $Z^{-1} = 1 + \Gamma(1/3)\Gamma(7/6) r_s^{2/3}/2\sqrt{\pi}$ is a renormalization of the Green's function pole.

A static screened potential of an external charge z immersed into 2DEG is given by $D(0, \mathbf{q})$ (4): $V(\mathbf{q}) = 2\pi e^2 z q^2/(q^3 + q_0^3)$. It grows with the transferred momentum, which helps to explain the heavier effective mass (10), because the backward scattering is larger than the forward scattering.

The temperature dependence of the effective mass comes from the momentum range $p_F \ll p \ll q_0$. Taking into account the temperature dependence of the polarization operator in the equation for the self-energy (9), we encounter logarithmic infrared divergence. Deriving and solving a simple renormalization group equation, we find a growing effective mass if the momentum of the quasiparticle decreases. On the Fermi line, we find

$$\frac{1}{m_*^2(T)} = \frac{1}{m_*^2} - \frac{NT^2}{12n^2}\log\frac{q_0}{p_F}, \quad (11)$$

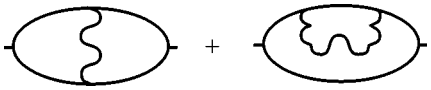

Fig. 4. Two diagrams for a spin-susceptibility correction.

where zero-temperature effective mass m_* is given by (10). In the experimental situation of the Si (100) MOSFET, the effective mass (11) can strongly depend on temperature.

At $T \ll \omega_0$, plasmon thermal fluctuations freeze out, whereas the ideal electron subsystem evolves from a degenerate gas at $T \ll \epsilon_F$ to the Boltzmann gas at $T \gg \epsilon_F$. The 2DEG thermodynamic potential $\Omega(T) = N\Omega_0(T, \mu) + E_0 + E_1$, where $\Omega_0(T, \mu)$ is the thermodynamic potential of the ideal Fermi gas with the property $N\Omega_0(0, \epsilon_F) = E_{\rm kin}$.

Static magnetic susceptibility is related to a change of the total energy in external magnetic field $\delta E = -N\chi^*(\mu_B H)^2/2$. χ^* is given by the Pauli ideal-gas susceptibility $\chi = m/2\pi$ and by the two diagrams in Fig. 4. Evaluating them, we find $\chi^*/\chi = m^*/m$. There is no exchange part coming from the interaction between quasiparticles. Thus, there is a single Landau–Fermi-liquid parameter m^*/m given by a series in powers of $r_s^{2/3}$. We observe that the experimental effective mass [3, 8] agrees well with (10). The experimental susceptibility [3, 15] is larger than χ^*, which indicates some exchange effects for $N = 4$.

In the end, we consider the quantum Hall state [16], with an integer filling factor ν defined as the ratio of electron number to the magnetic flux number. If $1 \ll \nu < N$, then ν is the number of occupied spin-valley states in the lowest Landau level. This state is degenerate under global rotations in electron Fock space by unitary matrices from the Grassmanian coset $F = U(N)/U(\nu) \otimes U(N - \nu)$, which corresponds to a ferromagnetic order parameter at zero temperature. We use the so-called magnetic units $\hbar = 1$, $e = c$, magnetic length $l_H = 1$, cyclotron frequency $\omega_H = eH/mc = 1/m$, and $r_s = \sqrt{2}\, e^2/\omega_H l_H \sqrt{\nu}$. The polarization operator is

$$\Pi(\omega, \mathbf{q}) = \frac{\nu}{2\pi}\sum_{s=1}^{\infty}\frac{q^{2s}}{2^s s!}\frac{2s\omega_H}{\omega^2 + \omega_H^2 s^2}\exp\left(-\frac{q^2}{2}\right), \quad (12)$$

and at $ql_H \gg 1$ it transforms into (3). We find the self-energy (9) using the Green's function $G^{-1}(\epsilon) = i\epsilon + \mu$ in the lowest Landau level. The difference between the self-energies for an electron in the empty spin-valley state and an electron in the occupied spin-valley state gives the charge activation gap: $\Delta = \Sigma_e - \Sigma_o$. We single out the Hartree–Fock term $E_{HF} = \sqrt{\pi/2}\, e^2/l_H$ and find

$$\Delta = E_{HF} - \int\frac{d\omega d^2\mathbf{q}}{(2\pi)^3}\left(\frac{2\pi e^2}{q} - D(\omega, q)\right)\frac{2\mu}{\omega^2 + \mu^2}, \quad (13)$$

where only the real part of the electron Green's function is essential, $\mu = \Delta/2$ is the chemical potential inside the ferromagnetic gap, and the last fraction in (13) becomes approximately the delta function $\delta(\omega)$ if $\mu \ll \omega_H$. The Hartree–Fock term cancels out exactly as in zero magnetic field, and after frequency integration we find

$$\Delta = \frac{\omega_H}{2}\int_0^{\infty} D(q)dq = \frac{\hbar\omega_H}{\nu}(\log(r_s\nu^{3/2}) + 0.277), \quad (14)$$

where $D^{-1}(q) = e^{q^2/2}/r_s\sqrt{2\nu} + \nu\sum_{s=1}^{\infty} q^{2s-1}/2^s s!s$. Note that $\Delta \ll E_{HF}$. The gap in the lowest Landau level (14) is similar to the gap in the $N = 2$ quasiclassical case of weak magnetic field and odd integer $\nu \gg 1$ [17].

We find a dispersion of spin waves as a pole of correlation function $C(\mathbf{x} - \mathbf{r}) = \langle\psi_e^\dagger(\mathbf{x})\psi_o(\mathbf{x})\psi_o^\dagger(\mathbf{r})\psi_e(\mathbf{r})\rangle$, which is uniform, because it describes a neutral excitation. It is given by a ladder set of diagrams like the second one in Fig. 3, where the electron Green's function includes the self-energy $G_{eo}^{-1} = i\epsilon \pm \Delta/2$. Using the Landau gauge representation of the density operators [7], we find

$$C(\Omega, Q) = \sum_{k=0}^{\infty}\left(-\frac{\omega_H}{i\Omega - \Delta}\int D(q)\exp(i\mathbf{Q}\times\mathbf{q})\frac{d^2\mathbf{q}}{4\pi q}\right)^k, \quad (15)$$

a sum over k-leg ladder diagrams. It has a pole at $i\Omega = \epsilon(Q)$ with the spin-wave dispersion

$$\epsilon(\mathbf{Q}) = \frac{\omega_H}{2}\int_0^{\infty} D(q)(1 - J_0(qQ))dq. \quad (16)$$

At intermediate wavelengths $r_s^{-1}\nu^{-3/2} \ll Ql_H \ll 1$, spin-wave dispersion is logarithmic: $\epsilon(Q) = -\omega_H\log(Ql_H)/\nu$, whereas, in the long-wavelength limit at $Ql_H \ll r_s^{-1}\nu^{-3/2}$, we recover Goldstone dispersion: $\epsilon(Q) = JQ^2$, where the exchange constant can be evaluated numerically:

$$J = \frac{\omega_H}{8}\int_0^{\infty} q^2 D(q)dq = 0.6613\frac{\omega_H}{\nu}. \quad (17)$$

A pair of Skyrmion topological defects of ferromagnetic order [18] has a lower activation energy $\Delta = J$ than the electron–hole pair (14).

We are grateful to G.M. Eliashberg, who shaped very much the content of the work. This work was supported by the Russian Foundation for Basic Research

(project no. 01-02-17520a) and INTAS (grant no. 99-01146).

REFERENCES

1. T. Ando, A. B. Fowler, and F. Stern, Rev. Mod. Phys. **54**, 437 (1982).
2. E. Abrahams, S. V. Kravchenko, and M. P. Sarachik, Rev. Mod. Phys. **73**, 251 (2001).
3. V. M. Pudalov, M. E. Gershenson, H. Kojima, *et al.*, Phys. Rev. Lett. **88**, 196404 (2002).
4. A. A. Shashkin, S. W. Kravchenko, V. T. Dolgopolov, and T. M. Klapwijk, Phys. Rev. B **66**, 073303 (2002).
5. M. Gell-Mann and K. A. Brueckner, Phys. Rev. **106**, 364 (1957); K. Sawada, Phys. Rev. **106**, 372 (1957).
6. M. Gell-Mann, Phys. Rev. **106**, 369 (1957).
7. Yu. A. Bychkov, S. V. Iordanskiĭ, and G. M. Éliashberg, Pis'ma Zh. Éksp. Teor. Fiz. **33**, 152 (1981) [JETP Lett. **33**, 143 (1981)]; C. Kallin and B. I. Halperin, Phys. Rev. B **30**, 5655 (1984).
8. J. L. Smith and P. J. Stiles, Phys. Rev. Lett. **29**, 102 (1972).
9. V. S. Khrapai, A. A. Shashkin, and V. T. Dolgopolov, cond-mat/0202505.
10. Y. Takada, Phys. Rev. B **43**, 5962 (1991).
11. L. L. Foldy, Phys. Rev. **124**, 649 (1961).
12. A. A. Abrikosov, L. P. Gorkov, and I. E. Dzyaloshinski, *Methods of Quantum Field Theory in Statistical Physics* (Dover, New York, 1975).
13. D. Pines and P. Nozieres, *Theory of Quantum Liquids* (Benjamin, New York, 1966; Mir, Moscow, 1967).
14. Capacitor energy density e^2dn^2 insures positive pressure and compressibility in the limit $d\sqrt{n} \longrightarrow \infty$.
15. T. Okamoto, K. Hosoya, S. Kawaji, and A. Yagi, Phys. Rev. Lett. **82**, 3875 (1999).
16. *The Quantum Hall Effect*, Ed. by E. R. Prange and S. M. Girvin (Springer-Verlag, New York, 1990; Mir, Moscow, 1989).
17. I. L. Aleiner and L. I. Glazman, Phys. Rev. B **52**, 11296 (1995).
18. S. L. Sondhi, A. Karlhede, S. A. Kivelson, and E. H. Rezayi, Phys. Rev. B **47**, 16419 (1993).

JETP Letters, Vol. 76, No. 9, 2002, pp. 568–571. From Pis'ma v Zhurnal Éksperimental'noĭ i Teoreticheskoĭ Fiziki, Vol. 76, No. 9, 2002, pp. 665–668.

Steps on Current–Voltage Characteristics of a Silicon Quantum Dot Covered by Natural Oxide¶

S. V. Vyshenski, U. Zeitler*, and R. J. Haug*

Nuclear Physics Institute, Moscow State University, Moscow, 119992 Russia

e-mail: svysh@pn.sinp.msu.ru

** Institut für Festkörperphysik, Uhiversität Hannover, D-30167 Hannover, Germany*

Received October 3, 2002

Considering a double-barrier structure formed by a silicon quantum dot covered by natural oxide with two metallic terminals, we derive simple conditions for a steplike voltage–current curve. Due to standard chemical properties, doping phosphorus atoms located in a certain domain of the dot form geometrically parallel current channels. The height of the current step typically equals (1.2 pA)N, where $N = 0, 1, 2, 3\ldots$ is the number of doping atoms inside the domain, and only negligibly depends on the actual position of the dopants. The found conditions are feasible in experimentally available structures. © *2002 MAIK "Nauka/Interperiodica".*

PACS numbers: 73.63.Kv; 73.21.La; 73.23.-b

The fabrication of Si nanostructures became possible through recently developed new technologies [1, 2]. Individual silicon quantum dots (SQD) reported in [2] are spherical Si particles with diameters d in the range 5–12 nm covered by a 1–2-nm-thick natural SiO_2 film. Metallic current terminals made from degenerately doped Si are defined lithographically to touch each individual dot from above and from below.

To ensure metallic electrodes, the donor concentration n should be $n \geq n_{\text{Mott}}$, where $n_{\text{Mott}} = 7.3 \times 10^{17}$ cm^{-3}. The critical concentration n_{Mott} is defined by the Mott criterion [3], introducing the transition to a metallic type of conductivity in a semiconductor at

$$a_B (n_{\text{Mott}})^{1/3} = 0.27, \qquad (1)$$

where a_B is the Bohr radius of an electron bound to a donor inside the Si crystal; in the case of phosphorus donors, $a_B = 3$nm [4].

As for the doping of the dot, the situation concerning a Mott transition in small dots is much less trivial than the one described by Eq. (1). Let us consider dots with diameters $d = 10$ nm formed from n-doped Si with $n = n_{\text{Mott}}$ as an illustrative example. Then each dot contains on average one donor. Note that we will consider degenerately n^+-doped electrodes with $n \gg n_{\text{Mott}}$, which ensures metallic conduction up to the borders of the dot.

Real fabrication technology [2] provides a wafer with hundreds of SQDs on it with current leads towards each individual SQD. Dots on average have the same value of mean dopant concentration n, which is determined by the parent material of bulk silicon the dots are formed from. However, on the level of each individual SQD, we will always have exactly *integer* number of doping atoms. If, as in the example above, the average number of dopants $\overline{N_{\text{tot}}} = 1$, the actual number of donors in the dot can have values $N_{\text{tot}} = 0, 1, 2, 3,\ldots$, with values larger than these very unlikely.

Our objective is to illustrate that SQDs from the same wafer fall into several distinct sets of approximately the same conductance. The typical value of conductance for each set is nearly completely determined by the number N of donors present in a certain part of a SQD, so that N labels each set of SQDs.

Summarizing the above, we need for a quantization of the conduction through a dot with N donors the following conditions:

• Size d of the dot comparable with Bohr radius: $2 < d/a_B < 5$.

• Average doping n of the dot $n \leq d^{-3}$, leading to a mean number of dopants $\overline{N_{\text{tot}}} \leq 1$, so that $N_{\text{tot}} = 0, 1, 2$ are the most probable configurations of an individual SQD.

• Doping of the electrodes $n_{\text{el}} \gg n_{\text{Mott}}$, so that current leads are perfectly metallic.

• Dot covered by an oxide layer thick enough to suppress ballistic transport through the dot.

In fact, all these conditions can be simultaneously satisfied for a SQD fabricated with the method mentioned above [2].

Model system. We use a simple model of a cubic SQD with $d > 2a_B$ (we will use $d = 10$ nm for estimates), covered with an oxide layer with thickness $\delta = 2$ nm, height [4] $B = 3.15$ eV, and connected with current ter-

¶This article was submitted by the authors in English.

minals from the left and right. The x axis is oriented from left to right along the current flow, as shown in Fig. 1.

A tunneling current is injected into the dot via the oxide barrier from the top (source at $x = 0$) and leaves the dot at the bottom (drain at $x = d$). Due to the presence of the oxide barriers, this current is nonballistic and nonthermal. We assume that the high potential barriers associated with the oxide layers are not much affected by the voltage and the tunneling charges. We concentrate on what happens between these effective source and drain (Fig. 2), as in [5].

In the case where the dot can be regarded as an insulating system, it is reasonable to assume that the applied voltage drops equally over the potential barriers and the dots. For simplicity, we neglect the difference of the dielectric constants of the oxide barriers and the dot. In this approximation, we can introduce an effective voltage $V_{\text{eff}} = V(d - 2\delta)/d = 0.6\,V$ describing the part of the total transport voltage V applied between effective source and drain which drops across the dot itself.

In this crude approximation, we neglect the effect of spatial quantization upon values of the ionization energy, the conductivity gap, and material parameters of silicon.

Dot without donors. At $V_{\text{eff}} = 0$, the Fermi level inside the dot is situated in the middle of the gap, i.e., $E_g/2$ below the conduction band edge ($E_g = 1.14$ eV at 300 K).

As V_{eff} grows, the bottom of the (still empty) conduction band bends down accordingly. When the conduction band in the dot close to the drain aligns with the Fermi level of the emitter, we expect a drastic increase in the tunneling current. This threshold V_{th} voltage (Fig. 2) for V_{eff} is given by $V_{\text{th}} = E_g/2e$, regardless of the number N_{tot} of dopants in the dot (as long as the dot is not yet metallic, of course). In the following, we therefore limit our studies to voltages

$$|V_{\text{eff}}| \le V_{\text{th}} = E_g/2e = 0.57\ \text{V}. \qquad (2)$$

In this voltage range, we have a d-thick barrier (formed by the dot) with always finite height between effective source and drain. The intrinsic concentration of electrons and holes at 300 K is 1.4×10^{10} cm^{-3}. Even at this high temperature, the probability of having at least one intrinsic electron in a dot with size $d = 10$ nm is only 1.4×10^{-8}. So we would expect virtually no current in this mode. This is confirmed by direct electrical tests [2] of SQD with the required properties.

Single-donor channel. Let us now consider one single donor in the dot located at x with ionization energy [4] $E_d = 0.045$ eV (for P as a donor).

At zero temperature, current is due to resonant tunneling via nonionized donor (as in [6], for example).

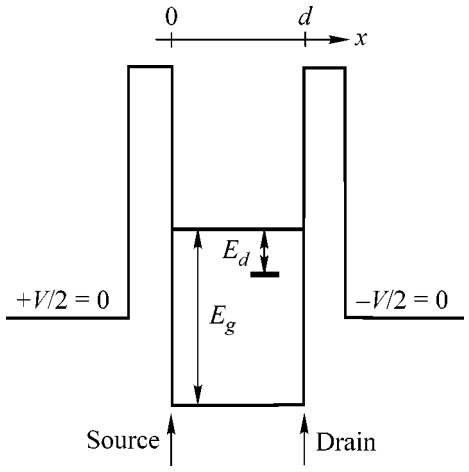

Fig. 1. Potential profile of the dot covered by an oxide layer at $V = 0$. A donor is marked with a short bar.

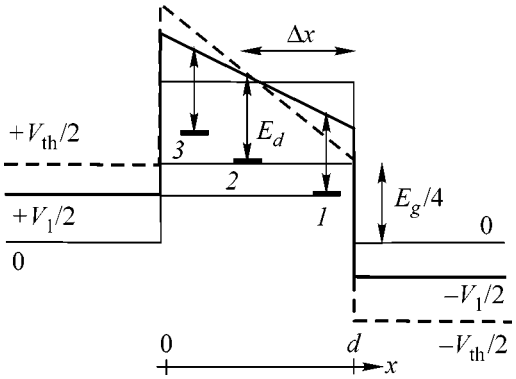

Fig. 2. Potential profile of the dot between effective source and drain biased with $V_{\text{eff}} = V_1$ (thick solid line) and $V_{\text{eff}} = V_{\text{th}}$ (dashed line).

Differential conductance $g(\varepsilon)$ for the states with energy ε is

$$g(\varepsilon) = \frac{4e^2}{\pi\hbar}\frac{\Gamma_l\Gamma_r}{(\varepsilon - \varepsilon_d)^2 + (\Gamma_l + \Gamma_r)^2}, \qquad (3)$$

where $\Gamma_{l,r}$ is the linewidth of the 1s state of the electron bound to the donor due to coherent mixing with conduction states to the left (right) of the left (right) tunnel barrier.

Oxide barriers (with height $B = 3.15$ eV and width $\delta = 2$ nm) give the dominant contribution to $\Gamma_{l,r}$ compared to contributions of the body of the dot (with typical height $< E_g/2 = 0.57$ eV and width $< d = 10$ nm). So, we can approximate $\Gamma_{l,r}$ with linewidth Γ for the case

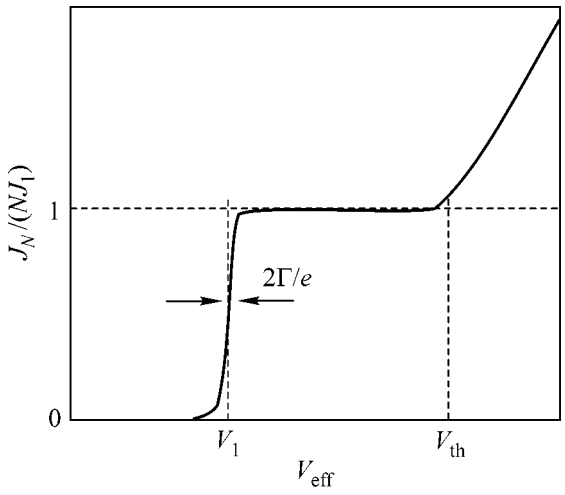

Fig. 3. Current–voltage characteristic of a model system (not to scale).

of an impurity localized at distance δ inside rectangular one-dimensional tunnel barrier [6] of height B:

$$\Gamma_l = \Gamma_r = \Gamma = \frac{2p_F\kappa}{p_F^2+\kappa^2}B\frac{\exp(-2\kappa\delta)}{\kappa\delta} = 2.5\times10^{-9}\ \text{eV}, \quad (4)$$

where m is (true, not effective) electron mass, $\kappa = (2mB)^{1/2}/\hbar$, and $p_F = (2mE_F)^{1/2}/\hbar = (3\pi^2 n_{\rm el})^{1/3}$ is the Fermi wave number in the contact electrodes. The numerical estimate in (4) is given for the electrodes doped up to $n_{\rm el} = 10^{21}$ cm^{-3} as in [2].

Within approximation (4), the point $\varepsilon = \varepsilon_d$ brings function $g(\varepsilon)$ given by (3) to a sharp maximum $g(\varepsilon_d) = e^2/\pi\hbar$ of width $\Gamma \ll eV_{\rm th}$.

From Fig. 2, it is clear that resonant energy $\varepsilon_d = E_g/2 - xV_{\rm eff}/2ed - E_d$. This means that, as soon as the effective Fermi level $eV_{\rm eff}/2$ reaches a certain threshold $eV_1/2$, tunnel current J flowing through the structure acquires a steplike increase of

$$J_1 = \frac{1}{e}\int_{-eV/2}^{eV/2} g(\varepsilon)d\varepsilon = \frac{g(\varepsilon_d)2\pi\Gamma}{e} = \frac{2e\Gamma}{\hbar} = 1.2\ \text{pA}. \quad (5)$$

If the impurity is located near the drain, i.e., $d - a_B < x < d$ (as donor *1* in Fig. 2), then threshold V_1 for the effective voltage $V_{\rm eff}$ is given by

$$V_1 = E_g/2e - E_d/e = 0.525\ \text{V}. \quad (6)$$

In contrast, for an impurity located at distances $\Delta x > 2dE_d/E_g$ from the drain (i.e., further away than the threshold case of donor *2* in Fig. 2), no additional current channel via a single impurity can be opened at low enough voltages defined in (2) where virtually no background current is present. In the present case, this value $\Delta x = 0.8$ nm, which returns us to the above criterion: only impurities located in the immediate vicinity (defined within the accuracy a_B) of the drain contribute to the single-impurity channel.

This shows that, in the first approximation, the conductance of this channel does not depend on x. As shown above, a single-impurity channel already selects only impurities located within a very narrow range of x close to the drain.

Two-, three-, multi-donor channel. The above consideration shows that, due to the bend of the bottom of conduction band following the transport voltage, there is no chance to notice current flowing through a sequential chain of impurities (such as donors *1* and *3* in Fig. 2), connecting source and drain. The contribution of such a chain will be totally masked by the current flowing directly via the conduction band. The only way for multiple impurities to manifest themselves in quantized conductance is to form multiple *geometrically parallel* single-impurity channels situated close enough to the drain, as considered above.

Therefore, if $N > 1$ impurities fall into the thin layer near the drain to approximately the same x coordinate as that of donor *1* in Fig. 2 (within the Bohr radius), we will see a switching-on of an N-fold channel with current

$$J_N = NJ_1 = N2e\Gamma/\hbar = (1.2\ \text{pA})N \quad (7)$$

at the same threshold voltage $V_{\rm eff} = V_1 = 0.525$ V as for a single-donor channel (Fig. 3).

All the above considerations are only valid as long as the dot itself can be regarded as an insulating system. As the number of donors in an SQD grows, the dot becomes a metallic particle, and the conduction band edge in the dot aligns with the Fermi level of the electrodes. In a very simple estimate, we define this transition to a metal when the total volume of $N_{\rm tot}$ donors with an individual volume of $(4\pi/3)a_B^3$ exceeds the volume of the dot. This is an exaggerated version of the Mott criterion (1) that holds not only in bulk but also in a small structure. For the analyzed example from above this gives $N_{\rm tot} = 8$ as a limiting value. The practically interesting set 0, 1, 2, 3, … for both $N_{\rm tot}$ and N considered above is still far below this limit.

Quite a number of other mechanisms of electron transport might take place in this system. Surprisingly, even taking into account such other mechanisms [7] does not much change the main idea of the present paper.

In small dots with diameter $d < 2a_B = 6$ nm, the domain with N active dopants extends to the whole dot, and thus $N = N_{\rm tot}$. In large dots with diameter $d > 2a_B = 6$ nm, the domain with active dopants is less than the dot itself and is localized near the drain. Hence, the position of the domain, number N, and value J_N all can

be different for current flowing in different directions. Really, when the sign of applied voltage changes, the source and the drain change places.

In a certain sense, the discrete increase of a dot's conductivity that follows the increase of the dopants number could be regarded as a *mesoscopic analogue of the Mott transition* between insulating and conducting states of the system.

Useful discussions with I. Devyatov, M. Kupriyanov, and S. Oda are gratefully acknowledged.

REFERENCES

1. L. J. Guo, E. Leobandung, L. Zhuang, *et al.*, J. Vac. Sci. Technol. B **15**, 2840 (1997).
2. A. Dutta, M. Kimura, Y. Honda, *et al.*, Jpn. J. Appl. Phys. **35**, 4038 (1997); S. Oda and K. Nishiguchi, J. Phys. IV **11** (3), 1065 (2001).
3. N. F. Mott, *Metall-Insulator Transitions* (Taylor & Francis, London, 1990, 2nd ed.), Chap. 5.
4. *Landolt-Börnstein: Numerical Data and Functional Relationships in Science and Technology, New Series*, Group III, Vol. 17a: *Physics of Group IV Elements and III–V Compounds*, Ed. by O. Madelung (Springer-Verlag, Berlin, 1982).
5. J. Schwinger, *Particles, Sources, and Fields* (Addison-Wesley, Reading, 1970; Mir, Moscow, 1976).
6. A. I. Larkin and K. A. Matveev, Zh. Éksp. Teor. Fiz. **93**, 1030 (1987) [Sov. Phys. JETP **66**, 580 (1987)].
7. I. A. Devyatov and M. Yu. Kupriyanov, Zh. Éksp. Teor. Fiz. **104**, 3897 (1993) [JETP **77**, 874 (1993)].

JETP Letters, Vol. 76, No. 9, 2002, pp. 572–574. Translated from Pis'ma v Zhurnal Éksperimental'noĭ i Teoreticheskoĭ Fiziki, Vol. 76, No. 9, 2002, pp. 669–672.

Anomalously High Raman Scattering Cross Section for Carbon–Carbon Vibrations in *trans*-Nanopolyacetylene

D. Yu. Paraschuk[1, *], I. V. Golovnin[1], A. G. Smekhova[1], and V. M. Kobryanskii[2]

[1] *Faculty of Physics, Moscow State University, Vorob'evy gory, Moscow, 199992 Russia*

** e-mail: paras@polys.phys.msu.su*

[2] *Semenov Institute of Chemical Physics, Russian Academy of Sciences, ul. Kosygina 4, Moscow, 117977 Russia*

Received October 3, 2002

Absolute Raman scattering cross section on the stretching carbon–carbon vibrational modes of *trans*-nanopolyacetylene (NPA) was measured at an excitation wavelength of 514 nm. It is shown that the carbon–carbon bonds in *trans*-NPA scatter light more efficiently than in the diamond structure by several orders of magnitude. The role of resonant Raman scattering and the model of coherent vibrations of carbon–carbon bonds are discussed. © *2002 MAIK "Nauka/Interperiodica".*

PACS numbers: 33.20.Fb; 42.70.Jk; 78.30.Jw

Polymers with conjugated π-electron system attract active attention as prototypes of materials with well-defined controllable electronic and optical properties. In recent years, they have been used in the fabrication of highly efficient light-emitting diodes [1] and optoelectronic integrated devices [2]. There have also been reports on the discovery of superconductivity in this material [3]. An important feature of the π-conjugated polymers is the strong electron–vibrational interaction in polymer chain, resulting, in particular, in a high nonlinear optical response of the vibrational nature. Polyacetylene (PA) is chemically the simplest π-conjugated polymer $[(CH)_x]$, in which the polymer chain consists of a sequence of carbon–carbon (CC) bonds (…–C=C–C=…). Most remarkable properties are displayed by the PA *trans* isomer. In spite of an almost 30-year history of inquiry, *trans*-PA has become quite a complex material for studying the unusual properties of long π-conjugated chains, primarily because of the destructive role of various defects that are present in the available PA samples. However, in recent years, one has succeeded in synthesizing the most ordered PA called nano-PA (NPA) [4], where the PA nanoparticles are dispersed in a transparent polymer matrix of a saturated polymer. The properties of *trans*-NPA are qualitatively different from those observed in *trans*-PA of other types. In particular, the anomalously high spontaneous Raman activity of stretching CC vibrational modes observed in [5] cannot be explained within the framework of the conventional Raman scattering theory [6, 7]. In [7], we proposed a qualitative model for interpreting these anomalies as a manifestation of vibrational coherence in the ordered *trans*-PA chains. In this work, we report the experimental estimate of the unusually high absolute Raman scattering cross section for the stretching CC modes in *trans*-NPA, which exceeds, by several orders of magnitude, highly Raman active materials such as diamond.

NPA films consisted of the PA nanoparticles of size ≤30 nm dispersed in a transparent poly(vinyl butyral) matrix with a PA weight content of ≈1% [4]. The PA nanoparticles were globular in shape and formed from structurally organized π-conjugated chains. The absorption spectrum of NPA showed a sharp edge with a zero-phonon line of the *trans* isomer at the wavelength λ = 730 nm (Fig. 1). The *trans*-to-*cis* concentration ratio was >90%, as was estimated from the optical absorption of films (Fig. 1) and the ratio of Raman intensities of the *cis* and *trans* isomers. Measurements were made at room temperature for unoriented films

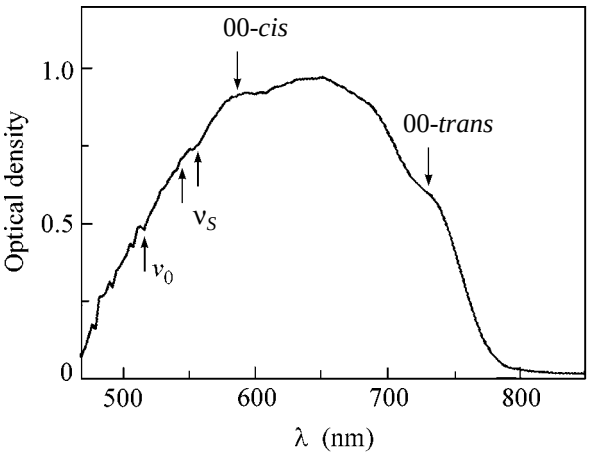

Fig. 1. Absorption spectrum of NPA film. Arrows indicate the excitation wavelength (ν_0), the Stokes scattering components from the C–C and C=C vibrational modes, and the zero-phonon absorption lines of the NPA isomers.

0021-3640/02/7609-0572$22.00 © 2002 MAIK "Nauka/Interperiodica"

with an optical density of ~1 and a thickness of 5 μm on glass substrates.

The intensity of scattered light from a sample with length L, refractive index n, and reflection coefficient R in a small solid angle $\Delta\Omega \ll 1$ is

$$I_S = I_0(1-R)^2 S(\nu_0, \nu_S) L \Delta\Omega n^2 T^*, \quad (1)$$

where I_0 is the intensity of the incident light, $S(\nu_0, \nu_S)$ is the Raman extinction per unit length and unit solid angle in a given scattering geometry for the optical excitation ν_0 and scattering ν_S frequencies, the factor n^2 accounts for the difference in the solid angles of Raman observation in the sample and outside it, and the T^* factor accounts for the sample absorption at ν_0 and ν_S (Fig. 1). For the sample with absorption coefficients $\alpha(\nu_0)$ and $\alpha(\nu_S)$, one has after integrating over L

$$T^* = \exp[-\alpha(\nu_S)L]\frac{\exp[\alpha(\nu_S)L - \alpha(\nu_0)L] - 1}{[\alpha(\nu_S) - \alpha(\nu_0)]L}. \quad (2)$$

For measuring the Raman spectra of NPA, a triple spectrograph was assembled on the basis of a double monochromator (f/6) with dispersion subtraction and a dispersive monochromator equipped with a cooled CCD. The forward scattering geometry was used, for which the argon laser radiation at $\lambda = 514$ nm and a power of ≈10 mW was focused on the sample, and the scattered radiation was accumulated at the input slit of the double monochromator.

The absolute Raman cross section of NPA was obtained using a strong Raman line at 872 cm^{-1} in a $LiNbO_3$ crystal. A plane-parallel $LiNbO_3$ plate of thickness $L = 1$ mm optically polished on both sides and oriented along its optical axis was used. The integrated Raman cross section of $LiNbO_3$ for this orientation was taken from [8], where it was measured relative to diamond at $\lambda = 488$ nm. The Raman extinction $S(\nu_0, \nu_S)$ of diamond at $\lambda = 514$ nm was taken from [9].

The Raman spectra measured under similar conditions for the NPA film and $LiNbO_3$ crystal are shown in Fig. 2. In the Raman spectrum of NPA, two lines at 1080 and 1470 cm^{-1} dominate, which correspond, respectively, to the C–C and C=C stretching modes of the *trans* isomer [5]. The Raman linewidths were mainly determined by the spectrometer instrumental function with a width of ≈40 cm^{-1}. The ratio of areas under the two Raman lines and the $LiNbO_3$ line (Fig. 2) was found to be $I_S(\text{NPA})/I_S(LiNbO_3) = 2 \pm 0.5$. Taking into account the parameters for $LiNbO_3$ ($n = 2.3$, $R = 0.16$, $L = 1$ mm, and $T^* = 1$) and NPA ($n = 1.5$, $R = 0.04$, $L = 5$ μm, and $T^* \approx 0.5$) one has from Eq. (1) $S(\text{NPA})/S(LiNbO_3) \approx 1500$. Setting the ratio $S(LiNbO_3)/S(\text{diamond}) = 0.44$ for the diamond line at 1332 cm^{-1} at $\lambda = 488$ nm [8] and $S(\text{diamond}) = 8 \times 10^{-7}$ cm^{-1} sr^{-1} at $\lambda = 514$ nm [9] and taking into account the corrections to the factor ν_S^4, one finally obtains for the isotropic film $S(\text{NPA}) \approx 5 \times 10^{-4}$ cm^{-1} sr^{-1}. Notice that the Raman signals for NPA depended linearly on the excitation intensity.

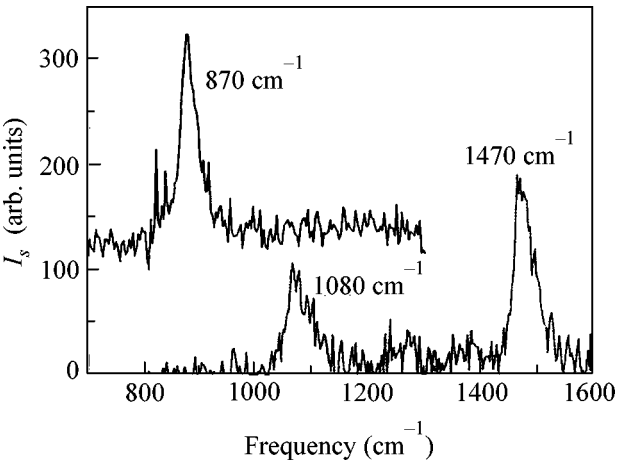

Fig. 2. (bottom line) Raman spectra of the NPA film and (upper line) of the reference $LiNbO_3$ sample. The spectrum of $LiNbO_3$ is shifted for clearness.

Thus, the Raman intensity of an NPA film with ≈1% of PA is three orders of magnitude higher than in diamond, which is known to be among the most Raman active substances. With allowance made for the carbon concentration in NPA and in diamond, one finds that the scattering cross section $\sigma = S/n = 10^{-24}$ cm^2/sr of the CC mode per one carbon atom in *trans*-NPA is 2×10^5 times greater than in diamond. Note that this result relates to the *trans*-NPA cross section averaged over the orientations of the strongly anisotropic polymer chains. Clearly, the anisotropy factor will increase this result. It is natural to attribute the enhancement of Raman intensity to the conjugation effect of carbon p orbitals in polymer chains.

Naturally, a comparison of the Raman efficiencies of different substances is only correct for the optical frequencies far from the electronic absorption bands. Let us discuss the origin of optical absorption in NPA at $\lambda = 514$ nm corresponding to the short-wavelength edge of the main electric-dipole transition of *cis*-NPA (Fig. 1). Note, first, that *cis*-NPA isomerizes into the *trans* form at the excitation intensities used in our Raman experiments. The Raman measurements of the NPA films with the isomer content *cis*/*trans* ≈ 1 followed by the isomerization in the course of recording indicate that the intensity of *cis* lines decreases from a value comparable to the *trans* lines to the undetectable level [10]. However, in this case the absorption at $\lambda = 514$ nm remains appreciable (Fig. 1), likely, because the isomerization results in a rather inhomogeneous NPA *trans* form with a high content of short conjugated bonds, which are responsible for the optical absorption at $\lambda = 514$ nm but make a small contribution to the Raman signal [10]. This follows from the well-known

fact (see, e.g., [11]) that the short conjugated *trans*-isomer chains manifest themselves at the high-frequency absorption and Raman edges (this is also seen from the asymmetry of the spectra in Fig. 2). Consequently, within the measurement accuracy, the NPA absorption at $\lambda = 514$ nm does not affect the Raman intensities of long conjugated *trans*-NPA chains, which are responsible for the Raman lines at 1080 and 1470 cm^{-1} and the electric-dipole absorption in the range 600–750 nm (Fig. 1). Therefore, one can assume that the resonant Raman scattering at $\lambda = 514$ nm does not occur for the most Raman active long *trans*-NPA chains. Nevertheless, we will estimate the gain factor for the resonant Raman cross section from the electric-dipole transition of the *trans* isomer at $\nu_0 \sim E_g \approx 1.7$ eV. Since the lifetime of the lowest electric-dipole *trans*-NPA state is on the order of tens of femtoseconds, as it follows from the direct NPA measurements [12] and the photoluminescence data on *trans*-PA [13], the homogeneous broadening parameter can be estimated at $\Gamma \approx 0.1$ eV, and the characteristic gain factor can be estimated as $(E_g/\Gamma)^2 \sim 300$ (see, e.g., [14]). One can see that, even if the resulting Raman cross section σ at $\lambda = 514$ nm is attributed to the resonant Raman scattering, i.e., if the $(E_g/\Gamma)^2$ factor is taken into account, the Raman efficiency for the CC vibrational modes in *trans*-NPA will be three orders of magnitude higher than in diamond. Note that σ in NPA coincides with the value measured for the most studied Shirakawa's PA [15]. However, these values can hardly be compared with each other, because the Shirakawa's PA displays a broad structureless electric-dipole absorption band and the CC Raman linewidths by an order of magnitude larger than in NPA, which corresponds to a broad length distribution of conjugated chains. For this reason, it is commonly accepted that $\lambda = 514$ nm in the Shirakawa's PA corresponds to the resonant Raman scattering from a certain length [11, 15].

Further, the Raman efficiency of *trans*-NPA depends relatively weakly on the excitation wavelength as compared to the *cis* isomer, for which the Raman cross section increases sharply at $\lambda = 514$ nm [10]. In [7], the estimate $\sigma \sim 1 \times 10^{-27}$ cm^2/sr was obtained for the Raman CC vibrations in NPA at $\lambda = 1064$ nm, for which the absorption is four orders of magnitude lower than for the main absorption band of *trans* isomer [16], and the Raman lines also correspond to the NPA transparency band. With allowance for the correcting factor ν_S^4, the Raman intensity at $\lambda = 514$ nm is ~40 times higher than for $\lambda = 1064$ nm.

Therefore, the Raman spontaneous intensity for the CC vibrational modes in the *trans*-NPA structure is higher than in the diamond structure by several orders of magnitude, and this is not associated with resonant Raman scattering. We attribute the observed high Raman activity in *trans*-NPA to the CC coherent vibrations that can arise in the ordered *trans*-NPA chains. According to the model of coherent vibrations suggested recently in [6, 7], the CC-bond ensemble can scatter light fields coherently with the addition of their amplitudes rather than of their intensities, as it takes place in the Raman processes. The increase in the Raman intensity of the CC vibrational modes upon transition from diamond to *trans*-PA can be characterized by the number N of CC bonds coherently scattering light. As a rough estimate of N one can take $N \sim \sigma(\text{NPA})/\sigma(\text{diamond}) \sim 10^5$ at $\lambda = 514$ nm, which is approximately equal to the number of CC bonds in the PA nanoparticle. The CC vibration coherence effect, in a sense, is analogous to the scattered light coherence in CARS spectroscopy.

REFERENCES

1. R. H. Friend, R. W. Gymer, A. B. Holmes, *et al.*, Nature **397**, 121 (1999).
2. H. Sirringhaus, N. Tessler, and R. H. Friend, Science **280**, 1741 (1999).
3. J. H. Schön, A. Dodabalapur, Z. Bao, *et al.*, Nature **410**, 189 (2001).
4. V. M. Kobryanskii and E. A. Tereshko, Synth. Met. **39**, 367 (1991); V. M. Kobryanskii, Proc. SPIE **3937**, 132 (2000); Rapra Review Reports **10**, Number 6, Report 114 (2000).
5. V. M. Kobryanskiĭ, Dokl. Akad. Nauk **362**, 213 (1998).
6. D. Yu. Parashchuk and V. M. Kobryanskiĭ, Pis'ma Zh. Éksp. Teor. Fiz. **73**, 171 (2001) [JETP Lett. **73**, 152 (2001)].
7. D. Yu. Paraschuk and V. M. Kobryanskii, Phys. Rev. Lett. **87**, 207402 (2001).
8. T. T. Basiev, A. A. Sobol, P. G. Zverev, *et al.*, Opt. Mater. **11**, 307 (1999).
9. V. S. Gorelik and M. M. Sushchinskiĭ, Fiz. Tverd. Tela (Leningrad) **12**, 1475 (1970) [Sov. Phys. Solid State **12**, 1157 (1970)].
10. V. M. Kobryanskii, D. Yu. Paraschuk, A. N. Shchegolikhin, *et al.*, Proc. SPIE **4098**, 182 (2000).
11. E. Ehrenfreund, Z. V. Vardeny, O. Brafman, and B. Horovitz, Phys. Rev. B **36**, 1535 (1987).
12. S. Adachi, V. M. Kobryanskii, and T. Kobayashi, Phys. Rev. Lett. **89**, 027401 (2002).
13. J. Orenstein, in *Handbook of Conducting Polymers*, Ed. by T. A. Skotheim (Marcel Dekker, New York, 1986), Vol. II, p. 1297.
14. R. Loudon, *The Quantum Theory of Light* (Clarendon, Oxford, 1973; Mir, Moscow, 1976).
15. L. Lauchlan, S. P. Chen, S. Etemad, *et al.*, Phys. Rev. B **27**, 2301 (1983).
16. N. V. Chigarev, V. A. Ruilova-Zavgorodniy, D. Yu. Paraschuk, and V. M. Kobryanskii, Proc. SPIE **4748**, 398 (2002).

Translated by V. Sakun

JETP Letters, Vol. 76, No. 9, 2002, pp. 575–578. Translated from Pis'ma v Zhurnal Éksperimental'noĭ i Teoreticheskoĭ Fiziki, Vol. 76, No. 9, 2002, pp. 673–677.

Effect of Screening by Two-Dimensional Charge Carriers on the Binding Energy of Excitonic States in GaAs/AlGaAs Quantum Wells

S. I. Gubarev*, O. V. Volkov, V. A. Koval'skiĭ, D. V. Kulakovskiĭ, and I. V. Kukushkin

Institute of Solid-State Physics, Russian Academy of Sciences, Chernogolovka, Moscow region, 142432 Russia

** e-mail: gubarev@issp.ac.ru*

Received October 14, 2002

The spectrum of excitonic excited states in GaAs/AlGaAs quantum wells of different width is studied together with its change due to the screening of electron–hole interaction by two-dimensional electrons. The exciton binding energy decreases sharply with an increase in the concentration of two-dimensional electrons. The temperature dependence of screening parameters is studied for the ground and excited excitonic states down to ultralow temperatures $T = 50$ mK. © *2002 MAIK "Nauka/Interperiodica".*

PACS numbers: 73.21.Fg; 71.35.Cc; 78.66.Fd

The Coulomb interaction of charge carriers plays the central part in the collective effects occurring in the low-dimensional electron systems such as the fractional or integer quantum Hall effects and composite fermions [1, 2]. Since the interaction in a two-dimensional electron system is strongly screened, the investigation of screening parameters is highly important for the understanding of the nature of these collective phenomena and their correct theoretical description. In spite of the importance of Coulomb screening phenomenon, the experimental works devoted to this problem are few in number. The Coulomb screening by free carriers manifests itself most pronouncedly in the screening of a bound electron–hole states (excitons) in a quantum well and in the collapse (dissociation) of these bound states upon an increase in the charge-carrier concentration higher than its critical value [3, 4].

It is worth noting that, while on the subject of the collapse of excitonic states, we by no means imply that the bound state disappears from the semiconductor excitation spectrum, because the bound states arise in the two-dimensional systems with the attractive potential as weak as one likes. It will be shown in this work that the screening of electron–hole interaction in an exciton by a system of two-dimensional electrons brings about a sharp decrease in the exciton binding energy upon reaching the threshold concentration, and this is accompanied by a decrease in the oscillator strength of the excitonic transition. Such a threshold-like decrease in oscillator strength was observed for the perfect GaAs/AlGaAs structures at unexpectedly low concentrations of free charge carriers [4]. The screening effect on the binding energy of excitonic state has not been studied experimentally so far, although this parameter remained one of the most important parameters in the quantitative description of screened interaction in electron systems.

It is the purpose of this work to study experimentally the screening effect of two-dimensional charge carriers on the binding energy of the ground and excited excitonic states in the GaAs/AlGaAs quantum wells.

Single 180-Å and 300-Å GaAs/AlGaAs quantum wells were studied at temperatures from $T = 4.2$ K to $T = 50$ mK. Despite the fact that the structures were undoped, the presence of residual impurities in them gave rise to a low-density two-dimensional channel with a charge-carrier concentration on the order of $n_e = (1–20) \times 10^9$ cm^{-2}. The carrier concentration in the channel could be smoothly varied by the illumination of structure with a combination radiation of two laser sources: a semiconductor laser with the wavelength $\lambda = 7500$ Å (for the intrawell photoexcitation) and a He–Ne laser with $\lambda = 6328$ Å (for the overbarrier photoexcitation). This made it possible to vary the electron density in the channel from the maximal value (different in different structures but on the order of 2×10^{10} cm^{-2}) to 1×10^9 cm^{-2}.

Similar to the previous works [4, 5], the charge-carrier concentration in the channel was determined by the optical detection of the dimensional magnetoplasma resonance. To this end, mesas shaped like discs with a diameter of 0.1 mm were formed in the structures, and the samples were placed in the maximum of electric field on the microwave path. The plasma oscillation frequency was obtained from the magnetic-field dependences of differential luminescence signal appearing upon the power modulation of microwave field with a frequency of 16–40 GHz. This frequency was directly related to the mesa diameter and the concentration of two-dimensional electrons [6]. This technique made it

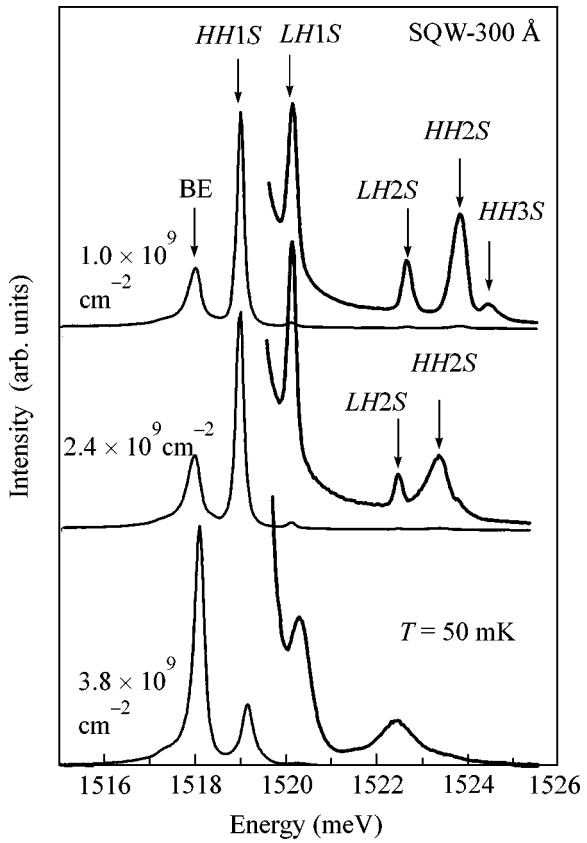

Fig. 1. Luminescence spectra measured at $T = 50$ mK in the 300-Å-thick quantum well for three concentrations of two-dimensional electrons. The electron concentration was measured by the magnetoplasma resonance method [4].

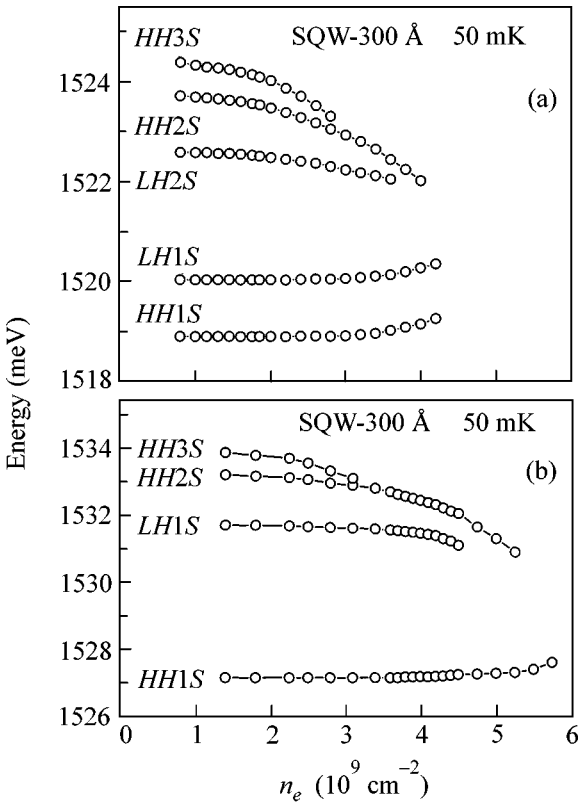

Fig. 2. Spectral positions of the excitonic ground (*HH*1*S*) and excited (*LH*1*S*, *LH*2*S*, *HH*2*S*, and *HH*3*S*) states as functions of electron concentration n_e measured for the GaAs/AlGaAs quantum wells (a) 300 and (b) 180 Å in thickness.

possible to determine the concentration of a two-dimensional electron gas up to the concentrations on the order of 1×10^9 cm^{-2} (the method of measurements is described in [4, 5]).

The high quality of the structures is seen from the fact that the well-resolved *HH*2*S*, *LH*2*S*, and *HH*3*S* lines of excited excitonic states (upper curve in Fig. 1) are clearly seen in the luminescence spectra at low carrier concentrations in the channel ($n_e \le 1 \times 10^9$ cm^{-2}), in addition to the lines corresponding to the recombination of the ground state of free (*HH*1*S*) and bound (*BE*) excitons on heavy holes and free excitons on light holes (*LH*1*S*). This interpretation of the observed lines is in compliance with the known experimental data [7] and confirmed by the numerical computations performed by us for a GaAs/AlGaAs quantum well with a given width. Moreover, our studies in a perpendicular magnetic field made it possible to unequivocally differentiate between the excitonic states with heavy and light holes and confirm the above-mentioned interpretation of excited states.

One can see from Fig. 1 that, as the concentration of two-dimensional carriers increases, the excited excitonic states are screened first, because their binding energies are lower and their wave functions are more extended than those of the ground state. Due to a decrease in the binding energy, the excited excitonic states thermally dissociate at helium temperatures $T =$ 1.5–4.2 K, as a result of which the lines corresponding to the transitions from the excited states disappear from the luminescence spectra of the structures under study. However, at ultralow temperatures on the order of 50 mK, the excited excitonic states are observed in the luminescence spectrum in a considerably broader concentration range (lower curves in Fig. 1). The binding energy of ground excitonic state on heavy (*HH*1*S*) and light (*LH*1*S*) holes is high and, correspondingly, it can be screened by a considerably higher concentrations of two-dimensional electrons. One can see from Fig. 1 that the screening of excited states is accompanied by a change in the spectral position of the respective recombination radiation lines.

Figure 2 shows the changes in the energies of the ground and excited excitonic states measured in the 180-Å and 300-Å quantum wells. One can see that the ground-state energy of the excitons on light and heavy holes almost does not change with a rise in the electron concentration in the wells and starts to shift to higher energies only at densities higher than 3×10^9 cm^{-2}. As

for the excited states, they undergo low-energy shift at very low concentrations n_e, with the least strongly bound *HH*3*S* state being shifted most pronouncedly. The behavior of excitonic terms in the narrower 180-Å quantum well coincides qualitatively with the behavior for the 300-Å well, with the only difference that the changes occur at higher electron concentrations.

A decrease in the exciton binding energy due to the screening of electron–hole interaction manifests itself more pronouncedly in a change of energy gap $E_{2S} - E_{1S}$ between the ground and excited excitonic states. Figure 3a shows the energy difference between the ground (*HH*1*S*) and excited (*HH*2*S*) excitonic states on heavy holes as a function of the concentration measured for the 300-Å and 180-Å quantum wells. One can see that this difference decreases almost twofold from 4.83 meV to 2.88 meV for the 300-Å well and from 6.05 meV to 3.59 meV for the 180-Å well with increasing electron concentration. In the narrower well with $L = 180$ Å, the screening is less efficient and the changes occur at higher electron concentrations. Such a dependence seems to be quite natural, because the exciton binding energy in the narrow well is higher, while the wave function in the well plane is less extended and, hence, the screening threshold should be shifted to higher electron concentrations. Figure 3b demonstrates the behavior of binding energy of the excitonic 1*S*, 2*P*, and 2*S* states (curves *1*, *2*, and *3*, respectively), as calculated by the relaxation method for the case of Linchard screening by two- dimensional electrons in the 300-Å-thick quantum well. For comparison, the ground-state (1*S*) energy calculated by the less accurate Ritz variational method [8] is also shown in the same figure. Despite the fact that the complex character of valence band in the quantum well was not taken into account in the calculations, the relaxation method properly describes the experimentally observed decrease in the binding energies of different excitonic states and yields the threshold concentrations close to their experimentally observed values.

It is worthy of note that the decrease in the binding energy of the 1*S* state is not accompanied by a noticeable change in the spectral position of the excitonic state, and a small shift to higher energies is observed only for high electron concentrations. In our opinion, such a behavior is caused by the fact that, apart from a decrease in exciton binding energy, the screening of Coulomb interaction also renormalizes the semiconductor gap, as a result of which the position of excitonic term is determined by the combined effect of these two contributions, which almost fully compensate each other.

From the curves presented in Fig. 2, one can determine changes in the exciton ground-state energy and in the position of semiconductor gap upon varying the concentration of quasi-two-dimensional electrons. For zero concentration of two-dimensional electrons in the channel, the theoretical calculations give $\sim E^b_{HH2S} =$ 1.15 meV for the binding energy of the *HH*2*S* excitonic state [7], whereas it decreases more than tenfold upon screening and, likely, does not exceed 0.1 meV when the excited states disappear from the luminescence spectra. For this reason, the position of the *HH*2*S* state at an electron concentration of 4×10^9 cm^{-2} coincides, to an accuracy better than 0.1 meV, with the renormalized semiconductor gap.

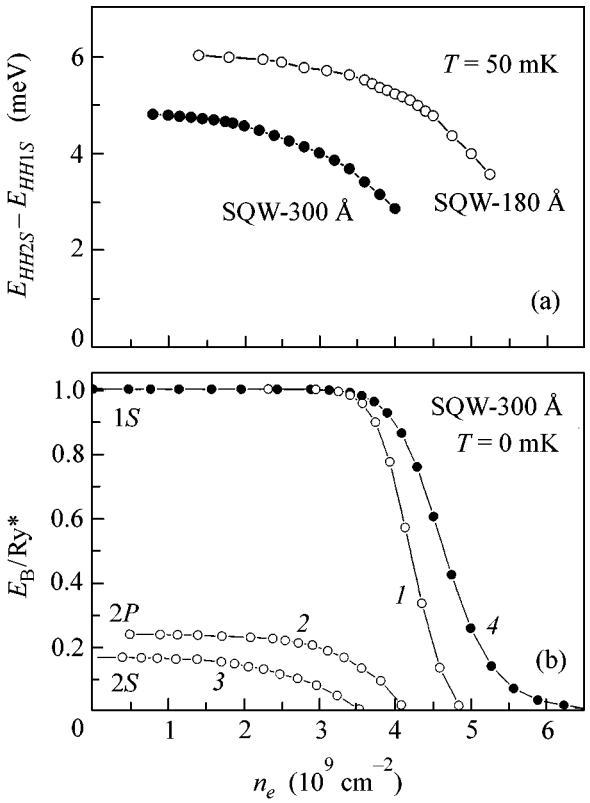

Fig. 3. (a) Energy gap $E_{HH2S} - E_{HH1S}$ between the ground (*HH*1*S*) and excited (*HH*2*S*) excitonic states as a function of electron concentration n_e measured for the quantum wells 300 and 180 Å in thickness. (b) Ground-state (1*S*) and excited-state (2*P* and 2*S*) exciton energies (curves *1*, *2*, and *3*, respectively) calculated by the relaxation method for the GaAs/AlGaAs quantum well of thickness 300 Å. Curve *4* corresponds to the exciton ground state calculated by the Ritz variational method.

Apart from measuring binding energies of the 1*S* and 2*S* excitonic states, we also examined the temperature dependence of the threshold concentration, for which the oscillator strength of excitonic transition decreases sharply, much as this was done in original work [4] in the range of appreciably lower temperatures down to $T = 50$ mK.

The influence of temperature on the screening of bound states in the quasi-two-dimensional systems has two aspects. On the one hand, the fraction of electrons localized at the fluctuations of random potential increases with lowering temperature, thereby reducing the concentration of mobile electrons that are involved in the screening of Coulomb interaction in the well. On

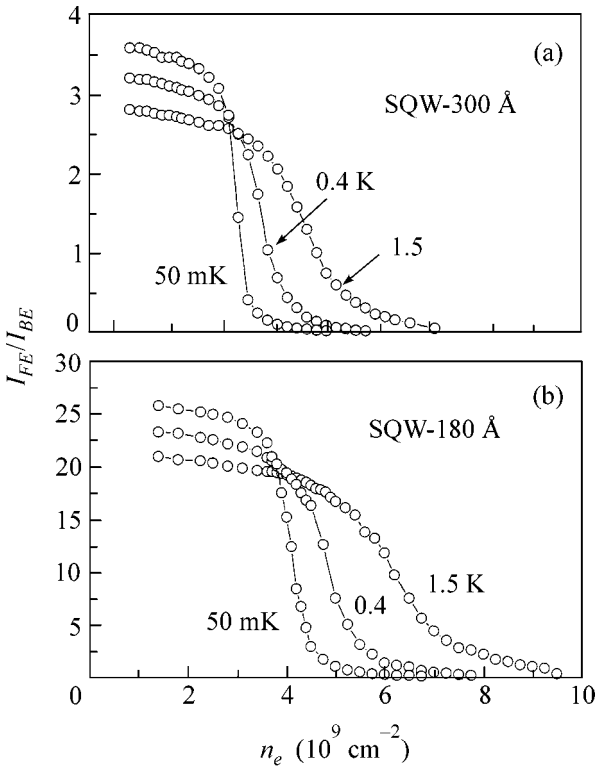

Fig. 4. Luminescence intensity ratio of the free (I_{FE}) and bound (I_{BE}) excitons as a function of electron concentration, as measured at various temperatures T = 1.5 K, 0.4 K, and 50 mK in (a) 300-Å-thick and (b) 180-Å-thick quantum wells.

the other hand, as shown in [8], the screening of excitonic states by two-dimensional electrons becomes more efficient with a decrease in temperature, because electrons with small momenta k make the greatest contribution to the screening. In the best structures, the screening of excitonic states occurs at very low concentrations, so that the electron gas is nondegenerate at temperatures T = 1.5–4.2 K. It was shown in [8] that the screening efficiency strongly depends on temperature in this case.

In Fig. 4, the variations of the line intensity ratio for the free and bound excitons are shown as functions of electron concentrations measured for two 180-Å- and 300-Å-thick quantum wells. One can see from this figure that the threshold concentration decreases with lowering temperature, evidencing the weakness of localization effects and a high quality of the samples. The temperature dependence of the threshold electron density, for which excitons become screened, is satisfactorily explained by the calculations made in [8]. At a temperature of 50 mK, the threshold concentration in the 300-Å quantum well is equal to 3×10^9 cm^{-2}, which corresponds to the dimensionless parameter r_s = 10.5. In the narrower quantum well 180 Å wide, the threshold concentration is higher, in accordance with the calculations carried out in [8].

The experimental results are in accordance with the results of calculations carried out in recent work [8] in the Linchard approximation with allowance for the nonlinear character of screening by two-dimensional electron gas in quantum wells. Taking into account the nonlinear character of screening leads to the satisfactory agreement with the experiment both for the value of threshold concentration and for the character of observed spectral changes under conditions of the collapse of excitonic states. Apart from the binding energy, a change in the oscillator strength was also calculated for the excitonic transition as a function of electron concentration in the quantum well. According to the calculations, the intensity of excitonic transition decreases less sharply than the binding energy with an increase in the density of two-dimensional gas. As a result, the exciton line in the optical experiments is observed even at relatively high electron concentrations, for which the exciton binding energy is appreciably lower.

In summary, we have investigated in this work how the binding energies of the excitonic ground and excited states decrease with increasing electron concentration in the well, as a result of the screening of electron–hole interaction by a system of quasi-two-dimensional electrons. The dependence of exciton binding energy on the electron density in the channel was experimentally measured. It was found that, upon lowering temperature from 1.5 K to 50 mK, the transition associated with exciton dissociation becomes more pronounced and shifts to lower electron concentrations.

This work was supported by the Russian Foundation for Basic Research, the State scientific and technical program “Nanostructures,” and INTAS (grant no. 99-1146).

REFERENCES

1. D. C. Tsui, H. L. Stormer, and A. C. Gossard, Phys. Rev. Lett. **48**, 1559 (1982).
2. J. K. Jain, Adv. Phys. **41**, 105 (1992).
3. G. Finkelstein, H. Strikman, and I. Bar-Josef, Phys. Rev. Lett. **74**, 976 (1995).
4. S. I. Gubarev, I. V. Kukushkin, S. V. Tovstonog, *et al.*, Pis’ma Zh. Éksp. Teor. Fiz. **72**, 469 (2000) [JETP Lett. **72**, 324 (2000)].
5. M. Yu. Akimov, I. V. Kukushkin, S. I. Gubarev, *et al.*, Pis’ma Zh. Éksp. Teor. Fiz. **72**, 662 (2000) [JETP Lett. **72**, 460 (2000)].
6. S. J. Allen, H. L. Stormer, and J. C. M. Hwang, Phys. Rev. B **28**, 4875 (1983).
7. D. C. Reynolds, K. K. Bajaj, C. Leak, *et al.*, Phys. Rev. B **37**, 3117 (1988).
8. D. V. Kulakovskiĭ, S. I. Gubarev, and Yu. E. Lozovik, Zh. Éksp. Teor. Fiz. **121**, 915 (2002) [JETP **94**, 785 (2002)].

Translated by V. Sakun

JETP Letters, Vol. 76, No. 9, 2002, pp. 579–583. Translated from Pis'ma v Zhurnal Éksperimental'noĭ i Teoreticheskoĭ Fiziki, Vol. 76, No. 9, 2002, pp. 678–682.

Boundary Conditions to the Ginzburg–Landau Equations at the Twinning Plane in a (*d* + *s*) Superconductor

E. A. Shapoval

All-Russia Research Institute of Metrological Service, Moscow, 117334 Russia

e-mail: shapoval@orc.ru

Received September 4, 2002; in final form, October 14, 2002

Effective boundary conditions to the Ginzburg–Landau equations at the twinning plane of an orthorhombic (*d* + *s*) superconductor are obtained on the basis of microscopic BCS theory. The range of the parameters of orthorhombic strain is found where the order parameter behaves variously on both sides of the twinning boundary.

PACS numbers: 74.20.De; 74.20.Fg

In recent years, much attention has been given to unconventional high-temperature orthorhombic superconductors [1–4]. This is due, in particular, to the observed breakdown of the tetragonal symmetry of CuO_2 planes in YBCO as a result of the appearance of CuO chains, which lead to the orthorhombic deformation of electronic spectrum and pair interaction, giving rise, in turn, to the *s* component in the order parameter if the latter had *d* symmetry in the absence of deformation. The two possible directions of these chains give rise to twinning boundaries that separate so-called twin domains with different chain directions. Although a number of works have been devoted to studying the behavior of domains near the twinning boundary [4–8], the question of boundary conditions to the Ginzburg–Landau (GL) equations at the twinning plane is still open. It turns out that the boundary conditions allow one to answer the question of how the order parameter of orthorhombic superconductors behaves upon passing to the neighboring domain.

For the quasi-two-dimensional superconductors of interest, the orthorhombicity can be introduced by writing the electron (quasiparticle) energy dispersion in the form

$$\begin{aligned}\epsilon(\mathbf{k}) &= 2t(k_x^2 + k_y^2 \mp 2ak_xk_y)\\ &= 2t((1 \mp a)k_x'^2 + (1 \pm a)k_y'^2),\end{aligned} \quad (1)$$

where the upper and lower signs relate to the right and left domains, respectively, and $k'_{x,y} = (k_y \pm k_x)/\sqrt{2}$. The corresponding Fermi surfaces (for $a = 0.5$) are shown at the top of Fig. 1.

The equations for the Fermi momenta can be written by introducing quasi-angular parameters $\theta_{1,2}$ measured from k'_x in the right and left domains:

$$k'_x = k_F\sqrt{1 \pm a}\cos\theta_{1,2}, \quad k'_y = k_F\sqrt{1 \mp a}\sin\theta_{1,2}, \quad (2)$$

where $k_F^2 = \sqrt{\epsilon_F/2t(1-a^2)}$ is the Fermi quasimomentum and ϵ_F is the Fermi energy. The introduction of the quasiangular parameter θ is suitable primarily because the averaging over the elliptic Fermi sur-

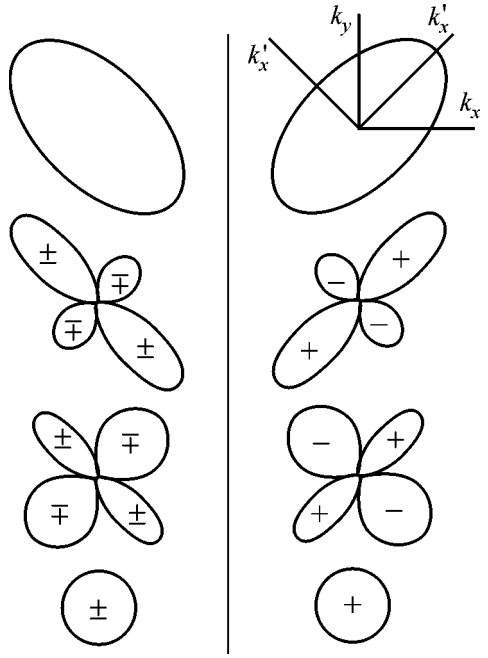

Fig. 1. (top) Fermi surfaces, (second row) order parameters, and (bottom) their *d* and *s* components in the neighboring domains for $a = b = 0.5$. The signs (±) correspond to the (upper sign) even and (lower sign) odd solutions.

face with allowance for the local density of states is greatly simplified:

$$\langle \ldots \rangle_F = \frac{1}{\nu}\int \frac{dS}{v}(\ldots) = \int_{-\pi}^{\pi} \frac{d\theta}{2\pi}(\ldots), \tag{3}$$

where v is the local velocity and ν is the total density of states at the Fermi surface.

The expressions for the momentum in the initial system are obtained from Eq. (2):

$$\begin{aligned} k_x^{(1,2)} &= k_F \cos(\theta_{1,2} - \alpha_{1,2}), \\ k_y^{(1,2)} &= k_F \cos(\theta_{1,2} - \alpha_{1,2}), \end{aligned} \tag{4}$$

where the indices (1, 2) again relate to the right and left domain, respectively, and $\tan\alpha_1 = \cot\alpha_2 = \sqrt{(1-a)/(1+a)}$. It follows that $\alpha_1 + \alpha_2 = \pi/2$. Introducing $\alpha = \alpha_2 - \alpha_1$, one has $\alpha_{1,2} = \pi/4 \mp \alpha/2$ and $\sin\alpha = a$ $(-\pi/2 < \alpha < \pi/2)$.

When an electron passes through the twinning boundary, its energy and y projection of momentum are conserved in the neighboring domain. It follows from Eq. (4) and the above definition of α that $\theta_2 - \theta_1 = \alpha$. Defining $\theta = (\theta_1 + \theta_2)/2 + \pi/4$, one has

$$k_x^{(1,2)} = k_F \cos(\theta \mp \alpha); \quad k_y^{(1,2)} = k_F \sin\theta. \tag{5}$$

By performing analogous calculations for the velocity $\mathbf{v} = \partial\epsilon(\mathbf{k})/\partial\mathbf{k}$, one finds that

$$v_x^{(1,2)} = v_F \cos\theta; \quad v_y^{(1,2)} = v_F \sin(\theta \mp \alpha) \tag{6}$$

at the Fermi surface, where $v_F = 2\sqrt{2t\epsilon_F}$ is the Fermi velocity. Hence it follows that, when passing to the neighboring domain, an electron conserves its velocity projection perpendicular to the twinning boundary. Moreover, it was shown in [6] that, at least in the strong coupling limit, an electron passes through the twinning boundary without reflection.

The effective boundary conditions to the GL equations are determined from the linearized equation for the order parameter $\Delta^*(\mathbf{p}_f, \mathbf{r})$ near the superconducting transition temperature,

$$\begin{aligned} \Delta^*(\mathbf{p}, \mathbf{r}) &= \sum_{\mathbf{p}', \mathbf{p}''} V(\mathbf{p} - \mathbf{p}'') \\ &\times \int d\mathbf{r}' \Delta(\mathbf{p}', \mathbf{r}') \pi T \sum_{\omega} \Phi_\omega(\mathbf{r}, \mathbf{p}''; \mathbf{r}', \mathbf{p}'), \end{aligned} \tag{7}$$

where $\mathbf{p}$ are the Fermi vectors determining the direction dependence of order parameter; the summation over these vectors corresponds, in fact, to the integration over the Fermi surface with allowance for the local density of states; V is the electron interaction potential; ω are the Matsubara frequencies; and the functions Φ_ω are defined through the Green's functions in the normal state:

$$\begin{aligned} \Phi_\omega(\mathbf{r}, \mathbf{p}; \mathbf{r}', \mathbf{p}') &= \sum_{\mathbf{q}, \mathbf{q}'} G_\omega(\mathbf{p}' + \mathbf{q}'/2, \mathbf{p} + \mathbf{q}/2) \\ &\times G_{-\omega}(-\mathbf{p}' + \mathbf{q}'/2, -\mathbf{p} + \mathbf{q}/2) \exp i(\mathbf{q}'\mathbf{r}' - \mathbf{q}\mathbf{r}). \end{aligned} \tag{8}$$

The electron–electron potential can be expanded in terms of a set of mutually orthogonal normalized functions at the Fermi surface:

$$V(\mathbf{p} - \mathbf{p}') = \sum_n V_n \phi_n(\mathbf{p}) \varphi_n(\mathbf{p}'), \tag{9}$$

where the positive V_n values correspond to attraction. It was shown by Pokrovskiĭ in [9] that, near the transition temperature $(1 - T/T_c \ll 1)$ in the weak coupling limit, one can take into account only the leading term corresponding to the maximum value of V_n in this expansion. Then the order parameter is $\Delta^*(\mathbf{p}, \mathbf{r}) = \Psi(\mathbf{r})\varphi(\mathbf{p})$, where the index for the function $\varphi(\mathbf{p})$ is omitted.

The simplest such function satisfying the orthorhombic symmetry condition and normalized at the Fermi surface can be written to the left and right of the twinning plane as

$$\begin{aligned} \varphi_{1,2} &= \frac{\pm\sqrt{2}\cos 2\theta_{1,2} + b}{\sqrt{1 + b^2}} \\ &= \frac{\pm\sqrt{2}(\sin(2\theta \mp \alpha) + b)}{\sqrt{1 + b^2}}. \end{aligned} \tag{10}$$

If the s component $|b| < \sqrt{2}$, the energy gap has zeros; otherwise, at $|b| > \sqrt{2}$, the gap is everywhere nonzero. The function $\varphi(\theta)$ on both sides of the twinning boundary is shown in the second row of Fig. 1, and below are shown its d and s components. The signs indicate their behavior for the even or odd solution of the spatial function $\Psi(\mathbf{r})$.

The kernel of the linearized integral equation can be most simply calculated by the quasi-classical trajectory method generalized to anisotropic superconductors [10, 11]. Considering that all spatial quantities depend only on the coordinate x, one finds

$$\begin{aligned} \Psi(x) &= \nu V_0 \int_0^\infty K_{11}(x - x')\Psi(x')dx' \\ &+ \nu V_0 \int_{-\infty}^0 K_{12}(x - x')\Psi(x')dx'; \quad x > 0; \\ \Psi(x) &= \nu V_0 \int_0^\infty K_{21}(x - x')\Psi(x')dx' \\ &+ \nu V_0 \int_{-\infty}^0 K_{22}(x - x')\Psi(x')dx'; \quad x < 0, \end{aligned} \tag{11}$$

where $K_{11} = K_{22}$ account for the contribution of electron trajectories within one domain and $K_{12} = K_{21}$ account for the contribution of the electron trajectories passed from one domain to the other through the twinning boundary:

$$\begin{aligned} K_{11}(x) &= \sum_{n=-\omega_D/2\pi T_c}^{\omega_D/2\pi T_c} \left\langle \frac{(\varphi_{1,2}(\theta))^2}{|\cos\theta|} \exp\left|\frac{(2n+1)x}{\cos\theta}\right| \right\rangle_F; \\ K_{12}(x) &= \sum_{n=-\omega_D/2\pi T_c}^{\omega_D/2\pi T_c} \left\langle \frac{(\varphi_1(\theta)\varphi_2(\theta))}{|\cos\theta|} \exp\left|\frac{(2n+1)x}{\cos\theta}\right| \right\rangle_F. \end{aligned} \tag{12}$$

To simplify formulas, the length henceforth is measured in units of coherent length $\xi_0 = v_F/2\pi T_c$, and ω_D is the Debye cutoff frequency for the logarithmically divergent integrals and sums in the BCS model.

Due to the symmetry property, this system has two linearly independent solutions (even and odd), each being the unique solution (except for an arbitrary coefficient) to the equation

$$\begin{aligned} \Psi^{\pm}(x) &= \nu V_0 \int_0^\infty (K_{11}(x-x) \pm K_{12}(x+x'))\Psi^{\pm}(x')dx' \\ &= \nu V_0 \int_0^\infty K^{\pm}(x, x')\Psi^{\pm}(x')dx'. \end{aligned} \tag{13}$$

In what follows, the indices (±) relate, respectively, to the even and odd solutions.

The effective boundary conditions to the GL equation follow from the asymptotic solution to this integral equation at $x \gg 1$. By direct substitution, one can readily verify that the linear function $\Psi \sim x + \lambda$, where λ is the extrapolation length defining the boundary condition $\Psi'(0) = \Psi(0)/\lambda$, is such an asymptotic solution. Our goal is to calculate this extrapolation length from Eq. (13). We will do this by applying the variational approximation proposed by Svidzinskiĭ [12, 13]. According to this method, the extrapolation length can be written, to first approximation, as

$$\lambda = \frac{H + G^2/E}{F + G}, \tag{14}$$

where

$$\begin{aligned} E &= \int_0^\infty \left[1 - \nu V_0 \int_0^\infty K(x, x')dx'\right]dx, \\ F &= \int_0^\infty \left[1 - \nu V_0 \int_0^\infty K(x, x')dx'\right]xdx, \\ G &= \int_0^\infty \left[\nu V_0 \int_0^\infty K(x, x')dx' - x\right]dx, \\ H &= \int_0^\infty \left[\nu V_0 \int_0^\infty K(x, x')dx' - x\right]xdx. \end{aligned} \tag{15}$$

In our problem,

$$\begin{aligned} E^{\pm} &= \frac{\pi^2}{8}\int_{-\pi}^{\pi}\frac{d\theta}{2\pi}|\cos\theta|(\varphi_1^2(\theta) \mp \varphi_1(\theta)\varphi_2(\theta)), \\ F^{\pm} &= \frac{7\zeta(3)}{8}\int_{-\pi}^{\pi}\frac{d\theta}{2\pi}\cos^2\theta(\varphi_1^2(\theta) \mp \varphi_1(\theta)\varphi_2(\theta)), \\ G^{\pm} &= \frac{7\zeta(3)}{8}\int_{-\pi}^{\pi}\frac{d\theta}{2\pi}\cos^2\theta(\varphi_1^2(\theta) \pm \varphi_1(\theta)\varphi_2(\theta)), \\ H^{\pm} &= \frac{\pi^4}{96}\int_{-\pi}^{\pi}\frac{d\theta}{2\pi}|\cos^3\theta|(\varphi_1^2(\theta) \pm \varphi_1(\theta)\varphi_2(\theta)). \end{aligned} \tag{16}$$

Here,

$$\begin{aligned} \varphi_1^2(\theta) = \phi_2^2(\theta) &= 1 - \cos 2\alpha\cos^2\beta\cos 4\theta \\ &\quad - \sqrt{2}\sin\alpha\sin 2\beta\cos 2\theta + \ldots, \\ \varphi_1(\theta)\varphi_2(\theta) &= \cos^2\beta(\cos 4\theta - \cos 2\alpha) \\ &\quad + \sin^2\beta - \sqrt{2}\sin\alpha\sin 2\beta\cos 2\theta + \ldots, \end{aligned} \tag{17}$$

where the ellipses stand for the θ-odd terms that vanish upon the integration. For simplicity, the orthorhombic deformation parameter b describing its s component is set to be equal to $b = \tan\beta$ $(-\pi/2 \le \beta \le \pi/2)$.

By using Eq. (17), one can evaluate $E^{\pm}$, $F^{\pm}$, $G^{\pm}$, and $H^{\pm}$, whereupon we find from Eq. (14) the extrapolation lengths $\lambda^{\pm}$. The resulting algebraic expressions are too cumbersome to present them in this paper. The extrapolation lengths can more simply be evaluated from Eqs. (16) and (17) for the given orthorhombic deformation parameters $a = \sin\alpha$ and $b = \tan\beta$. Figure 2 shows the dependences of λ^+ and λ^- on the parameter b for various positive values of a. For the negative a values, the extrapolation lengths are $\lambda^{\pm}(a, b) = \lambda^{\pm}(-a, -b)$.

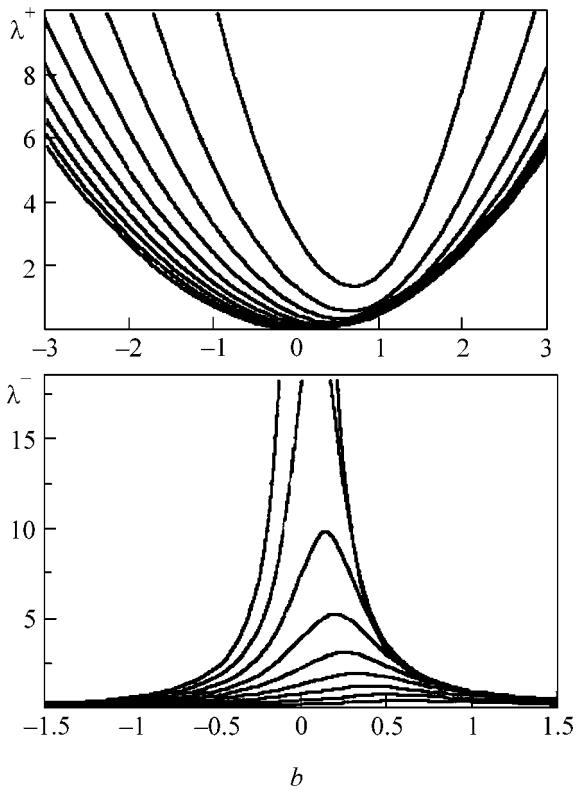

Fig. 2. Relative extrapolation lengths in units of $\xi_0 = v_F/2\pi T_c$ for the (upper panel) even and (bottom panel) odd solutions to Eq. (13) as functions of the orthorhombic deformation parameter (*s* component of order parameter) *b* for various values of orthorhombic deformation parameter *a* of Fermi surface from (upper curves) 0 to 0.9 with a step of 0.1.

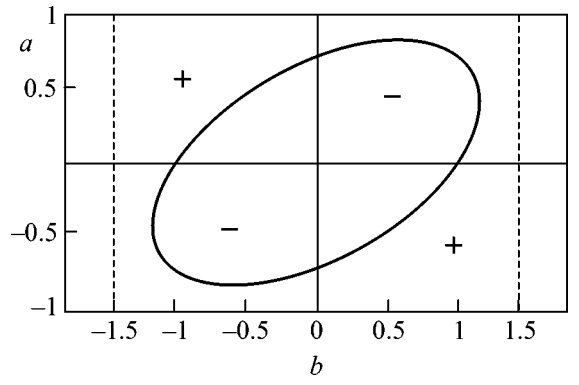

Fig. 3. Regions of (outside the ellipsoidal curve) even and (inside) odd behavior of the spatial solution as a function of the orthorhombic deformation parameters *a* and *b*. The vertical dashes separate the regions where the modulus of *s* component $|b| > \sqrt{2}$, so that the energy gap has no zeros there.

The following boundary conditions at the twinning plane follow from these results:

$$\begin{aligned}
&\mathbf{n}\left(\nabla - \frac{ie}{c}\mathbf{A}\right)\Psi(\mathbf{r})\Big|_{+0} \\
&= \frac{1}{2}\left(\frac{1}{\lambda^+} + \frac{1}{\lambda^-}\right)\Psi(+0) + \frac{1}{2}\left(\frac{1}{\lambda^+} - \frac{1}{\lambda^-}\right)\Psi(-0), \\
&\mathbf{n}\left(\nabla - \frac{ie}{c}\mathbf{A}\right)\Psi(\mathbf{r})\Big|_{-0} \\
&= \frac{1}{2}\left(\frac{1}{\lambda^-} - \frac{1}{\lambda^+}\right)\Psi(+0) - \frac{1}{2}\left(\frac{1}{\lambda^+} + \frac{1}{\lambda^-}\right)\Psi(-0).
\end{aligned} \tag{18}$$

These conditions, naturally, satisfy the condition for conservation of current through the twinning boundary.

It follows from boundary conditions (18) that the GL functional for the free energy of a superconductor includes the twinning-induced surface energy density equal in the respective units to

$$\begin{aligned}
\mathcal{F}_{\text{surf}} &= \frac{1}{2\lambda^+}|\Psi(+0) + \Psi(-0)|^2 \\
&+ \frac{1}{2\lambda^-}|\Psi(+0) - \Psi(-0)|^2.
\end{aligned} \tag{19}$$

Therefore, the even or odd spatial behavior of the order parameter with respect to the twinning plane depends on the ratio of the extrapolation lengths λ^+ and λ^-. Figure 3 shows the ellipsoidal curve separating the regions of odd (inside) and even (outside) behavior of $\Psi(\mathbf{r})$ as a function of the orthorhombic deformation parameters *a* and *b*. In the first case, the *d* component of order parameter dominates. According to definition (10), this component (illustrated in Fig. 1) only deforms upon passing through the twinning boundary because of the orthorhombic deformation of the Fermi surface, while the *s* component changes sign, confirming the commonly accepted assumption about the behavior of the order parameter components of (*d* + *s*) superconductors with respect to the twinning boundary [5–8]. If the solution $\Psi(\mathbf{r})$ is spatially even, the *s* component of order parameter dominates, and it is, naturally, even about the twinning plane, while the *d* component changes sign. The vertical dashed lines in Fig. 3 separate the regions where the energy gap has no zeros.

To this point, we considered the case where electrons pass through the twinning plane freely, i.e., without reflection. If the electron reflection from the twinning boundary (with reflection coefficient *R*) is taken into account, the even solution does not change, because the contribution of the reflected electron trajectories coincides with the contribution of the electron trajectories starting from the symmetric point of the neighboring domain, as is well seen in Fig. 1. Contrastingly, the odd solution changes appreciably, because the sign of the contribution from the reflected electrons

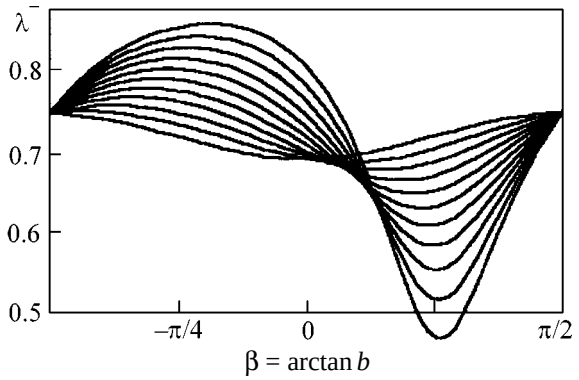

Fig. 4. Extrapolation lengths λ^- for the odd solution with the electron reflection coefficient from the twinning boundary $R = 1/2$ as functions of $\beta = \arctan b$ for various values of orthorhombic deformation parameter a of Fermi surface. At the right of the upper and bottom curves, $a = 0$ and 1, respectively. The remaining curves correspond to other a values with a step of 0.1.

is opposite to that of the electrons coming from the symmetric point of the neighboring domain, so that the second terms in Eqs. (16) for E^-, F^-, G^-, and H^- acquire the factor $(1 - 2R)$. In particular, at $R = 1/2$, the reflected electrons fully compensate the contribution of the electrons coming from the neighboring domain, so that the second terms in Eq. (16) vanish and λ^- becomes equal to the extrapolation length for a superconductor bordering the normal metal with free (reflectionless) electron passing through the interface. In this case, the problem can be exactly solved by the Wiener–Hopf method. The extrapolation lengths calculated by the Wiener–Hopf method for quasi-two-dimensional s and d_{xy} superconductors are equal to 0.696 and 0.744, respectively [14], while the variational approximation used in this work gives 0.688 (for $a = \alpha = 0$ and $b = \infty$; i.e., $\beta = \pi/2$) and 0.754 (for $a = \alpha = 0$ and $b = \beta = 0$), indicating that the error of variational approximation is less than 1.5%.

Figure 4 presents the extrapolation length λ^- as a function of the parameter $\beta = \arctan b$ for $R = 1/2$ and the parameters α ranging from 0 to 1, which is convenient for the inclusion of the limiting s state with $b = \infty$.

Surprisingly, the curves separating the regions of even and add spatial solutions, depending on the orthorhombic deformation parameters a and b for all $D = 1 - R > 0$, virtually coincide with the curve for $R = 0$ shown in Fig. 3 and differ from it no more than by 1%, i.e., lesser than the above-mentioned estimated error of the variational approximation. In other words, the regions of even and odd solutions with respect to the twinning boundary are virtually independent of the reflection coefficient R in the case of nonzero transmission coefficient D.

This work was supported by the Scientific Council of the direction "Superconductivity" of the State Scientific and Technical Program "Topics in Condensed State Physics."

REFERENCES

1. C. O'Donovan and J. R. Carbotte, Phys. Rev. B **52**, 16208 (1995).
2. M. T. Beal-Monod and K. Maki, Phys. Rev. B **53**, 5775 (1996); **55**, 1194 (1997).
3. R. Modre, I. Schürrel, and E. Schachinger, Phys. Rev. B **57**, 5496 (1995).
4. D. Einzel and I. Schürrel, Physica B (Amsterdam) **284–288**, 451 (2000).
5. M. Sigrist, K. Kuboki, A. Lee, *et al.*, Phys. Rev. B **53**, 2835 (1996).
6. M. E. Zhitomirsky and M. B. Walker, Phys. Rev. Lett. **79**, 1734 (1997).
7. D. L. Feder, A. Beadsall, A. J. Berlinsky, and C. Kallin, Phys. Rev. B **56**, R5751 (1997).
8. W. Belzig, C. Bruder, and V. Sigrist, cond-mat/9801107 (1998).
9. V. L. Pokrovskiĭ, Zh. Éksp. Teor. Fiz. **40**, 641 (1961) [Sov. Phys. JETP **13**, 447 (1961)].
10. E. A. Shapoval, Zh. Éksp. Teor. Fiz. **47**, 1007 (1964) [Sov. Phys. JETP **20**, 675 (1964)]; Zh. Éksp. Teor. Fiz. **49**, 930 (1965) [Sov. Phys. JETP **22**, 647 (1966)]; Zh. Éksp. Teor. Fiz. **88**, 1073 (1985) [Sov. Phys. JETP **61**, 630 (1985)].
11. E. A. Shapoval, Pis'ma Zh. Éksp. Teor. Fiz. **64**, 350 (1996) [JETP Lett. **64**, 381 (1996)].
12. A. V. Svidzinskiĭ, *Spatially Heterogeneous Problems of Superconductivity* (Nauka, Moscow, 1982).
13. V. P. Mineev and K. V. Samokhin, *Introduction to the Theory of Unusual Superconductivity* (Mosk. Fiz.-Tekh. Inst., Moscow, 1998).
14. E. A. Shapoval, Pis'ma Zh. Éksp. Teor. Fiz. **74**, 224 (2001) [JETP Lett. **74**, 204 (2001)].

Translated by V. Sakun

JETP Letters, Vol. 76, No. 9, 2002, pp. 584–589. Translated from Pis'ma v Zhurnal Éksperimental'noĭ i Teoreticheskoĭ Fiziki, Vol. 76, No. 9, 2002, pp. 683–688.

Transmission Capability of a Sequential Relativistic Quantum Communication Channel with Limited Observation Time

S. N. Molotkov

Institute of Solid State Physics, Russian Academy of Sciences, Chernogolovka, Moscow region, 142432 Russia

Received September 24, 2002; in final form, October 9, 2002

It is shown that the identity of particles must inevitably be taken into account, because states in quantum field theory are nonlocalizable. This circumstance, together with finite limiting velocity, is responsible for the asymptotic character of formulas for the transmission capability of nonrelativistic communication channels (they are formally valid only for infinite time delay between messages, when the identity of particles is negligible, and, correspondingly, for infinitely slow transmission in time—bits per second per message). The transmission capability of a sequential relativistic quantum communication channel is obtained in real time with allowance for the identity of particles. © *2002 MAIK "Nauka/Interperiodica".*

PACS numbers: 03.67.Hk

Transmission capability is one of the basic parameters of a communication channel [1]. It determines the upper rate of information transmission through the communication channel and equals the number of bits (≤ 1) per message that can be transmitted for a sufficiently long sequence with arbitrarily low error probability.

Classical information theory is formulated in terms of statistical ensembles [1]. Input quantities for a discrete channel are alphabet symbols that are sent to the channel with certain probabilities. The channel is described by the transition probabilities between the entry and exit for each symbol [1, 2]. In this case, the physical nature of information carriers associated with the alphabet symbols is not specified, but it is implicitly meant that a certain classical object (signal) corresponds to each symbol.

The entry object for a nonrelativistic quantum communication channel is a quantum ensemble [3–6]. The alphabet symbols are assigned to density matrices that are sent to the channel with certain probabilities. The quantum communication channel is formally described by a mapping (superoperator) that transforms the input density matrices into the output ones [3–6]. When classical information is transmitted through the quantum communication channel, rather than the quantum state itself, classical information is extracted at the receiver end by measurements. Quantum coding theorems were excellently reviewed by Holevo [4]. The physical nature of information carriers is also not specified.

The most important characteristic of a communication channel is its transmission capability in real time. The usual treatment of transmission capability as a rate (number of bits per message) is not associated with the transmission speed in real time, because the formulation of the problem does not involve time. It is implicitly meant that the alphabet symbols are transmitted with certain frequency. In this approach, logical contradictions do not arise for the classical nonrelativistic communication channel, because classical signals corresponding to the alphabet symbols can be measured as quickly as is wished (instantaneously) and, therefore, the transmission rate per unit time is determined only by the repetition frequency of symbols (if extra restrictions on the properties of the communication channel, e.g., on its transmission band, are absent).

The situation is basically different in relativistic quantum mechanics, which emerges immediately as quantum field theory in the absence of reasonable interpretation [7–9]. A state vector $|\varphi\rangle \in \mathcal{H}$ describing the quantum system must have a carrier (amplitude smoothing function) depending on the spacetime argument. The amplitude is specified on the mass shell. For this reason, the amplitude is nonlocalizable for both massless and massive particles in the Minkowski spacetime [10, 11], i.e., is nonzero over the entire space (beyond any compact region). Therefore, the calculation of trace over spatial degrees of freedom requires the availability of the entire space. In contrast to the nonrelativistic case, the existence of the limiting velocity makes this operation dangerous and leads to real physical sequences: the access to the entire space requires infinite time. In any real case, measurements are carried out in a limited spacetime domain. Therefore, there is a fundamental question of how the transmission capability of the communication channel depends on the quantum state (spacetime amplitude), spacetime domains, where measurements are carried out, and the reference frame.

0021-3640/02/7609-0584$22.00

If the state amplitudes cannot be strictly localized (this is true at least for free fields), the states that are sequentially sent into the communication channel cannot be treated as independent due to the inevitable overlap. In this case, the space of states is not described by the tensor product of the spaces of states for individual messages ($\mathcal{H}^{\otimes n}$) and must be described by either the symmetrized (Sym$\mathcal{H}^{\otimes n}$ for bosons) or antisymmetrized (Asym$\mathcal{H}^{\otimes n}$ for fermions) tensor product. Identical particles can be treated as distinguishable in individual messages, and the space of states can be efficiently described as the ordinary tensor product only for the infinite spacing between individual messages. However, the transmission speed in time (bits per second) is zero in this case due to the existence of the limiting velocity.

The generalized functions with operator values are represented in the form [7–9]

$$\hat{\varphi}^+_\mu(\hat{x}) = \int d\hat{k} e^{i\hat{k}\hat{x}} a^+_\mu(\hat{k})\theta(k_0)\delta(\hat{k}^2),$$
$$\hat{k} = (k_0, k), \quad \hat{x} = (x, t), \tag{1}$$

where $\mu = 0, 1$ is the helicity index. The generalized basis vectors (linear continuous functionals in $\mathcal{H}$) have the form

$$a^+_\mu(\hat{k})|0\rangle = |k\mu\rangle, \quad |\hat{x}\mu\rangle = \varphi_\mu(\hat{x})|0\rangle,$$
$$\langle k\mu|k'\mu'\rangle = k_0\delta_{\mu\mu'}\delta(k-k'), \tag{2}$$
$$[a^-_{\mu'}(\hat{k}'), a^+_\mu(\hat{k})] = k_0\delta(k-k')\delta_{\mu,\mu'},$$

where $|0\rangle$ is the vacuum vector, $|k\mu\rangle, |\hat{x}\mu\rangle \in \Omega^*$, and Ω^* is the space conjugated to the basic function space Ω. Physical states (vectors in $\mathcal{H}$) are obtained by smoothing the generalized operator functions with basic functions (amplitudes) from space $\Omega(\hat{x})$ (space of infinitely differentiable functions decreasing at infinity more rapidly than any negative power):

$$|\varphi_\mu\rangle = \sum_\mu \int d\hat{x}\tilde{\varphi}_\mu(\hat{x})\varphi^+_\mu(\hat{x})|0\rangle$$
$$= \sum_\mu \int \frac{dk}{k_0}\tilde{\varphi}_\mu(k, k_0 = |k|)|k\mu\rangle. \tag{3}$$

Here, the amplitude $\tilde{\varphi}_\mu(\hat{x})$ ($\tilde{\varphi}(k, k_0 = |k|)$) serves as the coefficient of expansion in terms of the generalized basis states. The construction $\tilde{\varphi}_\mu(\hat{x}) \in \Omega(\hat{x})$, $\tilde{\varphi}_\mu(\hat{x}) \in \Omega^*(\hat{x})$, and $|\varphi_\mu\rangle \in \mathcal{H}$, and $\Omega \subset \mathcal{H} \subset \Omega^*$ is the equipped Hilbert space (Gelfand triad) [8, 13].

Below, we consider the following field states propagating in one direction of the x axis ($k > 0$), which carry information between remote users:

$$|\varphi_\mu\rangle = \int_0^\infty \frac{dk}{k}\tilde{\varphi}(k, k)|k\mu\rangle = \int_0^\infty dk\varphi(k)|k\mu\rangle$$
$$= \int_{-\infty}^\infty (d(x-t))\varphi(x-t)|x-t, \mu\rangle, \tag{4}$$

where

$$\varphi(k) = \frac{\tilde{\varphi}(k, k)}{\sqrt{k}}, \quad \varphi(x-t) = \frac{1}{2\pi}\int_0^\infty e^{-ik(x-t)}\varphi(k)dk,$$
$$|x-t, \mu\rangle = \int_0^\infty e^{ik(x-t)}|k\mu\rangle dk, \tag{5}$$

with the normalization condition

$$\langle\varphi_\mu|\varphi_\mu\rangle = \int_0^\infty \frac{dk}{k}|\tilde{\varphi}(k, k)|^2 = \int_0^\infty dk|\varphi(k)|^2$$
$$= \int_{-\infty}^\infty d(x-t)|\varphi(x-t)|^2 = 1. \tag{6}$$

We discuss now the problem of admissible degree of amplitude localization on the branch of the light cone. The square integrability (normalization) condition for $\varphi(k)$ restricts the admissible degree of decreasing $\varphi(\tau)$ at infinity ($\tau \longrightarrow \infty$). The answer is given by the Wiener–Paley theorem [14]. For a square integrable function $\varphi(k)$, which is equal to zero on the semiaxis $k < 0$ but is not identical zero, the following integral must converge:

$$\int_{-\infty}^\infty \frac{\ln|\varphi(\tau)|}{1+\tau^2}d\tau < \infty. \tag{7}$$

Therefore, the amplitude $\varphi(\tau)$ on the light cone cannot decrease exponentially, but this decrease can be arbitrarily close to the exponential $|\varphi(\tau)| \sim \exp\{-\alpha|\tau|/\ln(\ln(\ln\ldots\ln|\tau|))\}$ (α is a positive number); i.e., states are nonlocalizable (are nonzero beyond any compact domain).

Let us discuss the transmission of classical information by a quantized massless field. It is fundamentally impossible to use only single-photon states in the case of a sequential communication channel because of nonlocalizability. We consider the binary alphabet {0, 1} with *a priori* probabilities $\{\pi_0, \pi_1\}$, which is assigned to quantum states with generally nonorthogonal polarizations $\{\nu_0, \nu_1\}$. For simplicity, the spatial amplitudes for different polarizations are considered as identical. The

results are simply generalized to arbitrary amplitudes. Individual messages of length n consist of single-photon states sequentially sent into the communication channel with the interval τ_0. More exactly, a message of length n is described by the following n-photon state vector, whose components are taken with probabilities $\{\pi_0, \pi_1\}$:

$$|\varphi_\nu\rangle = A_n \int_0^\infty \ldots \int_0^\infty dk_1 dk_2 \ldots dk_n \varphi_1(k_1) \times \varphi_2(k_2) \ldots \varphi_n(k_n) |k_1\nu_1, k_2\nu_2, \ldots, k_n\nu_n\rangle, \quad (8)$$

$$\varphi_m(k_m) = \varphi(k_m) e^{ik_m\tau_0(m-1)}, \quad \boldsymbol{\nu} = (\nu_1, \nu_2, \ldots, \nu_n),$$

where decomposition goes over the generalized basis vectors from Ω^*:

$$|k_1 i_1, k_2 i_2, \ldots, k_n i_n\rangle = a^+_{i_1} a^+_{i_2}(k_1) \ldots a^+_{i_n}(k_n)|0\rangle, \quad i_m = +, - \quad m = 1 \ldots n, \quad (9)$$

and

$$a^+_{\nu_i}(k_i) = \alpha_{\nu_i} a^+_+(k_i) + \beta_{\nu_i} a^+_-(k_i), \quad i = 0, 1, \quad |\alpha_{\nu_i}|^2 + |\beta_{\nu_i}|^2 = 1, \quad (10)$$

where indices $i_m = +, -$ correspond to the orthogonal basis polarization states. The generalized basis states are completely symmetric with respect to the particle permutations [7–9] and have the following form in the momentum space (for details, see [8]):

$$|k_1 j_1, k_2 j_2, \ldots, k_n j_n\rangle = \sqrt{\frac{k_1 k_2 \ldots k_n}{n!}} \times \sum_{\{i\}} \delta_{j_1, j_{i_1}} \delta(k_1 - q_{i_1}) \ldots \delta_{j_n, j_{i_n}} \delta(k_n - q_n), \quad (11)$$

where $j_l, j_{i_l} = +, -$ and the sum is taken over all particle permutations $\{i\}$. The orthogonality condition for the generalized basis vectors has the form

$$\langle k_1 j_1, k_2 j_2, \ldots, k_n j_n | k'_1 j'_1, k'_2 j'_2, \ldots, k'_m j'_m\rangle = \delta_{n,m} k_1 k_2 \ldots k_n \times \sum_{\{i\}} \delta_{j_1, j'_{i_1}} \delta(k_1 - k'_{i_1}) \ldots \delta_{j_n, j'_{i_n}} \delta(k_n - k'_{i_n}). \quad (12)$$

We now consider the normalization condition for the n-photon vectors of messages of length n. In order to emphasize the difference between the case of identical particles and the case of distinguishable particles, we first suppose that information is coded into the orthogonal polarization states [$j_i = +, -$ in Eq. (11)]. In this case, we have

$$\begin{aligned}\langle \varphi_{\mathbf{j}} | \varphi_{\mathbf{j}'} \rangle &= A_n^2 \int_0^\infty \ldots \int_0^\infty dk_1 \ldots dk_n \int_0^\infty \ldots \int_0^\infty dk'_1 \ldots dk'_n \\ &\times \varphi_1^*(k_1)\varphi_1(k'_1) \ldots \varphi_n^*(k_n)\varphi_n(k'_n) \\ &\times \langle k_1 j_1, k_2 j_2, \ldots, k_n j_n | k'_1 j'_1, k'_2 j'_2, \ldots, k'_m j'_m\rangle \\ &= A_n^2 \int_0^\infty \ldots \int_0^\infty dk_1 \ldots dk_n \sum_{\{i\}} \delta_{j_1, j'_{i_1}} \varphi_1^*(k_1)\varphi_1(k_1) \\ &\times e^{ik\tau_0(i_1 - 1)} \ldots \delta_{j_n, j'_{i_n}} \varphi_n^*(k_n)\varphi_n(k_n) e^{ik_n\tau_0(i_n - n)} \\ &= A_n^2 \sum_{\{i\}} \int_{-\infty}^\infty d\tau_1 \delta_{j_1, j'_{i_1}} \varphi^*(\tau_1)\varphi(\tau_1 - \tau_0(i_1 - 1)) \ldots \\ &\times \int_{-\infty}^\infty d\tau_n \delta_{j_n, j'_{i_n}} \varphi^*(\tau_n)\varphi(\tau_n - \tau_0(i_n - n)).\end{aligned} \quad (13)$$

Recall that the single-particle amplitude is normalized to unity according to Eq. (6). Overlaps in different positions for identical particles are zero formally only for $\tau_0 = \infty$ because of fundamental nonlocalizability.

We first find the transmission capability in the case where the observation time is unlimited (formally equal to infinity; i.e., the entire branch of the light cone is accessible in τ) and then generalize the results to finite time. Let us discuss the direct coding theorem for a source.

The density matrix corresponding to the code word from a random set of M words has the form

$$\rho^{(n)}_{\boldsymbol{\nu}_j} = |\varphi_{\boldsymbol{\nu}_j}\rangle\langle\varphi_{\boldsymbol{\nu}_j}|, \quad \boldsymbol{\nu}_j = (\nu_{1j}, \ldots, \nu_{nj}), \quad j = 1 \ldots M, \quad (14)$$

and, after averaging of $\mathbf{E}$ over all possible random sets of code words, provides the total density matrix of all possible messages of length n:

$$\rho^{(n)} = \mathbf{E}(\rho^{(n)}_{\boldsymbol{\nu}_j}) = \sum_{\boldsymbol{\nu}} P_{\boldsymbol{\nu}} |\varphi_{\boldsymbol{\nu}}\rangle\langle\varphi_{\boldsymbol{\nu}}|, \quad P_{\boldsymbol{\nu}} = \sum_{i_1, \ldots, i_n} \pi_{\nu_{i_1}} \ldots \pi_{\nu_{i_n}}, \quad i_m = 0, 1, \quad (15)$$

where $P_{\boldsymbol{\nu}}$ is the probability of state $|\varphi_{\boldsymbol{\nu}}\rangle$. Reduce $\rho^{(n)}$ to the diagonal form

$$\rho^{(n)} = \sum_{\mathbf{J}} \lambda_{\mathbf{J}} |\lambda_{\mathbf{J}}\rangle\langle\lambda_{\mathbf{J}}|, \quad \langle\lambda_{\mathbf{J}}|\lambda_{\mathbf{J}'}\rangle = \delta_{\mathbf{J},\mathbf{J}'}, \quad \mathbf{J} = (J_1, \ldots, J_{2^n}), \quad (16)$$

where the eigenvalues $\lambda_{\mathbf{J}}$ and eigenvectors $|\lambda_{\mathbf{J}}\rangle$ can be expanded in terms of the generalized basis vectors as

$$\begin{aligned}|\lambda_{\mathbf{J}}\rangle &= \sum_{i_1,\ldots,i_n}\int_0^\infty\ldots\int_0^\infty dk_1\ldots dk_n \\ &\times\Phi(k_1 i_1,\ldots,k_n i_n;\tau_0)|k_1 i_1,\ldots,k_n i_n\rangle \\ &= \sum_{i_1,\ldots,i_n}\int_{-\infty}^\infty\ldots\int_{-\infty}^\infty d\tau_1\ldots d\tau_n \\ &\times\Phi(\tau_1 i_1,\ldots,\tau_n i_n;\tau_0)|\tau_1 i_1,\ldots,\tau_n i_n\rangle.\end{aligned} \tag{17}$$

The amplitude $\Phi(k_1 i_1, \ldots, k_n i_n; \tau_0)$ is uniquely expressed in terms of single-particle amplitudes $\varphi(k)$ and their polarizations and also depends on the time spacing (τ_0) between individual packets.

The projector on the typical space of the n-photon density matrix

$$\begin{aligned}\mathrm{Typ} &= \{\lambda_{\mathbf{J}} : e^{-(H^{(n)}+\delta)} < \lambda_{\mathbf{J}} < e^{-(H^{(n)}-\delta)}\}, \\ P_\varepsilon^{(n)} &= \sum_{\lambda_{\mathbf{J}}\in\mathrm{Typ}} |\lambda_{\mathbf{J}}\rangle\langle\lambda_{\mathbf{J}}|, \\ H^{(n)} &= -\sum_{\mathbf{J}}\lambda_{\mathbf{J}}\log\lambda_{\mathbf{J}}\end{aligned} \tag{18}$$

is the von Neumann entropy of the ensemble of n-photon states, where $P_\varepsilon^{(n)}$ is the projector on the typical subspace. After averaging over random code words [3–6], the mean error over the random sets of M code words of length n satisfies the inequality

$$\begin{aligned}\bar{P}_e(n, M) &\le 2\mathrm{Tr}\{\rho^{(n)}(I - P_\varepsilon^{(n)})\} \\ &+ \mathrm{Tr}\{\rho^{(n)}P_\varepsilon^{(n)}\rho^{(n)}P_\varepsilon^{(n)}\} \le 2\varepsilon + (M-1)e^{-(H^{(n)}-\delta)}.\end{aligned} \tag{19}$$

The error can be made arbitrarily small, if the number of code words satisfies the inequality $M = e^{nR^{(n)}} < e^{H^{(n)}-\delta}$; i.e., the number of bits per one message meets the condition

$$R^{(n)} < \frac{H^{(n)}}{n} - \delta'. \tag{20}$$

The limit of $H^{(n)}/n$ for $n \longrightarrow \infty$ is important. It is always smaller than $H^{(1)\otimes n}$, because the overlap of individual packets decreases the distinguishability of code words due to the identity of particles.

The quantity $H^{(n)}/n$ decreases with increasing n for fixed spacing τ_0 and a given amplitude. For $\tau_0 = 0$, we have $H^{(n)} = 0$, because all states in the typical subspace become identical. Let the spacing of one extreme packet on the light cone be $\tau_0 = \infty$. In this case, the density matrix is $\rho^{(n)} = \rho^{(n-1)} \otimes \rho^{(1)}$ and

$$\frac{H^{(n)}}{n} \le \frac{H^{(n-1)}}{n} + \frac{H^{(1)}}{n} \le \frac{H^{(n-1)}}{n-1}. \tag{21}$$

The sequence $H^{(n)}/n$ decreases and is limited from below. Therefore, the limit exists and equals

$$H_\infty = \lim_{n\to\infty}\frac{H^{(n)}}{n}. \tag{22}$$

This limit is the transmission capability and determines the rate of information transmission as the number of bits per message per photon. However, it is not the speed in the bit /s sense, because the access to the entire branch of light cone is required.

The inverse coding theorem is proved using the Fano inequality [3, 6] and gives the same upper estimate for the number of code words as inequality (20) does.

The transmission capability as the number of bits per second is associated with measurements in a finite time window, and we discuss this problem below.

In the preceding case, where the entire light-cone branch in τ is accessible (unlimited observation time), the space, in which the probability distribution of results arises after decoding, is a discrete space specified by the indices of code words $\boldsymbol{\nu}_j = (\nu_{1j}, \ldots, \nu_{nj})$. The fundamental difference of the decision rule (unity decomposition) for a finite observation window is that the space of results is the Cartesian product of sets

$$\begin{aligned}\Sigma &= [(\tau_1 \in T_n, \nu_{1j}) \cup (\tau_1 \in \bar{T}_n, \nu_{1j})] \\ &\times\ldots[(\tau_n \in T_n, \nu_{nj}) \cup (\tau_n \in \bar{T}_n, \nu_{nj})],\end{aligned} \tag{23}$$

where T_n is the light-cone region accessible to observation (time window) and $T_n + \bar{T}_n = (-\infty, \infty)$. In what follows, it is convenient to denote $T_n = nT_0$ (T_0 is the effective time window per message). When an n-photon message is decoded, the outcome of a measurement in each of the channels numbered by indices ν_{kj} can be either in the time window, $\tau_k \in T_n$, or outside it, $\tau_k \in \bar{T}_n$, independently of other values. The latter outcome means that the detector in the time window T_n did not trigger.

Any operator acting in n-photon subspace on polarization degrees of freedom in a limited time window

can be expanded in terms of the generalized basis operators as

$$X_{\mathbf{j}\mathbf{j}'} = \int\ldots\int dk_1\ldots dk_n|k_1j_1, \ldots, k_nj_n\rangle\langle k_nj_n', \ldots, k_1j_1'|$$
$$= \int\limits_{T_n}\frac{d\boldsymbol{\tau}}{(2\pi)^n}\left(\int\limits_0^\infty d\mathbf{k}e^{i\mathbf{k}\boldsymbol{\tau}}|\mathbf{k}\mathbf{j}\rangle\right)\left(\int\limits_0^\infty d\mathbf{k}'e^{-i\mathbf{k}'\boldsymbol{\tau}}\langle\mathbf{k}'\mathbf{j}'|\right) \quad (24)$$
$$+ \int\limits_{\bar{T}_n}\frac{d\boldsymbol{\tau}}{(2\pi)^n}\left(\int\limits_0^\infty d\mathbf{k}e^{i\mathbf{k}\boldsymbol{\tau}}|\mathbf{k}\mathbf{j}|\right)\left(\int\limits_0^\infty d\mathbf{k}'e^{-i\mathbf{k}'\boldsymbol{\tau}}\langle\mathbf{k}'\mathbf{j}'|\right),$$

where the following notation is introduced for brevity:

$$|k_1j_1, \ldots, k_nj_n\rangle = |\mathbf{k}\mathbf{j}\rangle, \quad k = (k_1, \ldots, k_n),$$
$$\boldsymbol{\tau} = (\tau_1, \ldots, \tau_n), \quad \mathbf{j} = (j_1, \ldots, j_n),$$
$$d\mathbf{k} = dk_1\ldots dk_n, \quad d\boldsymbol{\tau} = d\tau_1\ldots d\tau_n \quad j_k = \pm.$$

The density matrix for an individual message in the basis of generalized states is equal to

$$\rho_\nu^n = |\varphi_\nu\rangle\langle\varphi_\nu| = \left(\sum_{l_1, \ldots, l_n = \pm}\int\limits_0^\infty\ldots\int\limits_0^\infty dk_1\ldots dk_n\gamma_{l_1}\ldots\gamma_{l_n}\right.$$
$$\left.\times\varphi(k_1)\ldots\varphi(k_n)e^{ik_n\tau_0(n-1)}|k_1l_1\ldots k_nl_n\rangle\right)$$
$$\times\left(\sum_{l_1', \ldots, l_n' = \pm}\int\limits_0^\infty\ldots\int\limits_0^\infty dk_1'\ldots dk_n'\gamma_{l_1'}^*\ldots\gamma_{l_n'}^*\right. \quad (25)$$
$$\left.\times\varphi_{l_1'}^*(k_1')\ldots\varphi_{l_n'}^*(k_n')e^{ik_n'\tau_0(n-1)}\langle k_n'l_n'\ldots k_1'l_1'|\right),$$

where $\gamma_{l_i} = \alpha_i$, $l_i = +$ and $\gamma_{l_i} = \beta_i$, $l_i = -$. Therefore, the density matrix for the ensemble of n messages is $\rho^{(n)} = \sum_\nu P_\nu\rho_\nu^{(n)}$. After calculation of the trace over space-time variables in the basis $|\mathbf{k}\mathbf{j}\rangle$, the effective density matrix takes the form

$$\rho_{\nu e}^{(n)} = \sum_{\{\mathbf{i}, \mathbf{i}'\}}\sum_{l_1, l_1', \ldots, l_n, l_n' = \pm}\int\limits_{T_n}\frac{d\boldsymbol{\tau}}{(2\pi)^n}$$
$$\times\gamma_{l_{i_1}}\gamma_{l_{i_1'}}^*\varphi_{i_1}(\tau_1)\varphi_{i_1'}^*(\tau_1)\ldots\gamma_{l_{i_n}}\gamma_{l_{i_n'}}^*\varphi_{i_n}(\tau_n)\varphi_{i_n'}^*(\tau_n)$$
$$\times\delta_{j_1, l_{i_1}}\delta_{l_{i_1'}', j_1'}\ldots\delta_{j_n, l_{i_n}}\delta_{l_{i_n'}', j_n'} \oplus \sum_{\{\mathbf{i}, \mathbf{i}'\}}\sum_{l_1, l_1', \ldots, l_n, l_n' = \pm}\int\limits_{\bar{T}_n}\frac{d\boldsymbol{\tau}}{(2\pi)^n} \quad (26)$$
$$\times\gamma_{l_{i_1}}\gamma_{l_{i_1'}}^*\varphi_{i_1}(\tau_1)\varphi_{i_1'}^*(\tau_1)\ldots\gamma_{l_{i_n}}\gamma_{l_{i_n'}}^*\varphi_{i_n}(\tau_n)\varphi_{i_n'}^*(\tau_n)$$
$$\times\delta_{?_1, l_{i_1}}\delta_{l_{i_1'}', ?_1}\ldots\delta_{?_n, l_{i_n}}\delta_{l_{i_n'}', ?_n},$$

where j_k, j_k', $?_k = \pm$ and similarly for the total density matrix. The sign of direct sum indicates that the second term is orthogonal to the first term. In the second term, it is sufficient to retain only diagonal elements (as was discussed above), and the formal change $j_k, j_k' \longrightarrow ?_k$ is made. Repeating the preceding argumentation, one can obtain that the number of code words is equal to (for details, see [3–6])

$$R^{(n)} < H(\mathcal{T}[\rho^{(n)}]) - \sum_\nu P_\nu H(\mathcal{T}[\rho_\nu^{(n)}]) - \delta$$
$$= H(\rho_e^{(n)}) - \sum_\nu P_\nu H(\rho_{\nu e}^{(n)}) - \delta. \quad (27)$$

The inverse coding theorem can be proved similarly [3, 6] using the quantum analogue of the Fano inequality. Therefore, the transmission capability is

$$C(T_0)$$
$$= \max_{\{\pi_0, \pi_1\}}\lim_{n\to\infty}\left(\frac{H(\rho_e^{(n)}) - \sum_\nu P_\nu H(\rho_{\nu e}^{(n)})}{nT_0}\right)\left[\frac{\text{bit}}{\text{photon s}}\right]. \quad (28)$$

Thus, since states in quantum field theory are nonlocalizable, individual messages cannot be described as independent because of their inevitable overlap, and the identity of particles must therefore be taken into account. This circumstance, together with the existence of finite limiting velocity, is responsible for the asymptotic character of formulas for the transmission capability of nonrelativistic communication channels (they are valid formally only for infinite spacing between messages, when the identity of particles can be ignored). The transmission speed in time (bit/s message) tends to zero in this case. Formula (28) determines the transmission capability of the relativistic quantum channel in real time.

I am grateful to S.S. Nazin for stimulating discussions and critical remarks. This work was supported by the Russian Foundation for Basic Research (project no. 02-02-16289) and project nos. 40.020.1.1.1170 and 37.029.1.1.0031.

REFERENCES

1. C. E. Shannon, Bell Syst. Tech. J. **27**, 397 (1948); **27**, 623 (1948).
2. R. G. Gallager, *Information Theory and Reliable Communication* (Wiley, New York, 1968; Sov. Radio, Moscow, 1974).
3. A. S. Kholevo, Probl. Peredachi Inf. **8**, 63 (1972); **15**, 3 (1979); Usp. Mat. Nauk **53**, 193 (1998).
4. R. Jozsa and B. Schumacher, J. Mod. Opt. **41**, 2343 (1994).

5. P. Hausladen, R. Jozsa, B. Schumacher, *et al.*, Phys. Rev. A **54**, 1869 (1996).
6. B. Schumacher and M. D. Westmoreland, Phys. Rev. A **56**, 131 (1997).
7. N. N. Bogoliubov and D. V. Shirkov, *Introduction to the Theory of Quantized Fields* (Nauka, Moscow, 1973; Wiley, New York, 1980).
8. N. N. Bogolyubov, A. A. Logunov, and I. T. Todorov, *Introduction to Axiomatic Quantum Field Theory* (Nauka, Moscow, 1969; Benjamin, New York, 1975).
9. N. N. Bogolyubov, A. A. Logunov, A. I. Oksak, and I. T. Todorov, *General Principles of Quantum Field Theory* (Nauka, Moscow, 1987).
10. D. A. Kirzhnits, Usp. Fiz. Nauk **90**, 129 (1966).
11. I. Bialynicki-Birula, Phys. Rev. Lett. **80**, 5247 (1998).
12. A. M. Jaffe, Phys. Rev. **158**, 1454 (1967).
13. I. M. Gel'fand and N. Ya. Vilenkin, *Generalized Functions*, Vol. 4: *Applications of Harmonic Analysis* (Fizmatgiz, Moscow, 1961; Academic, New York, 1964).
14. N. Wiener and R. Paley, *Fourier Transform in the Complex Domain* (American Mathematical Society, New York, 1934; Nauka, Moscow, 1964).

Translated by R. Tyapaev